☐ Revision No.

Project No. G-35-605

Project Director: Dr. E. Mosmal

Sponsor: National Science Foundation: Washington, D. C. 20550

Type Agreement: Grant No. INT-8109101

Award Period: From 9/1/81 To 2/28/83* (Performance) 5/31/85 (Reports)

Sponsor Amount: $20,440 2/28/84

Contracted through: GTRI/XXX

Cost Sharing: 742 (G-35-605) 2/28/85

Title: A Study of Internal Gravity Waves in the Po Valley

ADMINISTRATIVE DATA OCA CONTACT William F. Brown x4820

1) Sponsor Technical Contact: Ms. M. Rurak, Rm. 1214, International Programs, National Science Foundation, 1800 G Street, N. W., Washington, D. C. 20550

2) Sponsor Admin./Contractual Contact: Ms. P. L. Green, Grants Official; Division of Grants and Contracts, Directorate for Administration, National Science Foundation, Washington, D. C. 20550

Reports: See Deliverable Schedule Security Classification:

Defense Priority Rating:

RESTRICTIONS

See Attached NSF Supplemental Information Sheet for Additional Requirements.

Travel: Foreign travel must have prior approval - Contact OCA in each case. Domestic travel requires sponsor approval where total will exceed greater of $500 or 125% of approved proposal budget category.

Equipment: Title vests with GIT

COMMENTS: *Includes the usual six month unfunded flexibility period.

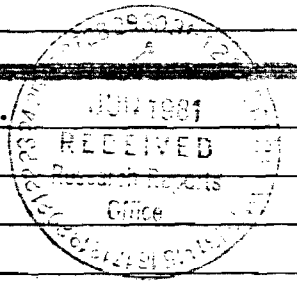

COPIES TO:

Administrative Coordinator
Research Property Management
Accounting Office
Procurement/EES Supply Services
Research Security Services
Reports Coordinator (OCA)
Legal Services (OCA)
Library, Technical Reports
EES Research Public Relations (2
Project File (OCA)
Other:

Date 11/15/85

Project No G-35-634 Subcontract GEO 901

Includes Subproject No(s) N/A

Project Director(s) Dr. Franco Einaudi GTRC / XXX

Sponsor National Science Foundation, Washington, D.C.

Title A Study of Internal Gravity Waves in the Po Valley

Effective Completion Date: 2/28/85 (Performance) 5/31/85 (Reports)

Grant/Contract Closeout Actions Remaining:

- [ ] None
- [ ] Final Invoice or Final Fiscal Report
- [ ] Closing Documents
- [X] Final Report of Inventions - Sent Questionnaire to Dr. Einaudi for file.
- [ ] Govt. Property Inventory & Related Certificate
- [ ] Classified Material Certificate
- [ ] Other _____

Continues Project No. None Indicated Continued by Project No. None Indicated

COPIES TO:

Project Director
Research Administrative Network
Research Property Management
Accounting
Procurement/GTRI Supply Services
Research Security Services
Reports Coordinator (OCA)
Legal Services
Library
GTRC
Research Communications (2)
Project File
Other A. Jones; M. Heyser; R. Embry

ORM OCA 69.285

G-35-605

GEORGIA INSTITUTE OF TECHNOLOGY
SCHOOL OF GEOPHYSICAL SCIENCES

Atlanta, Georgia 30332
(404) 894-2857

September 14, 1982

Mrs. Marilyn Rurak
Room 1214, International Program
National Science Foundation
1800 G Street NW
Washington, D.C. 20550

Dear Mrs. Rurak:

Following our telephone conversation, I am including the following items regarding my grant "A Study of Internal Gravity Waves in the Po Valley."

a) A report on the work performed during the first year. At the end of the report there is a brief statement of the work we intend to do during the second year.
b) Statement of other support for me.
c) A budget for the second year.

I hope that the enclosed documents are what you need to proceed with the funding of the second year. Thank you, and best wishes.

Sincerely,

Franco Einaudi

FE:rr

Enclosures.

CONTINUATION FOR G-35-605

ROUTE + C/S SHEET REQUESTED FROM CAROL COOK.

9/14/82

APPENDIX I

PROPOSAL TO THE NATIONAL SCIENCE FOUNDATION
Cover Page

FOR CONSIDERATION BY NSF ORGANIZATIONAL UNIT (Indicate the most specific unit known, i.e. program, division, etc.)	IS THIS PROPOSAL BEING SUBMITTED TO ANOTHER FEDERAL AGENCY? Yes ___ No ___ ; IF YES, LIST ACRONYM(S):
U.S. - Italy Cooperative Science Program Division of International Programs	
PROGRAM ANNOUNCEMENT/SOLICITATION NO.: U.S.-Italy Cooperative Science Program	CLOSING DATE (IF ANY):

NAME OF SUBMITTING ORGANIZATION TO WHICH AWARD SHOULD BE MADE (INCLUDE BRANCH/CAMPUS/OTHER COMPONENTS)
GEORGIA TECH RESEARCH INSTITUTE
Georgia Institute of Technology

ADDRESS OF ORGANIZATION (INCLUDE ZIP CODE)
Georgia Institute of Technology
Atlanta, GA 30332

TITLE OF PROPOSED PROJECT
A Study of Internal Gravity Waves in the Po Valley

REQUESTED AMOUNT	PROPOSED DURATION	DESIRED STARTING DATE
$19,214	1 year	September 1, 1982

PI/PD NAME AND SOCIAL SECURITY NO. (SSN)*	PI/PD PHONE NO.
Franco Einaudi, 105 386 352	

PI/PD DEPARTMENT	PI/PD ORGANIZATION
School of Geophysical Sciences	

ADDITIONAL PI/PD AND SSN*	ADDITIONAL PI/PD AND SSN*
ADDITIONAL PI/PD AND SSN*	ADDITIONAL PI/PD AND SSN*

FOR RENEWAL OR CONTINUING AWARD REQUEST, LIST PREVIOUS AWARD NO.: INT-8105101	SUBMITTING ORGANIZATION IS ___ IS NOT X A SMALL BUSINESS CONCERN (see CFR Title 13, Part 121 for definitions).

*Submission of social security numbers is voluntary and will not affect the organization's eligibility for an award. However, they are an integral part of the NSF information system and assist in processing the proposal. SSN solicited under NSF Act of 1950, as amended.

CHECK APPROPRIATE BOX(ES) IF THIS PROPOSAL INCLUDES ANY OF THE ITEMS LISTED BELOW:

- ☐ Animal Welfare
- ☐ Human Subjects
- ☐ National Environmental Policy Act
- ☐ Endangered Species
- ☐ Marine Mammal Protection
- ☐ Research Involving Recombinant DNA Molecules
- ☐ Historical Sites
- ☐ Pollution Control
- ☐ Proprietary and Privileged Information

PRINCIPAL INVESTIGATOR/ PROJECT DIRECTOR	AUTHORIZED ORGANIZATIONAL REP.	OTHER ENDORSEMENT (optional)
NAME: Franco Einaudi	NAME: G. D. Hutchison	NAME:
SIGNATURE:	SIGNATURE:	SIGNATURE:
TITLE: Professor	TITLE: Contracting Officer	TITLE:
DATE: September 14, 1982	DATE: September 14, 1982	DATE:

REPORT ON THE WORK PERFORMED DURING THE PERIOD
September 4, 1981 - August 31, 1982

The work performed during this time has proceeded along the following two lines: (1) acquisition of data in the Po Valley; and (2) development of analytical and numerical tools to analyze them.

1) The pressure measurements were carried out with a network of 9 microbarographs deployed in the Po Valley. Most of the sensors were located along two South-North trajectories to satisfy the requirements of ALPEX. The data were collected for about one month during the Spring 1982 ALPEX experiment.

The data were stored on cassettes specially designed so as to minimize the number of times they had to be replaced. They were able to store about a week's worth of data. It should be noted that the pressure data Dr. Perona obtained are much more detailed than those required by ALPEX since the integration time was only 10 seconds. From the variability of the maxima and minima of the signals, the data appear promising. Mr. Flavio Canavero, who is the graduate student at Tech working on this project, is in the process of transferring the data from the cassettes to a magnetic tape. This process, (for reasons related to the original design of the cassettes), has turned out to be lengthier than expected and Mr. Canavero has worked on it intensely in the last two months. The transfer should be completed by the end of September.

2) The analysis of the data proceeds in the following sequence:
   (a) spectral analysis of the pressure signal of each individual station;
   (b) cross correlation analysis between signals at various stations to identify the phase velocity of the individual disturbances.

We have tested various programs on an event of particular interest to us. Such an event took place on May 9, 1979 in the United States. Thunderstorms appeared in the Northern Plains to form a somewhat regular sequence of storm cells. We analyzed the pressure traces in the area where the storm occurred to isolate the waves.

Without going into detail, I mention the various programs that have been utilized, as follows:

i. All the data are filtered using a pass "humming" window. The filter was created using a program written by Rabiner, McGonegal and Paul [1979].

ii. Two different programs were used to calculate the power spectra of each signal. One method was to find the Fourier transform of the auto-covariance function. We employed the program written by Rabiner, Schafer and Dlugos [1979]. The second technique we have used is the maximum entropy method. The program used in this case utilizes the Burg algorithm (Burg [1976])and was taken from Robinson and Silvia [1981].

iii. We wrote our own cross correlation technique.

The overall analysis of the May 9, 1979 case was quite satisfactory and we expect to be able to utilize the techniques developed to the data collected in the Po Valley.

The program for the second year of our research consists in analyzing the data obtained during the ALPEX experiment. We expect to analyze them using the techniques developed last year and mentioned above.

As mentioned earlier, the distribution of the sensors during the Spring 1982 experiment was designed in terms of the ALPEX experiment. We expect to carry out another experiment in the latter part of the year, having in mind a smaller size network of microbarographs. The final formulation of our plans in this regard will, in part, depend on the results derived from the data already collected.

References

1. Rabiner, L.R., R.W. Schafer, and D. Dlugos [1979], "Correlation Method for Power Spectrum Estimation," Programs for Digital Signal Processing, IEEE Press, New York, Ch. 2.2.

2. Rabiner, L.R., C.A. Mc Gonegal, and D. Paul [1979], "FIR Windowed Filter Design Program - WINDOW", ibid, Ch. 5.2.

References - continued

3. Burg, John Parker [1975], "Maximum Entropy Spectral Analysis," Ph.D. Thesis, Stanford University.

4. Robinson, R.A. and M.T. Silvia [1981], Digital Foundations of Time Series Analysis, Vol. 2, Wave Equation Space Time Processing, Holden-Day, Inc., San Francisco.

CURRENT AND PENDING SUPPORT FOR FRANCO EINAUDI

Franco Einaudi has submitted to the National Science Foundation a 3-year proposal entitled "An Investigation of the Interaction between Turbulence and Propagating Internal Gravity Waves in the Planetary Boundary Layer." Franco Einaudi has requested 3 months' salary/year in this grant.

INSTRUCTIONS ON
:RSE BEFORE
'LETING)

SUMMARY
PROPOSAL BUDGET

FOR NSF USE ONLY

PROPOSAL NO.	DURATION (MONTHS) Proposed	Granted
AWARD NO.		

GANIZATION
orgia Institute of Technology

NCIPAL INVESTIGATOR/PROJECT DIRECTOR
anco Einaudi

ENIDR PERSDNNEL: PI/PD, Co-PI's, Faculty and Dther Senior Associates List each separately with title, A.6. show number in brackets)	NSF FUNDED PERSON-MOS CAL.	ACAD	SUMR	FUNDS REQUESTED BY PRDPDSER	FUNDS GRANTED BY NSF (IF DIFFERENT)
				$	$
) OTHERS (LIST INDIVIDUALLY ON BUDGET EXPLANATIDN PAGE)					
( ) TOTAL SENIOR PERSONNEL (1-5)					
DTHER PERSDNNEL (SHOW NUMBERS IN BRACKETS)					
) POST DOCTORAL ASSOCIATES					
) DTHER PRDFESSIDNALS (TECHNICIAN, PRDGRAMMER, ETC.)					
1) GRADUATE STUDENTS 1/2 time student				9,000	
( ) UNDERGRADUATE STUDENTS					
( ) SECRETARIAL-CLERICAL					
( ) OTHER					
TOTAL SALARIES AND WAGES (A+B)				9,000	
FRINGE BENEFITS (IF CHARGED AS DIRECT COSTS)					
TOTAL SALARIES, WAGES AND FRINGE BENEFITS (A+B+C)				9,000	
PERMANENT EQUIPMENT (LIST ITEM AND DOLLAR AMOUNT FOR EACH ITEM EXCEEDING $1,000. ITEMS OVER $10,000 REQUIRE CERTIFICATION)					
TOTAL PERMANENT EQUIPMENT					
TRAVEL 1. DOMESTIC (INCL. CANADA AND U.S. POSSESSIONS)					
2. FOREIGN				2,940	
tlanta-Rome round trip ($1,150), travel within Italy ($250), 1 week n Rome at $68 per diem ($476), 2 weeks in Turin at $76 per diem ($1,064) ncludes PI and Graduate ~~Research Assistant~~					
PARTICIPANT SUPPORT COSTS					
1. STIPENDS $					
2. TRAVEL					
3. SUBSISTENCE					
4. OTHER					
TOTAL PARTICIPANT COSTS					
OTHER DIRECT COSTS					
1. MATERIALS AND SUPPLIES				556	
2. PUBLICATION COSTS/PAGE CHARGES					
3. CONSULTANT SERVICES					
4. COMPUTER (ADPE) SERVICES On Ga. Tech CYBER 70 at DCAA approved rates				1,500	
5. SUBCONTRACTS					
6. OTHER					
TOTAL OTHER DIRECT COSTS				2,056	
TOTAL DIRECT COSTS (A THROUGH G)				13,996	
INDIRECT COSTS (SPECIFY) 47.2% of total direct costs minus capital equipment and foreign travel (H - D - E)					
TOTAL INDIRECT COSTS				5,218	
TOTAL DIRECT AND INDIRECT COSTS (H + I)					
RESIDUAL FUNDS (IF FOR FURTHER SUPPORT OF CURRENT PROJECTS GPM 252 AND 253)				1,627	
AMOUNT OF THIS REQUEST (J) OR (J MINUS K)				$ 19,214	$

I/PD TYPED NAME & SIGNA
Franco Einaudi

DATE Sept. 14, 1982

NST. REP. TYPED NAME & SIGN
G. D. Hutchison

DATE Sept. 14, 1982

FOR NSF USE ONLY
INDIRECT COST RATE VERIFICATION

Date Checked	Date of Rate Sheet	Initials - DGC / Program

:F FORM 1030 (8 80) SUPERSEDES ALL PREVIOUS EDITIONS

*SIGNATURES REQUIRED ONLY FOR REVISED
BUDGET (GPM 2331)

Georgia Institute of Technology
A UNIT OF THE UNIVERSITY SYSTEM OF GEORGIA
ATLANTA, GEORGIA 30332
SCHOOL OF GEOPHYSICAL SCIENCES 404/894-3893

July 5, 1983

Mrs. Marilyn Rurak
1214, International Program
al Science Foundation
G Street NW
Washington, D.C. 20550

G-35-605, Eianudi, GeoSci

Dear Mrs. Rurak:

I was not able to talk to you over the telephone since you were travelling. I myself will be in Australia until the beginning of September and therefore have decided to follow the same procedure as I did last year. I am including the following items regarding my grant, "A Study of Internal Gravity Waves in the Po Valley.":

a) A report on the work performed up to date. At the end of this report you will find a brief statement of the work we intend to do during the third year of the grant.

b) A statement of other support for me.

c) A budget for the third year.

I hope that the enclosed documents are what you need to proceed with the funding of the third year. It is important that the funding arrives by the beginning of the Fall quarter so as to be able to pay the student salary.

dress until the end of August will be:

c/o Dr. J.J. Finnigan
CSIRO
Division of Environmental Mechanics
P.O. Box 821
Canberra City, A.C.T. 2601
Australia

Thank you and best wishes.

Sincerely,

Franco Eianudi

P.S. You will receive the official budget from the Office of Contracts. Also, for questions of an administrative nature, please call on Ms. Carol Cook at the above number. The unobliged funds are about $500.00.
encl.
FE/abg

XC: Reports Coordinator 2 copies
Annual Report

REPORT ON THE WORK PERFORMED DURING THE
PERIOD SEPT. 1, 1982-AUG. 31, 1983

i) Mr. Flavio Canavero has completed the transferring of the data originally collected on cassettes to magnetic tapes. (Mr. Canavero is a graduate student who has been on the grant since its beginning). As mentioned in my earlier report, this process, for reasons related to the original design of the cassettes, has turned out to be lengthier than expected. The microbarographs were located in the seven stations indicated in Appendix A: for each station, the days in April, May and June, 1982, during which good data is available are indicated as a function of time. Part of this period coincided with the ALPEX experiment.

The data has all been plotted as a function of time in graphs like the one of Appendix B: pressure is plotted as a function of time with a vertical scale which is adjusted for each twelve-hour record. The record refers to the station in Acgui for the 25th day of May, 1982.

The air temperature and the temperature of the sensor itself is also plotted as a function of time in blades of 24 hours. One such example is given in Appendix C.

One of the ongoing projects is the identification of cases when a periodic disturbance is present in the majority of the stations and is so clear that the identification can be carried out by visual inspection. One such an event is described in Appendix D when the pressure is plotted as a function of time for each of the seven stations. The pressure of the same periodic event in the record is evident in most of the records. The analysis of this event is in progress utilizing the techniques mentioned in my previous report. These techniques were prepared during the analysis of an event which occurred on May 9, 1979 in

the Midwest of the United States. This work has resulted in a paper by J.G. Stobie, L.W. Uccellini and myself entitled "A Case Study of Gravity Waves-Convective Storms Interaction: May 9, 1979", which has just been accepted in the Journal of the Atmospheric Sciences.

The objectives of studying events of this kind were described in my original proposal.

iii) The analysis of the data to produce the climatology of gravity waves in the Po Valley is also in progress. The information contained in these data is enormous and the analysis requires a good deal of care. A quick look at the data displayed in Appendices reveals that the pressure is highly nonstationary. We are in the process of deciding the best way to detrend and time average the data in order to produce the appropriate power spectra necessary to produce the climatology of gravity waves described in the proposal.

Plans for the third year

During this coming year, we expect to complete the climatology study mentioned in iii) and the analysis of case studies discussed in ii). Mr. Canavero has just passed his comprehensive examination and should be working on these projects as part of his Ph.D. dissertation.

APPENDIX A

Solid line indicates that the microbaragraph record is available.

Appendix A:

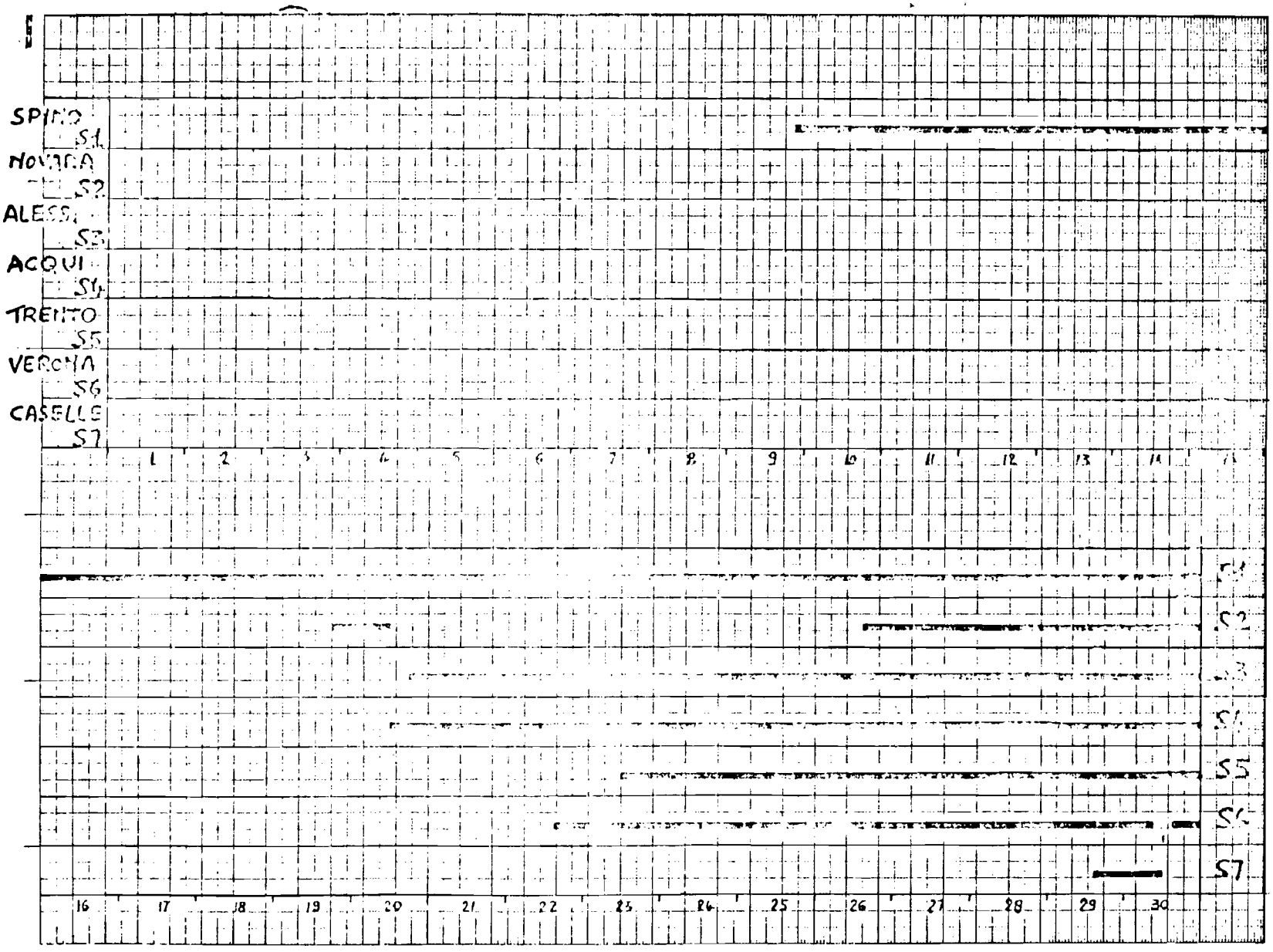

APRIL

Appendix A

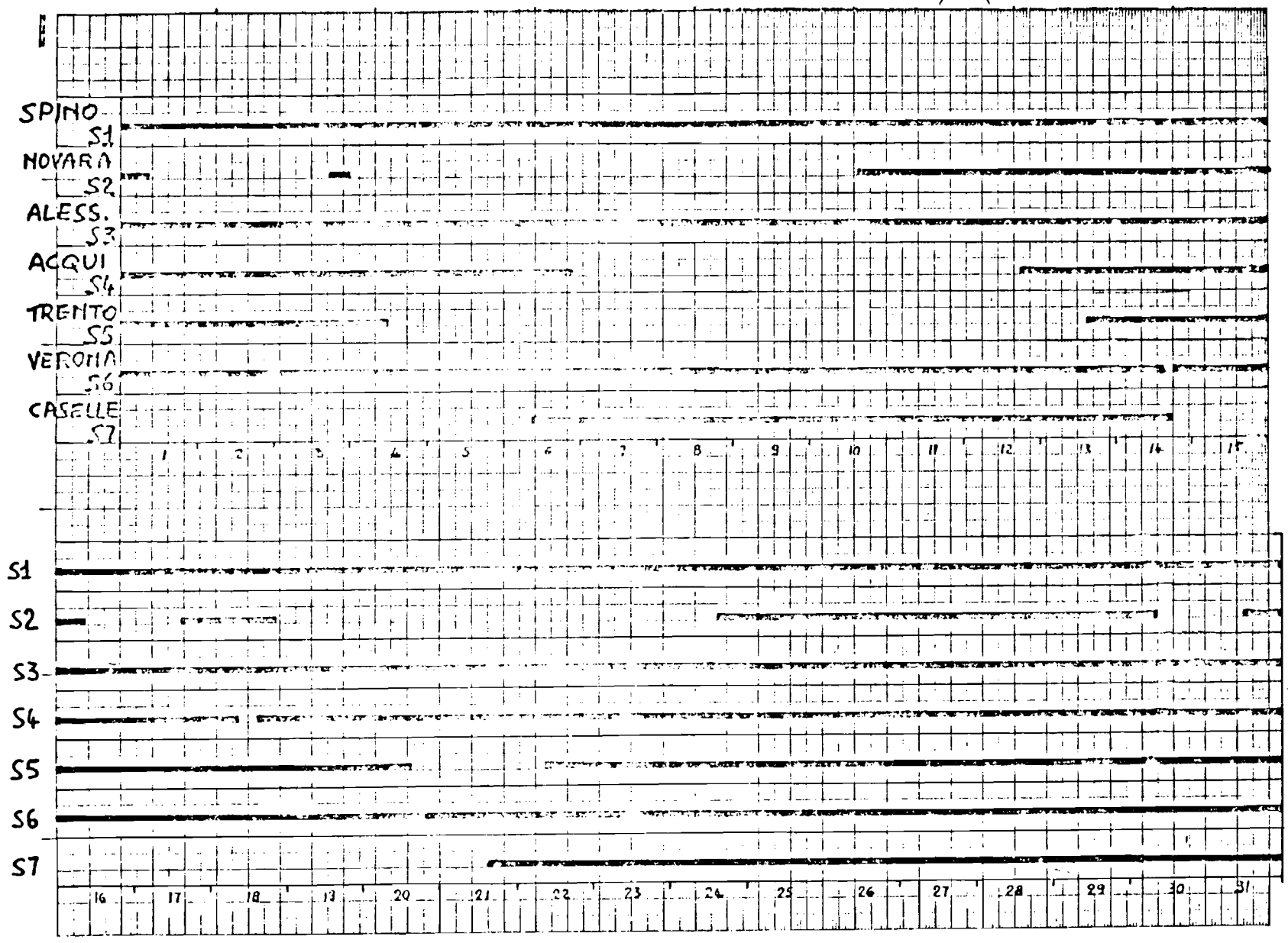
SPINO S1
NOVARA S2
ALESS. S3
ACQUI S4
TRENTO S5
VERONA S6
CASELLE S7
1 2 3 4 5 6 7 8 9 10 11 12 13 14 15
S1
S2
S3
S4
S5
S6
S7
16 17 18 19 20 21 22 23 24 25 26 27 28 29 30 31
MAY

Appendix A

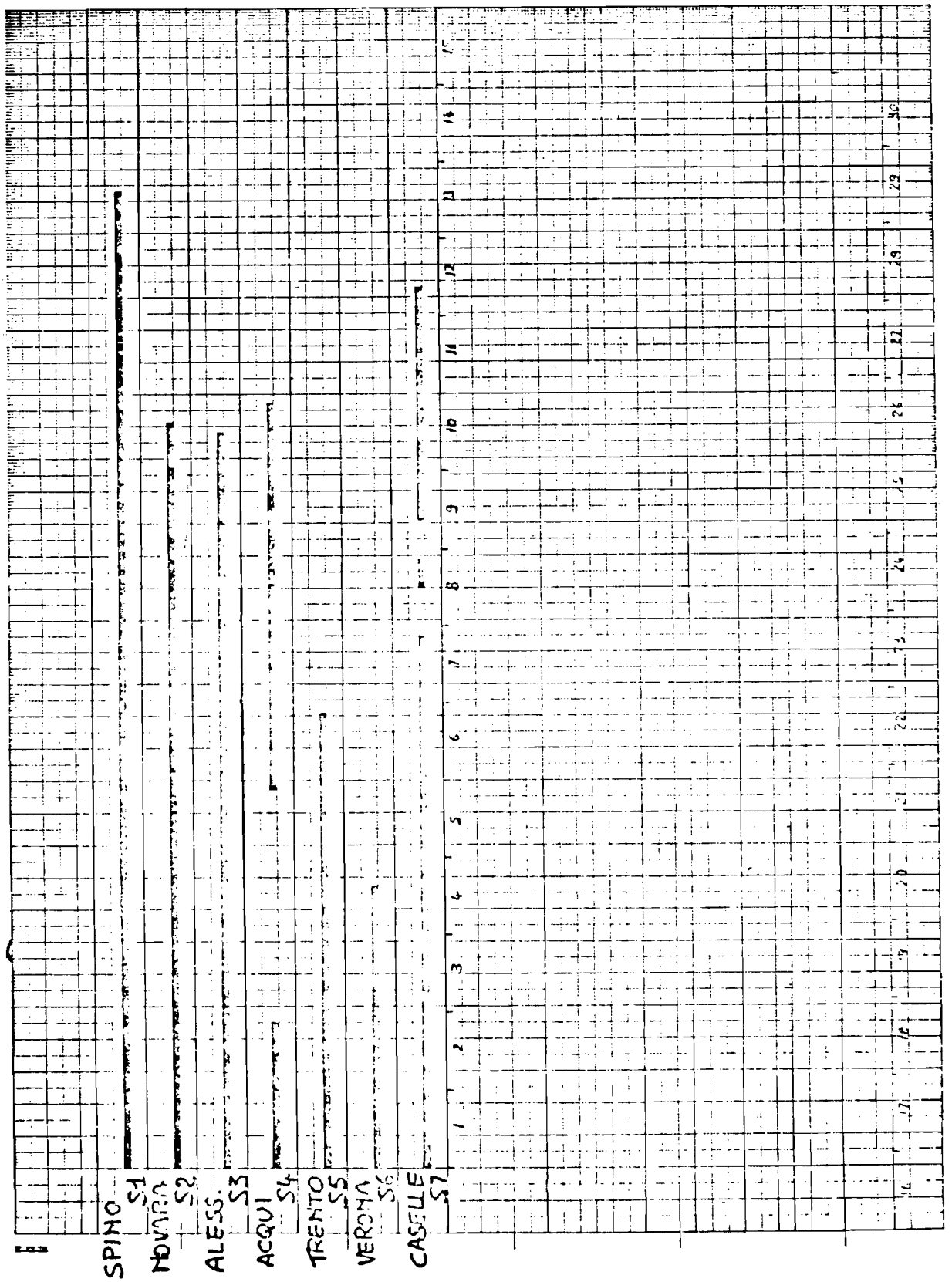
JUNE
SPINO S1
NOVARA S2
ALESS. S3
ACQUI S4
TRENTO S5
VERONA S6
CASELLE S7

APPENDIX B

PRESSURE RECORD AS A FUNCTION OF TIME FOR ACQUI, STATION #4.

THE VERTICAL SCALE IS ADJUSTED FOR EACH 12 HOUR TIME BLOCK.

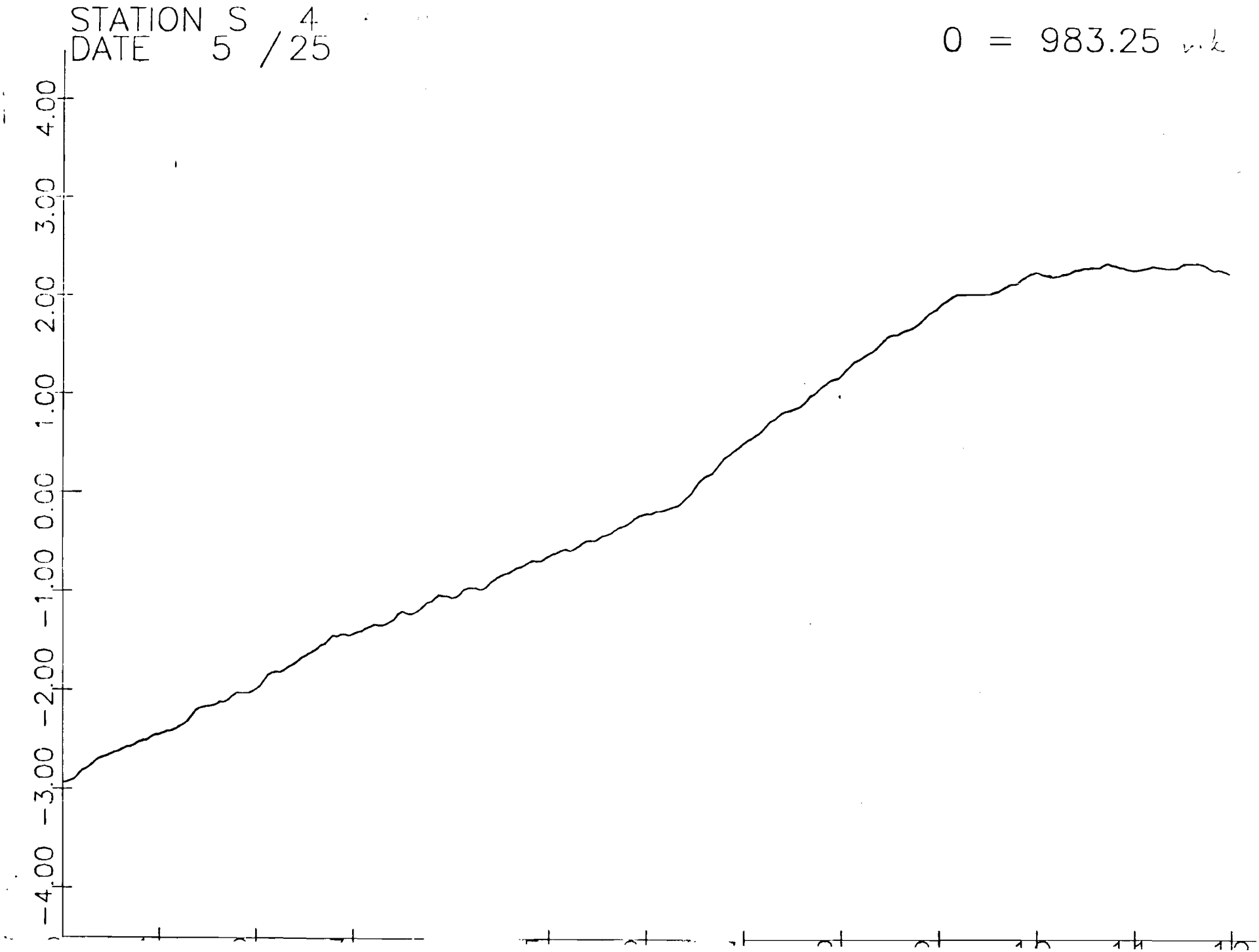
STATION S 4
DATE 5 / 25
0 = 983.25 mb
4.00
3.00
2.00
1.00
0.00
-1.00
-2.00
-3.00
-4.00

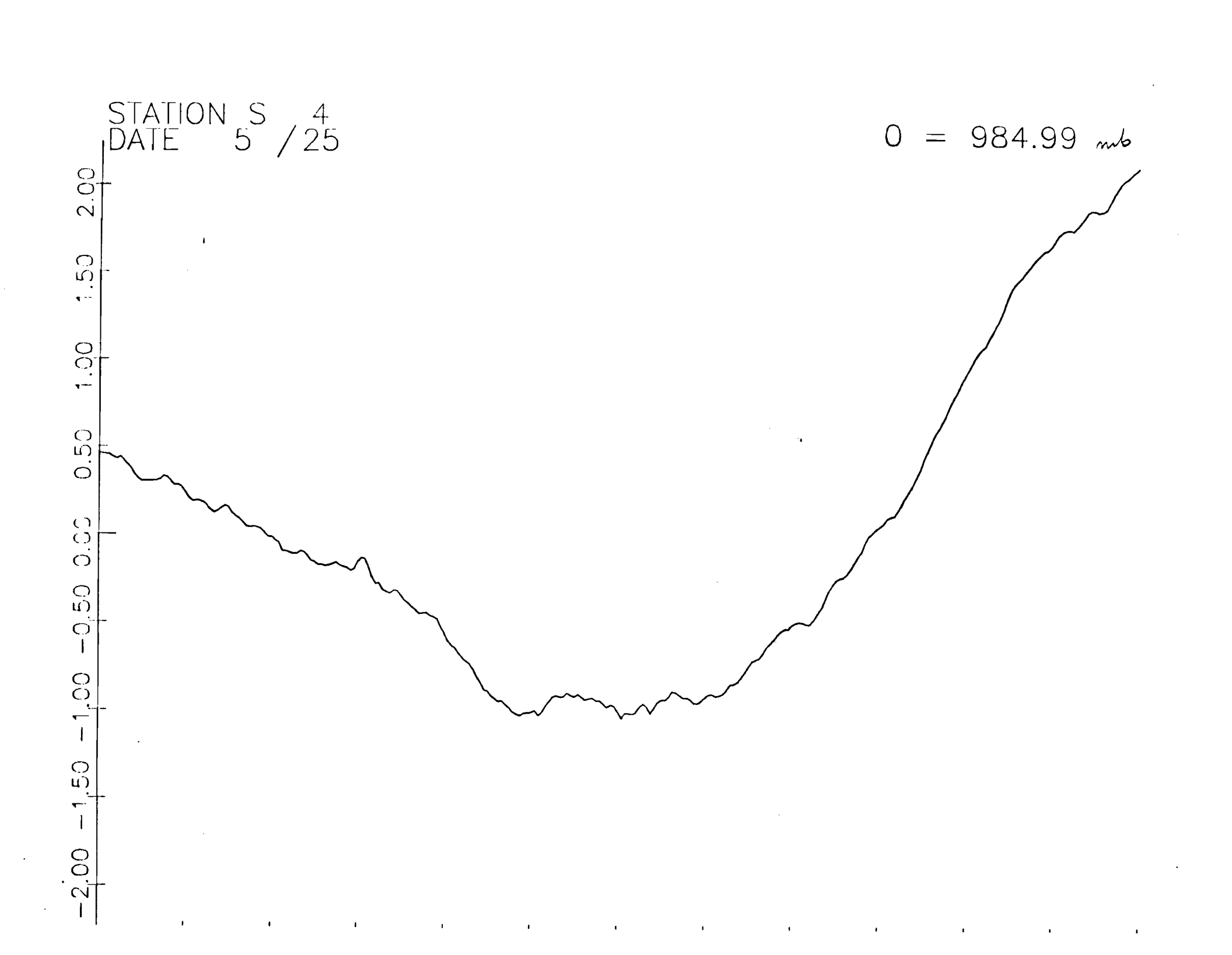
STATION S 4
DATE 5 / 25
0 = 984.99 mb
2.00
1.50
1.00
0.50
0.00
-0.50
-1.00
-1.50
-2.00

APPENDIX C

AIR TEMPERATURE NEAR THE GROUND AND TEMPERATURE OF THE SENSOR AS A FUNCTION OF TIME.

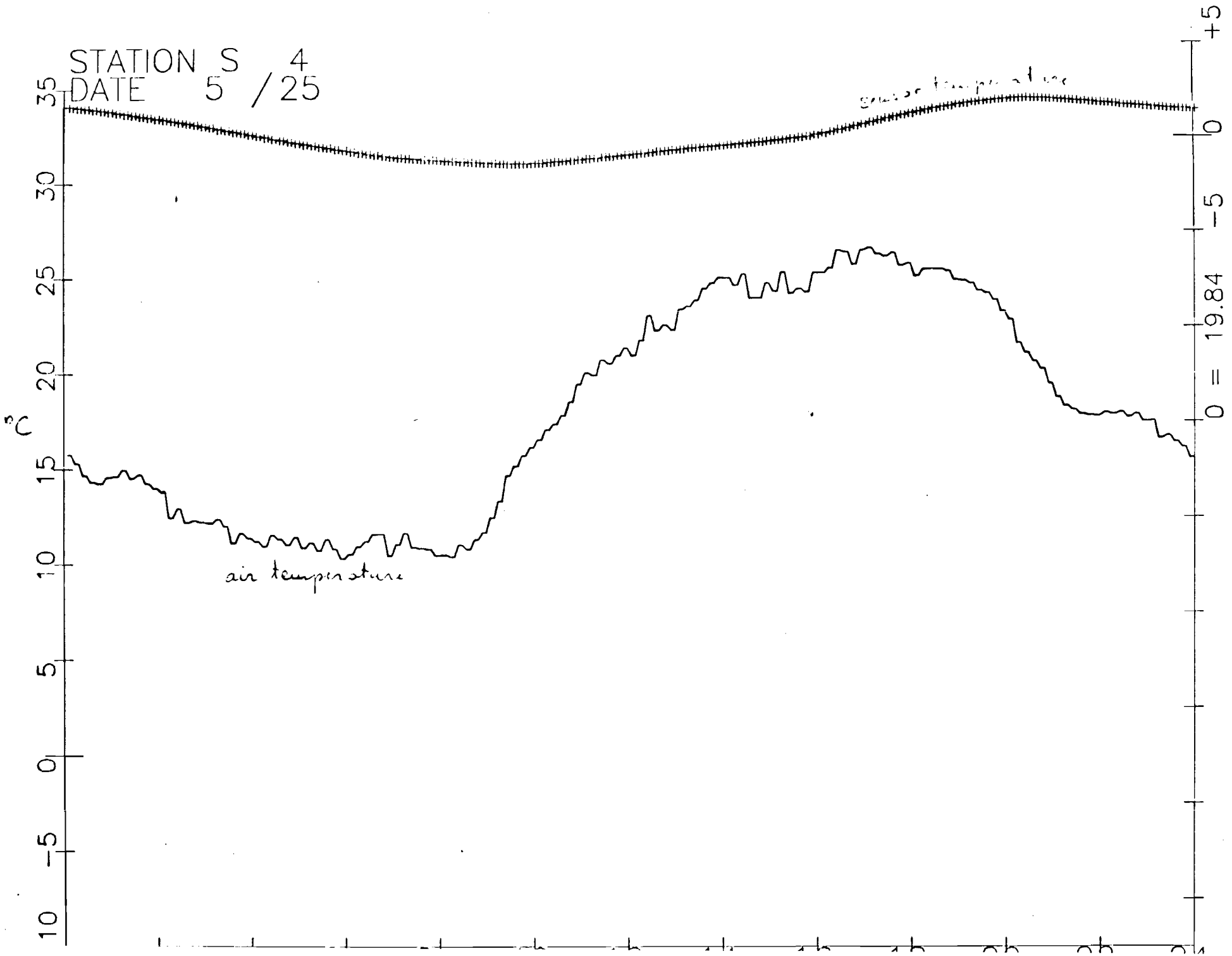
STATION S 4
DATE 5 / 25
35
30
25
20
15
10
5
0
-5
10
°C
+5
0
-5
0 = 19.84
air temperature

APPENDIX D

PRESSURE AS A FUNCTION OF TIME FOR AN EVENT DURING MAY 25, 1982. THE PRESSURE TRACES ARE GIVEN FOR EACH STATION: THE REFERENCE PRESSURE IS ARBITRARY AND THE TRACE IS TRANSLATTED VERTICALLY WHENEVER NECESSARY SO AS TO HAVE MAXIMUM VERTICAL SCALE RESOLUTION.

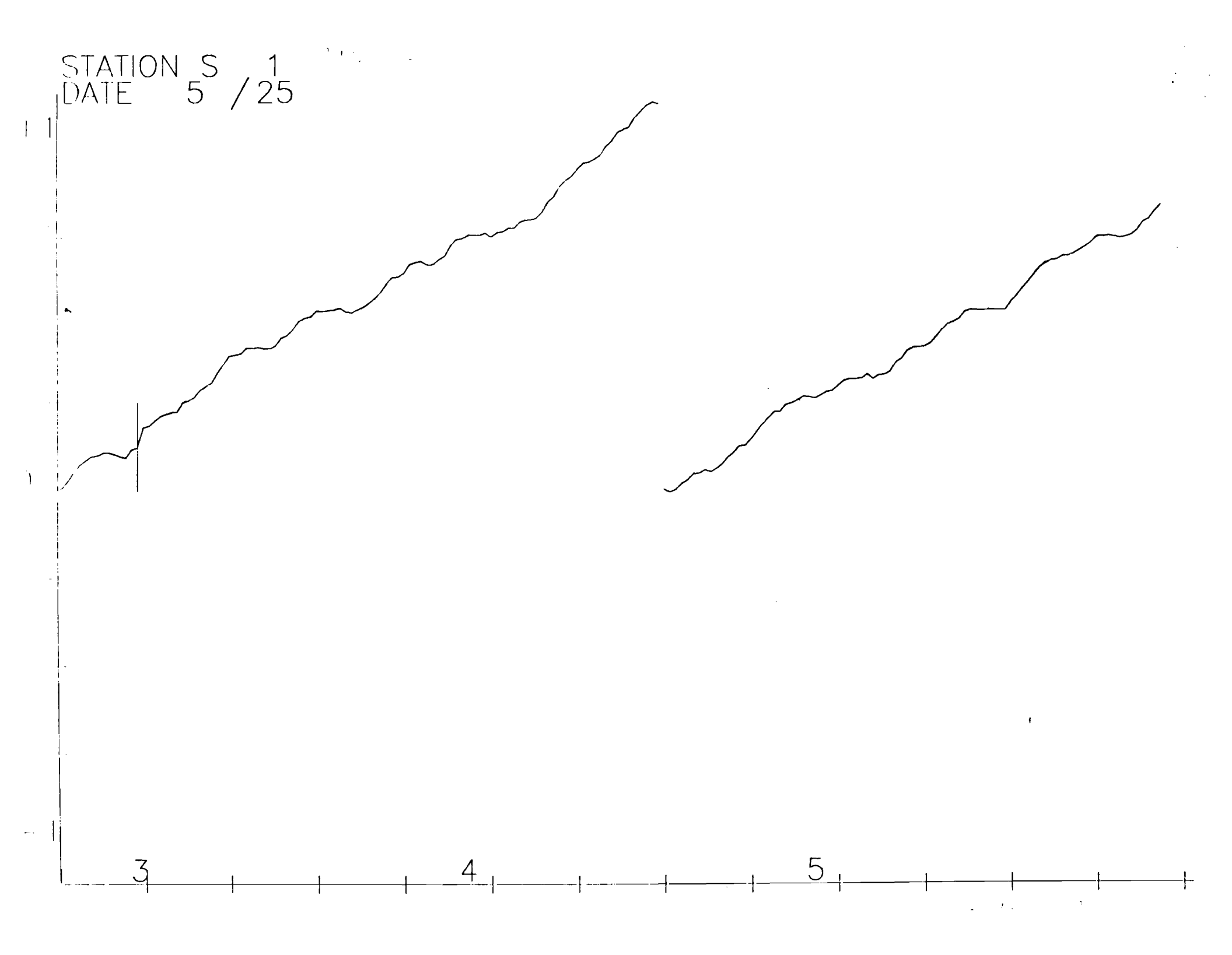
STATION S 1
DATE 5 / 25
3
4
5

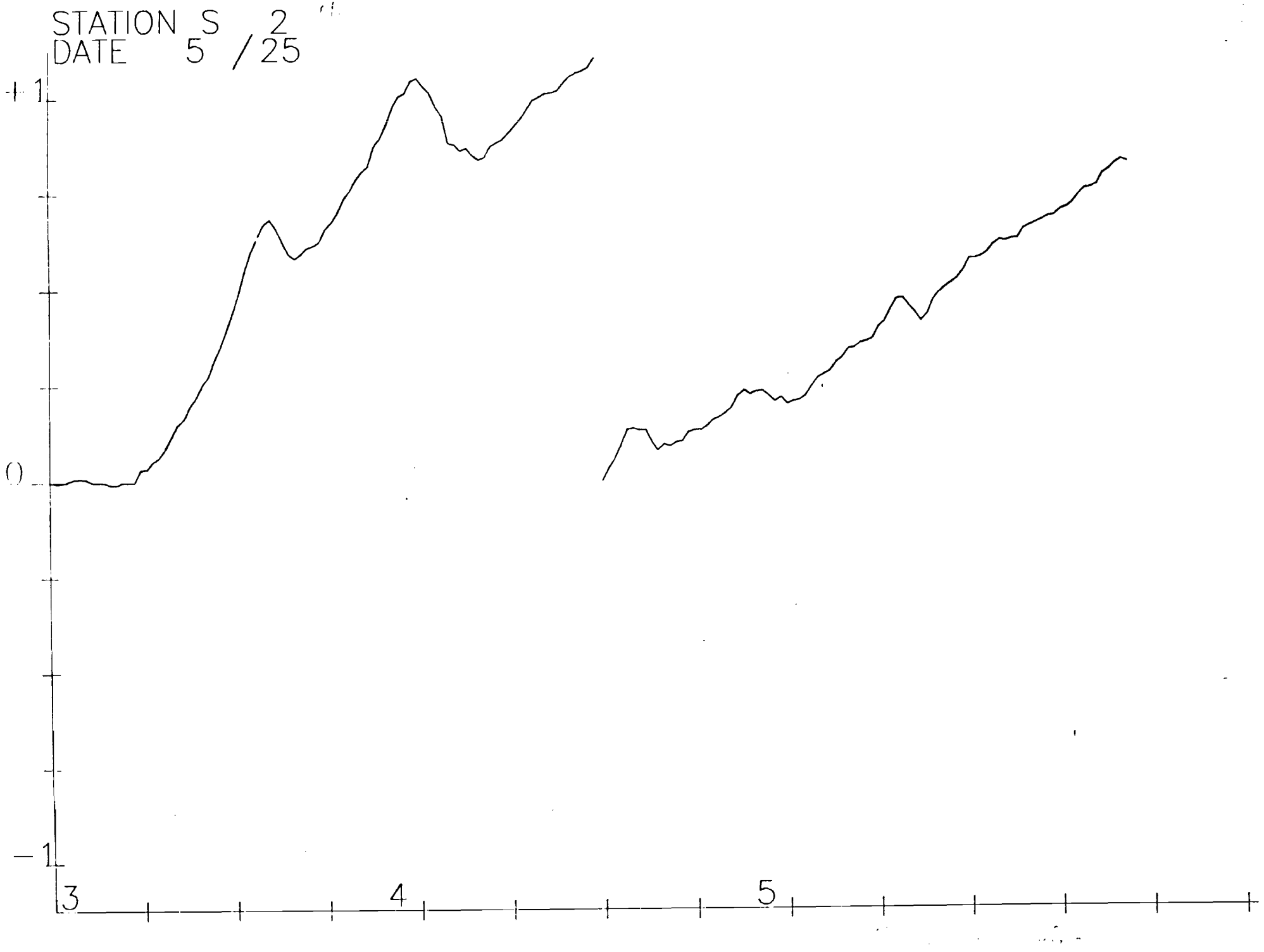
STATION S 2
DATE 5 / 25
+1
0
−1
3
4
5

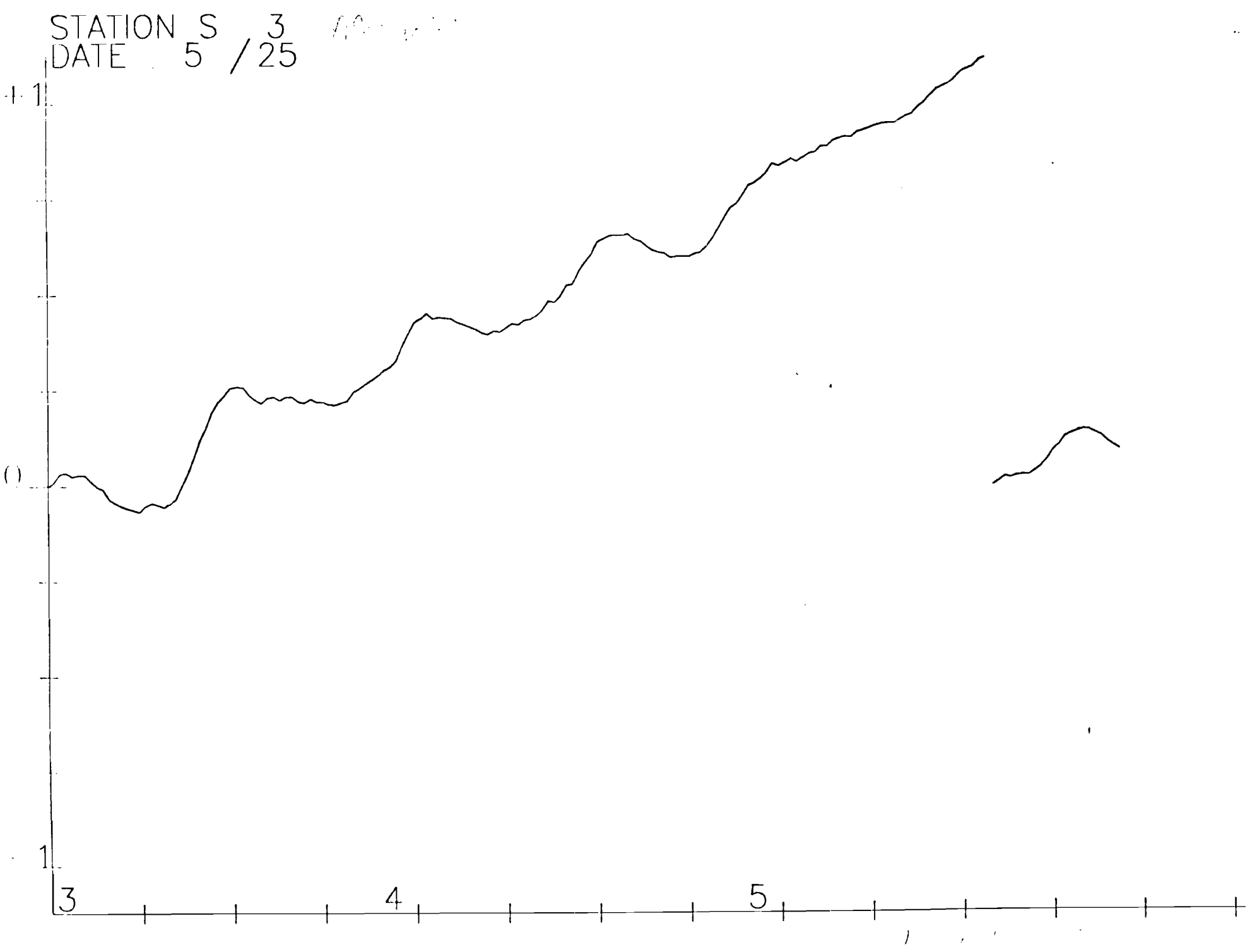
STATION S 3
DATE 5 / 25
1
0
1
3
4
5

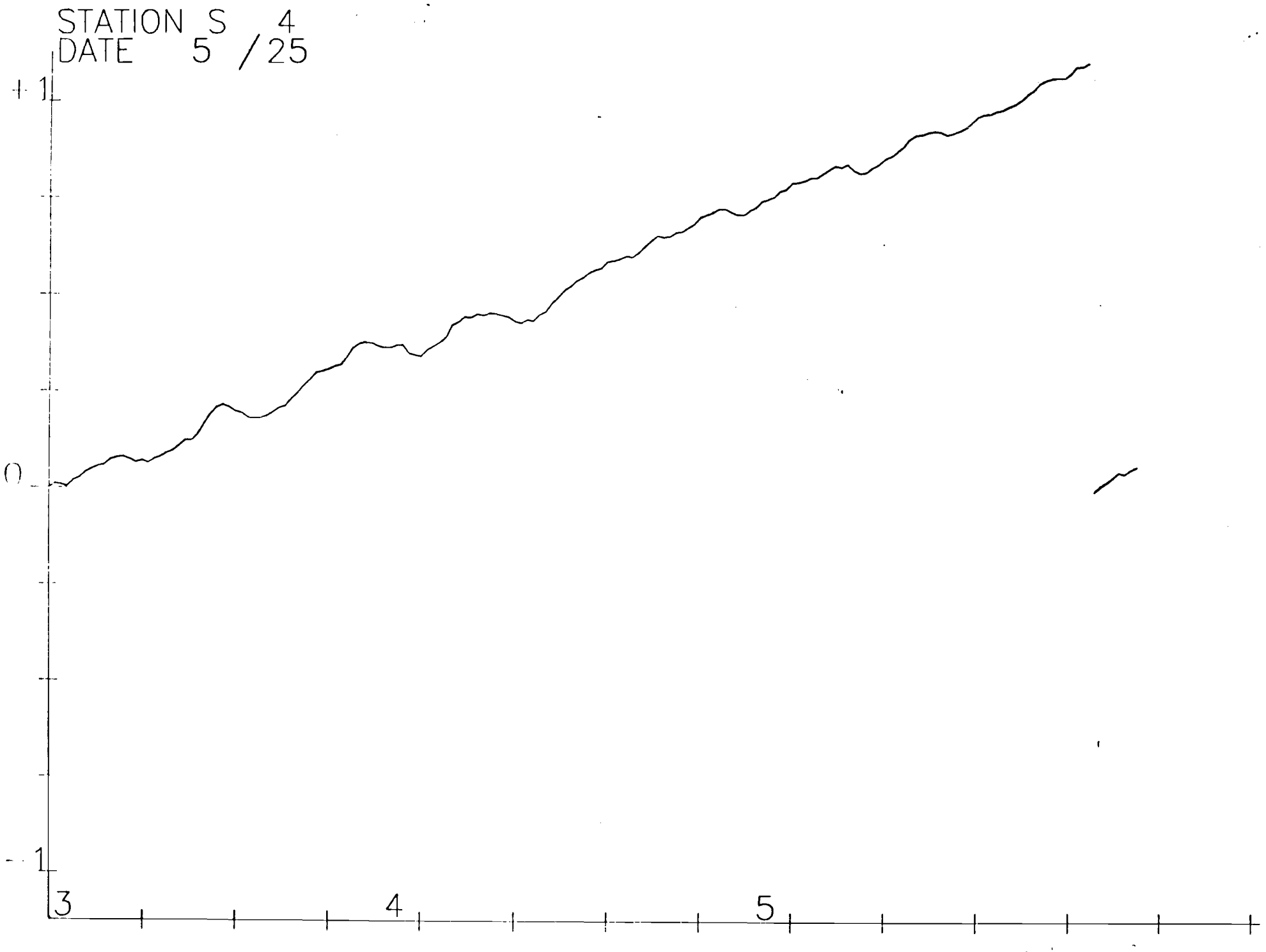
STATION S 4
DATE 5 / 25
+1
0
-1
3
4
5

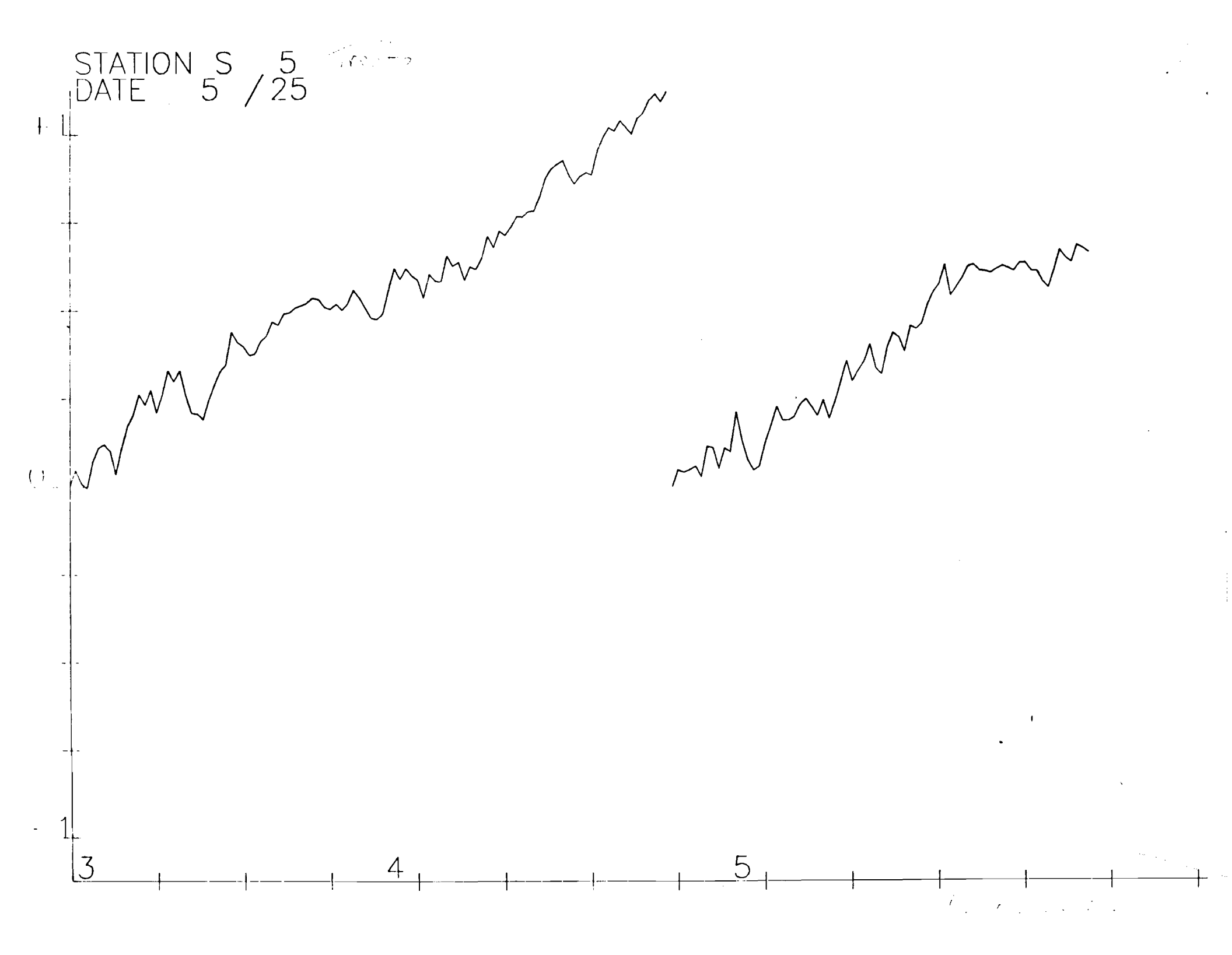
STATION S 5
DATE 5 / 25
1
3
4
5

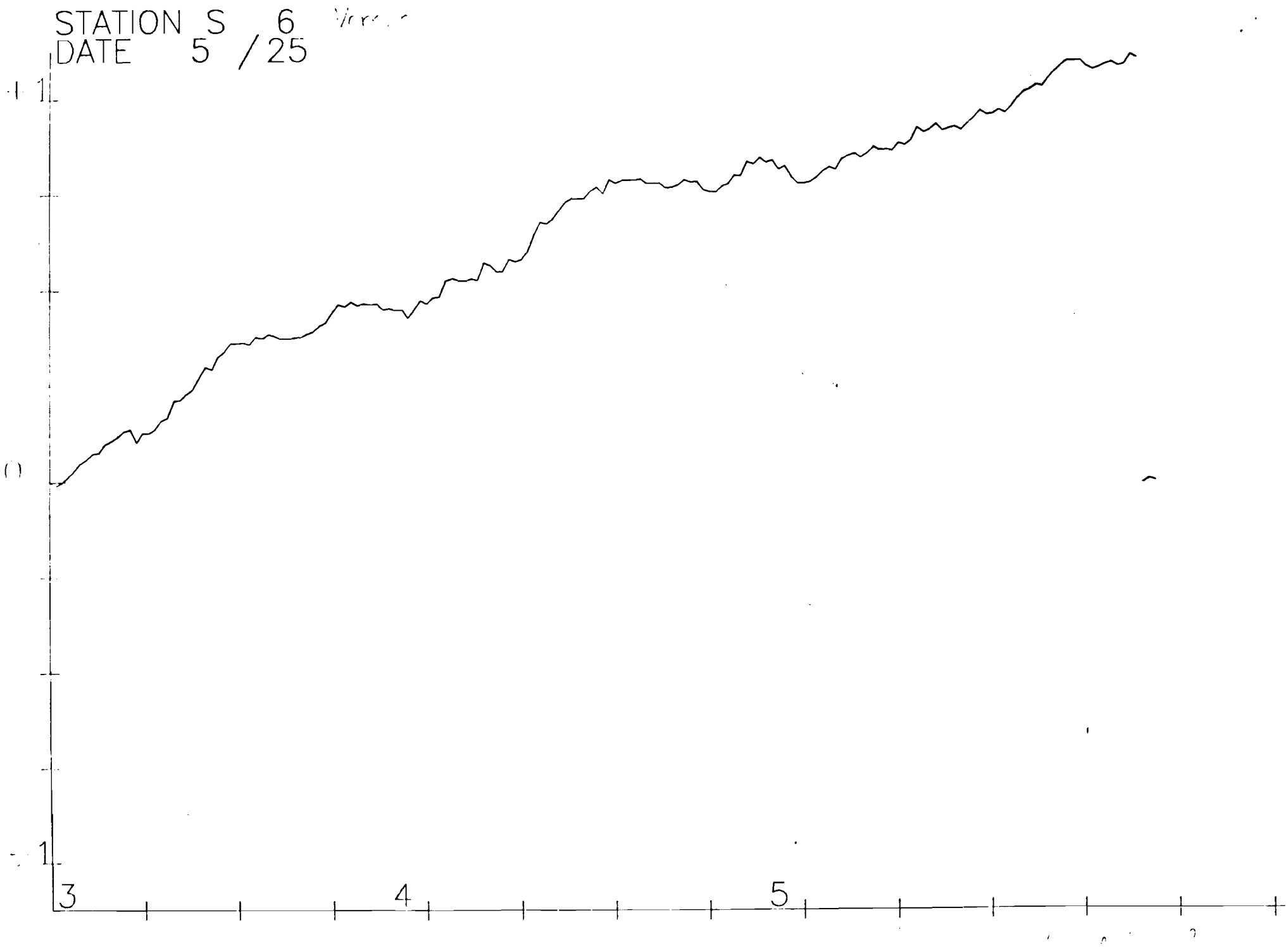
STATION S 6
DATE 5 / 25
1
0
1
3
4
5

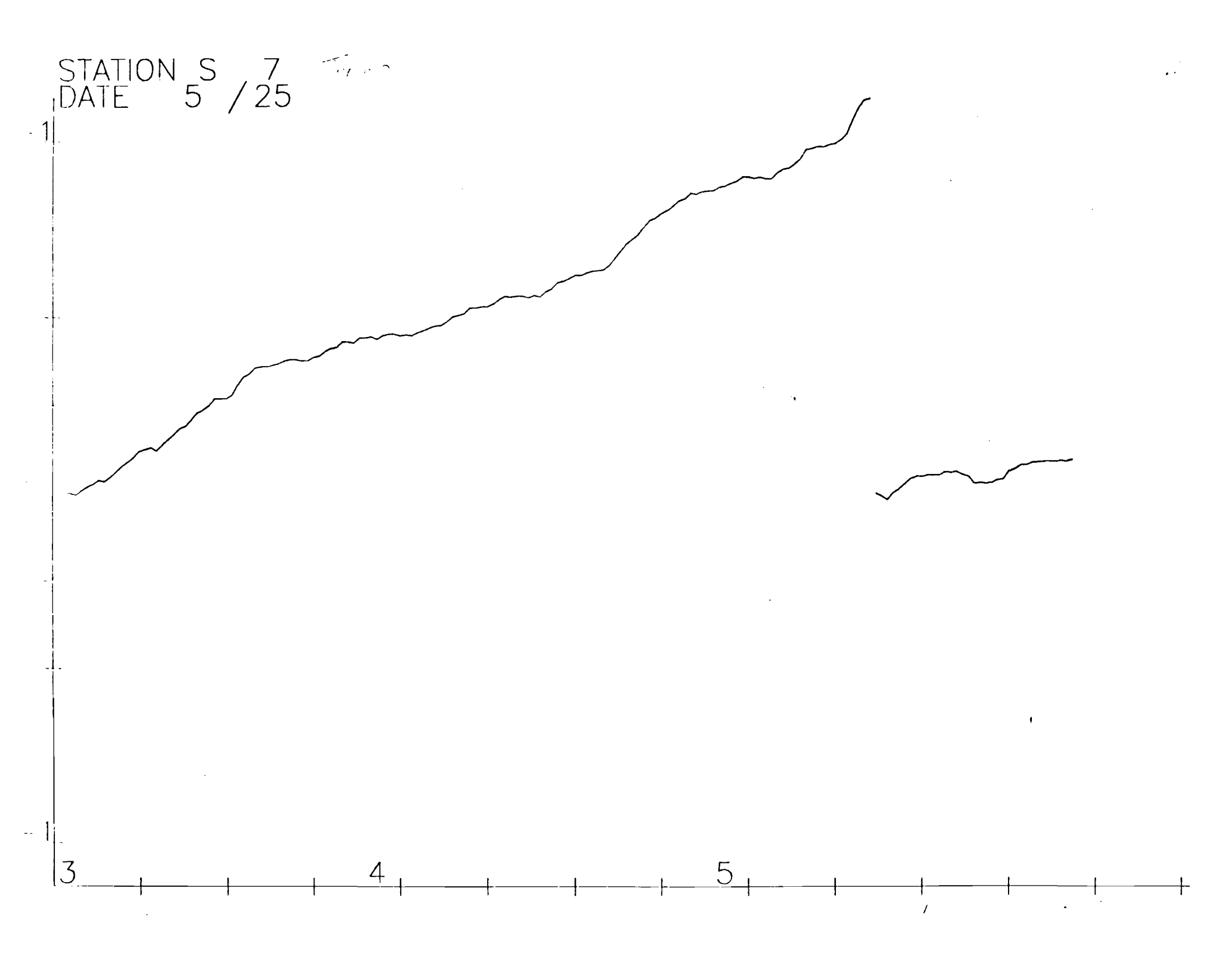
STATION S 7
DATE 5 / 25
1
1
3
4
5

Current and Pending Support for Franco Einaudi

Franco Einaudi has received a 3-year grant from the National Seience Foundation titled "An investigation of the interaction between turbulence and propagating internal gravity waves in the planetary boundary layer." Franco Einaudi has three months' salary/year on this grant.

NATIONAL SCIENCE FOUNDATION
Washington, D.C. 20550

FINAL PROJECT REPORT
NSF FORM 98A

PLEASE READ INSTRUCTIONS ON REVERSE BEFORE COMPLETING

PART I-PROJECT IDENTIFICATION INFORMATION

1. Institution and Address	2. NSF Program	3. NSF Award Number
School of Geophysical Sciences Georgia Institute of Technology Atlanta, GA 30332	International Programs	INT-8105101
	4. Award Period From 9/1/81 To 2/28/85	**5. Cumulative Award Amount** $ 61,969

6. Project Title

A Study of Internal Gravity Waves in the Po Valley

PART II-SUMMARY OF COMPLETED PROJECT *(FOR PUBLIC USE)*

The following research has been carried out during the period of this grant:
1) A complete set of microbarograph pressure records were collected in the Po Valley during the Spring of 1982. The microbarographs were located in the seven stations indicated in Appendix A. The graphs indicate, as a function of time, the data collected for each station in April, May, and June of 1982. Part of this period coincided with the ALPEX experiment.
2) A set of programs designed to identify and relate gravity waves and thunderstorms was developed and successfully applied to an event which occurred in the United States on May 9, 1979. These programs include FFT and maximum entropy methods for calculating the spectra of pressure signals and cross-correlation techniques to calculate the amplitude and direction of phase propagation. In this event, we have shown that gravity waves and storms develop and propagate together. We provide further evidence about the role of gravity waves in organizing convection.
3) A climatological study of the time and space variability of spectral estimates of pressure at two of the stations has been successfully completed. Of these stations, Station A is in the plains and Station B in the foothills of the Dolomites.

The study reveals new and important phenomena concerning the behavior of atmospheric spectra. First, pressure records are intrinsically nonstationary; thus, one should more properly deal with evolutionary spectra, which account for time variation, rather than stationary ones. Secondly, a relationship exists between a given frequency range and a corresponding nonstationarity scale, i.e., the time beyond which the nonstationarity sets in. Thirdly, spectra show a substantial variability in time with their shape and energy content depending on different time segments. Finally, important differences in the spectra exist between Stations A and B which indicate substantial effects of topography, particularly for periods below 40 min. The results of this work suggest that nonstationarity of the pressure spectra is an important element for our understanding of atmospheric and oceanic dynamics.

PART III-TECHNICAL INFORMATION *(FOR PROGRAM MANAGEMENT USE)*

1. ITEM *(Check appropriate blocks)*	NONE	ATTACHED	PREVIOUSLY FURNISHED	TO BE FURNISHED SEPARATELY TO PROGRAM	
				Check (✓)	Approx. Date
a. Abstracts of Theses		Appendix B			
b. Publication Citations		Appendix C			
c. Data on Scientific Collaborators		Appendix D			
d. Information on Inventions	X				
e. Technical Description of Project and Results		Appendix E			
f. Other *(specify)*					

2. Principal Investigator/Project Director Name *(Typed)*	3. Principal Investigator/Project Director Signature	4. Date
Franco Einaudi		10/16/85

Appendix A

Solid line indicates that the microbarograph record is available.

Appendix A :

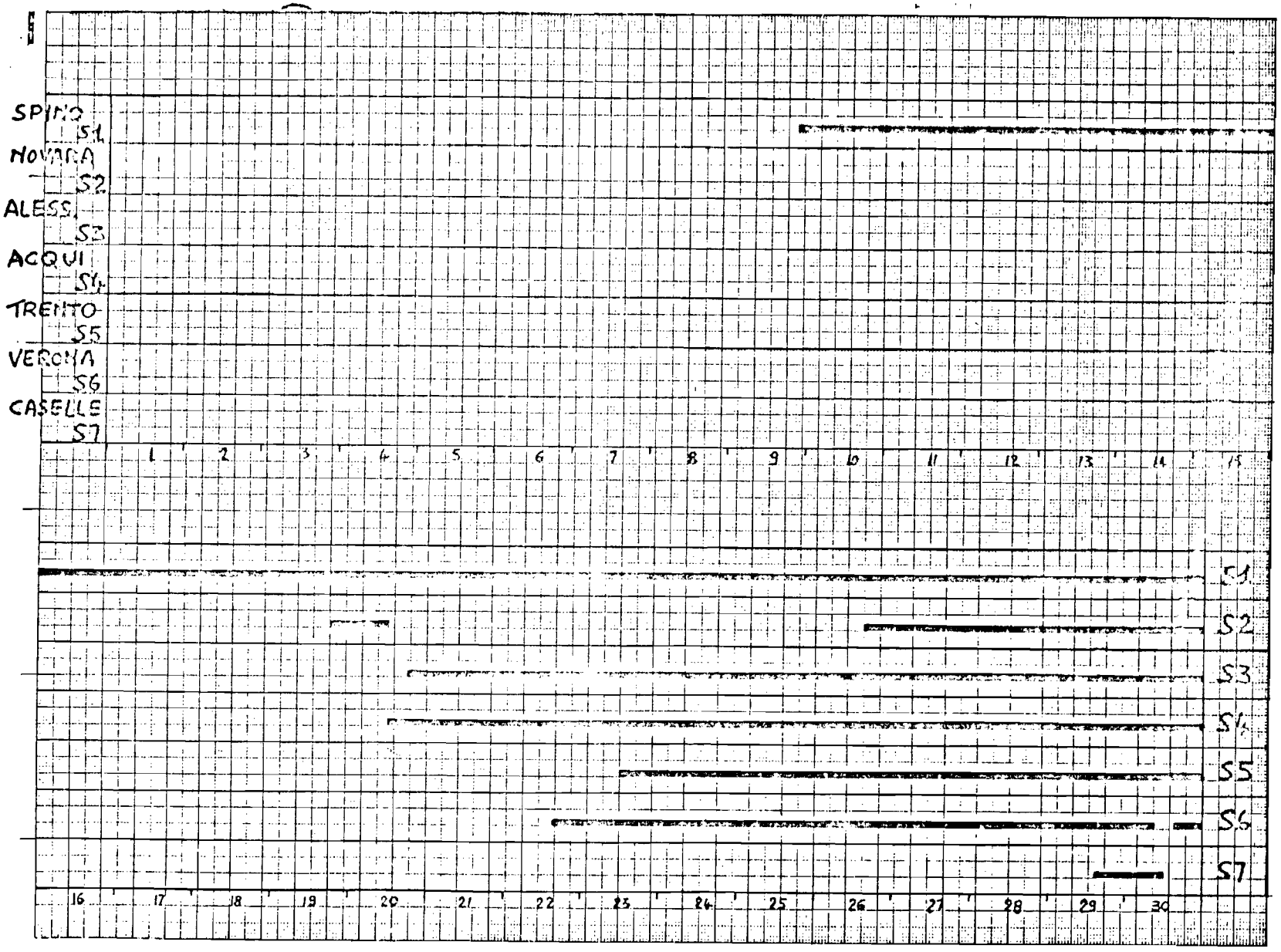
SPINO S1
NOVARA S2
ALESSI S3
ACQUI S4
TRENTO S5
VERONA S6
CASELLE S7
1 2 3 4 5 6 7 8 9 10 11 12 13 14 15
16 17 18 19 20 21 22 23 24 25 26 27 28 29 30
S1
S2
S3
S4
S5
S6
S7
APRIL

Appendix A

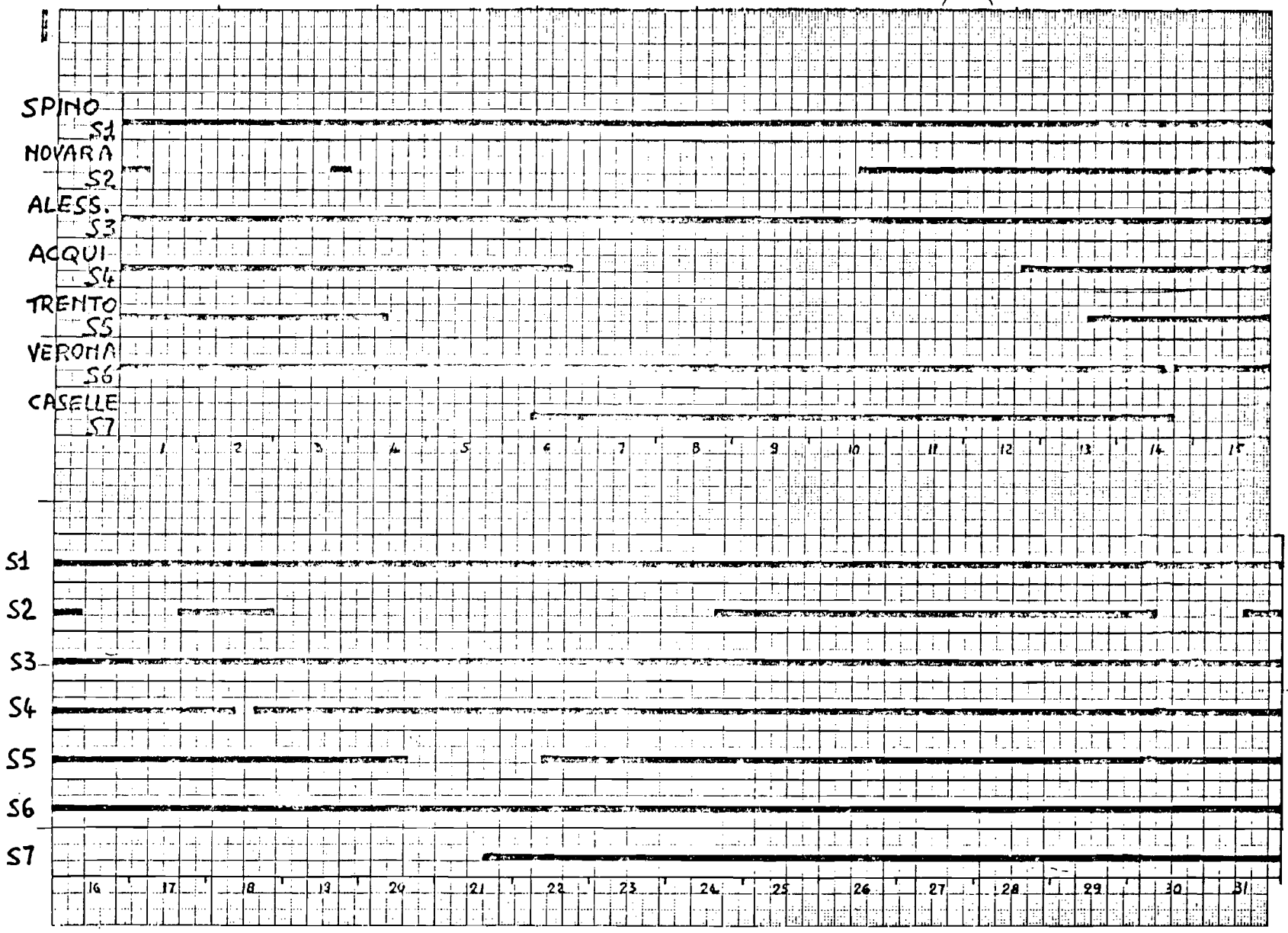
SPINO S1
NOVARA S2
ALESS. S3
ACQUI S4
TRENTO S5
VERONA S6
CASELLE S7
1 2 3 4 5 6 7 8 9 10 11 12 13 14 15
S1
S2
S3
S4
S5
S6
S7
16 17 18 19 20 21 22 23 24 25 26 27 28 29 30 31
MAY

Appendix A

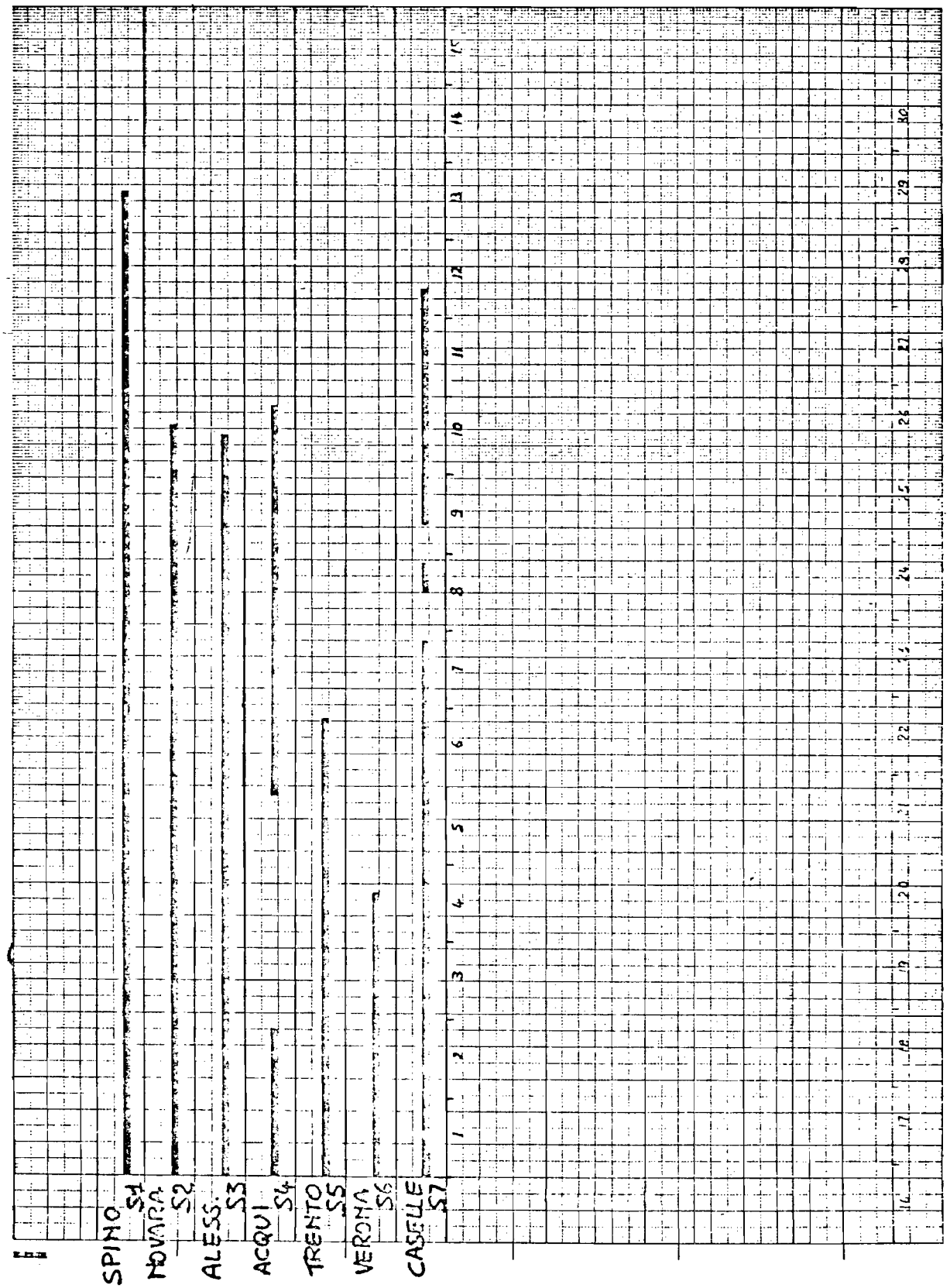
JUNE
SPINO S1
NOVARA S2
ALESS. S3
ACQUI S4
TRENTO S5
VERONA S6
CASELLE S7

Appendix B

SEP 12 1985

GEORGIA INSTITUTE OF TECHNOLOGY

Office of
Graduate Studies and Research

Date September 12, 1985

REQUEST FOR APPROVAL OF THESIS TOPIC

NAME Flavio (First) Giovanni (Middle) Canavero (Last)

requests approval to prepare and present a thesis in partial fulfillment of the requirements for the degree of Doctor of Philosophy in Geophysical Sciences

Thesis Title: Variability of atmospheric pressure spectra in the Po Valley.

Brief description:

The purpose of this thesis is to analyze the temporal and spatial behavior of atmospheric pressure spectra. The literature shows many examples of pressure, wind and temperature spectra whose shapes display a remarkable degree of universality. Theories relaying either on turbulence or internal waves have been suggested to account for such spectra. A serious difficulty exists in explaining the intermediate scales, the so-called mesoscale range, within which much more energy appears to exist than theory would predict.

As a preliminary step for our understanding of the physical mechanisms underlying the spectral behavior, a detailed analysis of the surface pressure has been carried out having in mind to test the temporal and spatial variability of these spectra. The source of the data were two microbarograph stations in the Po Valley, 275 km apart, one in the plains 50 km South of the Alps, the other in the foothill of the Dolomites. The 60-day record was part of the Alpine Experiment (ALPEX) which took place in 1982.

The study reveals new important phenomena concerning the behavior of atmospheric spectra: (1) pressure records are intrinsecally nonstationary and thus one should more properly be dealing with evolutionary spectra which account for time variations. The spectral estimation technique has to be carefully devised to minimize leakage and give acceptable confidence limits. (2) A relationship exists between a given frequency range and a corresponding nonstationarity scale, i.e. the time beyond which the nonstationarity sets in. (3) Spectra show a substantial variability in time with their shape and energy content depending on different time segments. Particular examples of such a dependence of spectra on time of day and large scale weather phenomena are discussed. (4) Important differences of the spectra exist between the two stations indicating substantial effect of topography, particularly for periods below 40 min. The results of this work suggest that nonstationarity of the pressure spectra are important elements for our understanding of atmospheric and oceanic dynamics.

Approved:

Director of School

Thesis Advisor

Member Reading Committee or Thesis Advisory Committee

Member Reading Committee or Thesis Advisory Committee

Signature of Graduate Student

33666
Campus P. O. Box

9/19/85
Dean, Office of Graduate Studies and Research

Prepare original only. Graduate Office will distribute copies.

Appendix C

PUBLICATIONS

J.G. Stobie, F. Einaudi and L.W. Uccellini, 1983: "A Case Study of Gravity Waves-Convective Storms Interaction: 9 May 1979". J. Atmos. Sci., 40, 2804-2830. Appendix F1.

D. Fua and F. Einaudi, 1984: "On the Effect of Dissipation on Shear Instabilities in the Stable Atmospheric Boundary Layer". J. Atmos. Sci., 41, 888-900. Appendix F2.

F. Canavero and F. Einaudi: "Time and Space Variability of Spectral Estimates of Atmospheric Pressure". To be submitted to J. Atmos. Sci. Appendix F3.

Appendix D

SCIENTIFIC COLLABORATORS

Dr. J.G. Fua	Senior research scientist; National Research Council Rome, Italy
Dr. J.G. Stobie	Air Force Global Weather Central; Offutt AFB, NE 68113 Graduate student at the time of his involvement with this project.
Flavio Canavero	Ph. D. student who should receive his degree in January, 1986. He has been on this grant through most of his work and his Ph. D. dissertation summary is included as Appendix B.

Appendix E

The pressure data collected in the Po Valley is summarized in Appendix A. The data has a nominal resolution of 4.5 μbar and has been averaged over 10 sec.

One of the original objectives of the proposal was to identify gravity waves and correlate them with convective activities identified by a weather radar in the vicinity of Turin. This failed to be feasible, because of difficulties with the radar. However, FFT, maximum entropy and cross-correlation techniques were used to analyze pressure disturbances in the north central United States and relate them to storm activities in that same area. Thus, we have analyzed an equivalent problem in a different geophysical area. The result of the analysis is described in the paper by Stobie, Uccellini, and myself (see Appendix F1). We show that in the 9 May 1979 event, convective cells and observed gravity waves form a closely linked system with cell intensity, height, and associated rainfall maximized at the wave ridge. The paper provides further evidence of the important role that gravity waves play in mesoscale dynamics.

The second result of the research is described in the paper enclosed here as Appendix F3. In this paper, we analyze the temporal and spatial behavior of atmospheric pressure spectra collected at two of the stations in the Po Valley. The literature shows many examples of pressure, wind and temperature spectra whose shapes display a remarkable degree of universality. Theories relying either on turbulence or internal waves have been suggested to account for such spectra. A serious difficulty exists in explaining the intermediate scales, the so-called mesoscale range, within which much more energy appears to exist than theory predicts.

As a preliminary step for our understanding of the physical mechanisms underlying the spectral behavior, a detailed analysis of the surface pressure has been carried out with the intent to test the temporal and spatial variability of these spectra. We have done so by analyzing the data at two stations in the Po Valley, 275 km apart, one in the plains 50 km south of the Alps and the other in the foothills of the Dolomites.

The study reveals new and important phenomena concerning the behavior of atmospheric spectra: 1) Pressure records are intrinsically nonstationary; thus, one should more properly deal with evolutionary spectra which accounts for time variations. The spectral estimation technique has to be carefully devised to minimize leakage and give acceptable confidence limits. 2) A relationship exists between a given frequency range and a corresponding nonstationarity scale, i.e., the time beyond which the nonstationarity sets in. 3) Spectra show a substantial variability in time with their shape and energy content depending on different time segments. 4) Important differences in the spectra exist between the two stations, which indicate the substantial effect of topography, particularly for periods below 40 min. The results of this work suggest that nonstationarity of the pressure spectra is an important element for our understanding of atmospheric and oceanic dynamics.

A Case Study of Gravity Waves–Convective Storms Interaction: 9 May 1979

JAMES G. STOBIE AND FRANCO EINAUDI

LOUIS W. UCCELLINI

Reprinted from JOURNAL OF THE ATMOSPHERIC SCIENCES, Vol. 40, No. 12, December 1983
American Meteorological Society
Printed in U. S. A.

Reprinted from JOURNAL OF THE ATMOSPHERIC SCIENCES, Vol. 40, No. 12, December 1983
American Meteorological Society
Printed in U. S. A.

A Case Study of Gravity Waves–Convective Storms Interaction: 9 May 1979

JAMES G. STOBIE AND FRANCO EINAUDI

LOUIS W. UCCELLINI

A Case Study of Gravity Waves–Convective Storms Interaction: 9 May 1979

JAMES G. STOBIE[1] AND FRANCO EINAUDI

School of Geophysical Sciences, Georgia Institute of Technology, Atlanta, GA 30332

LOUIS W. UCCELLINI

Goddard Laboratory for Atmospheric Sciences, NASA/Goddard Space Flight Center, Greenbelt, MD 20771

(Manuscript received 20 April 1983, in final form 24 July 1983)

ABSTRACT

An analysis is presented of a series of severe storms which occurred in the north central United States on 9 May 1979 and whose spatial distribution and movement correlate well with observed gravity waves. Two gravity wave trains of 2.1–3 mb amplitude, 2.5–3.3 h period and 240–265 km horizontal wavelength were isolated through power spectra analysis and cross-correlation techniques applied to National Weather Service barograph traces. The wave trains propagated in the 200° direction, which coincided with the jet axis, with a phase velocity of 20–30 m s^{-1} and within a 300 km wide band. The storms were identified on enhanced infrared GOES satellite pictures with the help of radar summaries. These convective systems initially developed in Nebraska and propagated north-northeast at 25 m s^{-1}, revealing wave-like characteristics with a separation of 300–400 km. The convective systems were closely linked to the observed wave trains with cell intensity, height and associated rainfall maximized at the wave ridge. One of the two wave trains developed in regions of weak or no convection and appeared to initiate more intense convective clusters downstream from the point of origin. It is shown that the characteristics of the wave trains are consistent with those of gravity waves generated in a region of strong vertical shear associated with the jet. It is suggested that the wave trains continue to extract energy from the basic state all along their track through critical level interaction.

1. Introduction

In the last few years, progress has been made in understanding the interaction between internal gravity waves, water vapor and deep convection. This progress is largely due to detailed case studies combined with the advent of the new remote sensing techniques of satellite imagery and Doppler radar. The new data reveal that various phenomena involving condensation and precipitation are often organized with spatial and temporal scales well within the gravity wave domain.

Recent papers by Testud *et al.* (1980) and Wang *et al.* (1983) (see also references therein) provide a detailed analysis of wave-like rainbands associated with a cold front. These rainbands are essentially oriented perpendicular to the cold front and are explained in terms of shear instability within the frontal zone. The horizontal wavelengths and periods are of the order of a few kilometers and a few minutes, respectively. Balachandran (1980) describes a wave with a period of ~20 min and horizontal wavelength of ~30 km propagating essentially parallel to the jet. This disturbance appears to owe its origin to a squall line in Ohio and Pennsylvania which later triggers heavy storms in the New York City area. Koch (1979), in a case study of an Oklahoma dryline, detects waves with wavelengths of 22 km and periods of 17 min. Using spectral methods on data from the National Severe Storm Laboratory mesonetwork, he concludes that these waves were responsible for triggering a series of 11 severe storms.

At longer wavelengths and periods, the papers by Bosart and Cussen (1973), Eom (1975), Uccellini (1975) and Miller and Sanders (1980) provide examples of midlatitude gravity waves which propagate over several hundreds of kilometers, persist from 6 to 15 h and are associated with storm and wind systems of various intensities. In the case of Bosart and Cussen, a wave of a few millibars amplitude, a 1–2 h period and a 50–90 km horizontal wavelength propagates in the direction of motion of the front. The origin of the wave is attributed to thunderstorms upstream of the gravity wave activity. Longer horizontal wavelengths are present in the events of 19 April 1970, discussed by Eom (1975), and of 18 May 1971, discussed by Uccellini (1975). These two cases are characterized by a very similar synoptic environment in which a stationary frontal zone extends northeast from a developing cyclone in the Midwest. In both cases, the waves propagate in the direction of a strong upper-tropospheric jet, cover a narrow path ~200 km wide, have amplitudes of a few millibars, horizontal wavelengths

[1] Current affiliation: Air Force Global Weather Central, Offutt AFB, NE 68113.

of 400–500 km and periods from 2.5 to 4 h. The static stability in the two cases, on the other hand, is very different. During the observation period of Eom's case the air over the Midwest is overcast and relatively stable. The main effect of the waves on the cloudiness is to introduce periodic variations in its intensity, but no convective activity is observed to be closely associated with the waves. In Uccellini's case, however, severe convective storm systems are present and their intensities fluctuate with periods of the same order as those of the gravity waves. Furthermore, the gravity waves appear to initiate convection in some areas and reintensify pre-existing storm cells in others. An exceptionally strong cyclogenetic environment characterizes the 3 April 1974 event described by Miller and Sanders (1980). Wave packets with periods of ~3 h and wavelengths approaching 275 km appear to play an important role in the reorganization or enhancement of existing thunderstorm cells and the initiation of new cells which eventually produce numerous tornados.

As has been previously noted by Uccellini (1975), the existence of strong jet streaks[2] and a developing cyclone are common features in these cases. While convection is also important, the Eom case study shows that the presence of convection is not a necessary requirement for the development of the large-amplitude, long-period gravity waves. Thus, while the generation of high-frequency gravity waves may at times be due to the cold outflow from severe storms during their dissipation, other mechanisms may be important for the development of subsynoptic to mesoscale waves. The strong vertical shears in jets suggest shear instability could be one such mechanism. The presence of jet streaks may also be significant in affecting the energy exchange between the background system and the waves and in forcing the selection of particular wavelengths.

The purpose of this paper is to present a detailed study of a gravity wave event which occurred on 9 May 1979, a case for which weather events such as storm movements and precipitation patterns correlate well with the observed waves. Here and throughout the paper we use the term "gravity wave" as synonymous with "gravity wave train" i.e., to indicate a progressive wave disturbance which is confined to a limited region of space at any instant of time. The case study is presented not only to document further the existence of large-amplitude, long-period and long-wavelength gravity waves, but also to determine possible mechanisms for wave generation.

The synoptic situation, which is quite similar to the Eom and Uccellini cases, is described in Section 2. The characteristics of the waves and the methods for their identification are presented in Section 3. The relation between waves and weather follows in Section 4, while the theoretical model for the waves is described in Section 5.

2. Synoptic overview: 9–10 May 1979

On 9–10 May 1979, an inverted trough extending northeastward from a surface low near the Texas Panhandle dominated the synoptic surface analyses (Fig. 1A). By 0000 GMT 9 May, a strong cold front had pushed into the central United States with temperatures plunging to near 0°C in the Dakotas. In Kansas, Nebraska and Iowa, temperatures were near 10°C just north of the front and jumped to 25°C immediately south of it. At 300 mb (Fig. 1B), the trough axis was located over eastern Nevada, with southwesterly winds extending across the central United States. An upper-level jet with winds greater than 60 m s^{-1} at the 300 mb level was located behind and parallel to the surface front. By 1200 GMT 9 May, the surface front became stationary from southwest Kansas to southern Wisconsin (Fig. 1C) with the temperature gradient across the front remaining near 15°C over ~300 km. The 300 mb analysis (Fig. 1D) indicates that the strongest upper-tropospheric winds were still located to the west of the front, with a jet streak centered over northern New Mexico and southern Colorado. The wind direction near the jet streak became more southerly with the trough beginning to close off near western Utah. By 0000 GMT 10 May, the surface front remained stationary in the northern Midwest (Fig. 1E) with an inverted trough evident in Iowa. The 300 mb analysis indicates that the trough axis had shifted only slightly eastward and was located over southwest Utah (Fig. 1F). The jet winds extended from New Mexico toward North Dakota, remained nearly parallel to the surface front and evolved into two separate jet streaks with winds greater than 50 m s^{-1}.

The radar summaries from 0435 to 1435 GMT 9 May 1979 (Fig. 2) indicate that considerable precipitation occurred in Nebraska, South Dakota, Iowa and Minnesota. Numerous thunderstorm systems were embedded within broad areas of rain, snow and ice pellets, with particularly intense convective cells attaining heights of over 50 000 ft in Nebraska and Iowa after 0535 GMT 9 May. These storms developed immediately to the west and north of the stationary front (Fig. 1C) within an air mass marked by surface temperatures of 2–6°C and immediately to the right of the jet streak axis analyzed at the 300 mb level (Fig. 1D).

While the radar summaries clearly depict intense convection for this case, there is little evidence for any periodic structure to the storm systems. Yet the infrared satellite imagery for this period illustrates that the convective systems in Nebraska, South Dakota, Iowa and Minnesota evolved in such a way as to produce an

[2] Palmén and Newton (1969, p. 199) define jet streaks as the regions of isotach maxima embedded within jet streams.

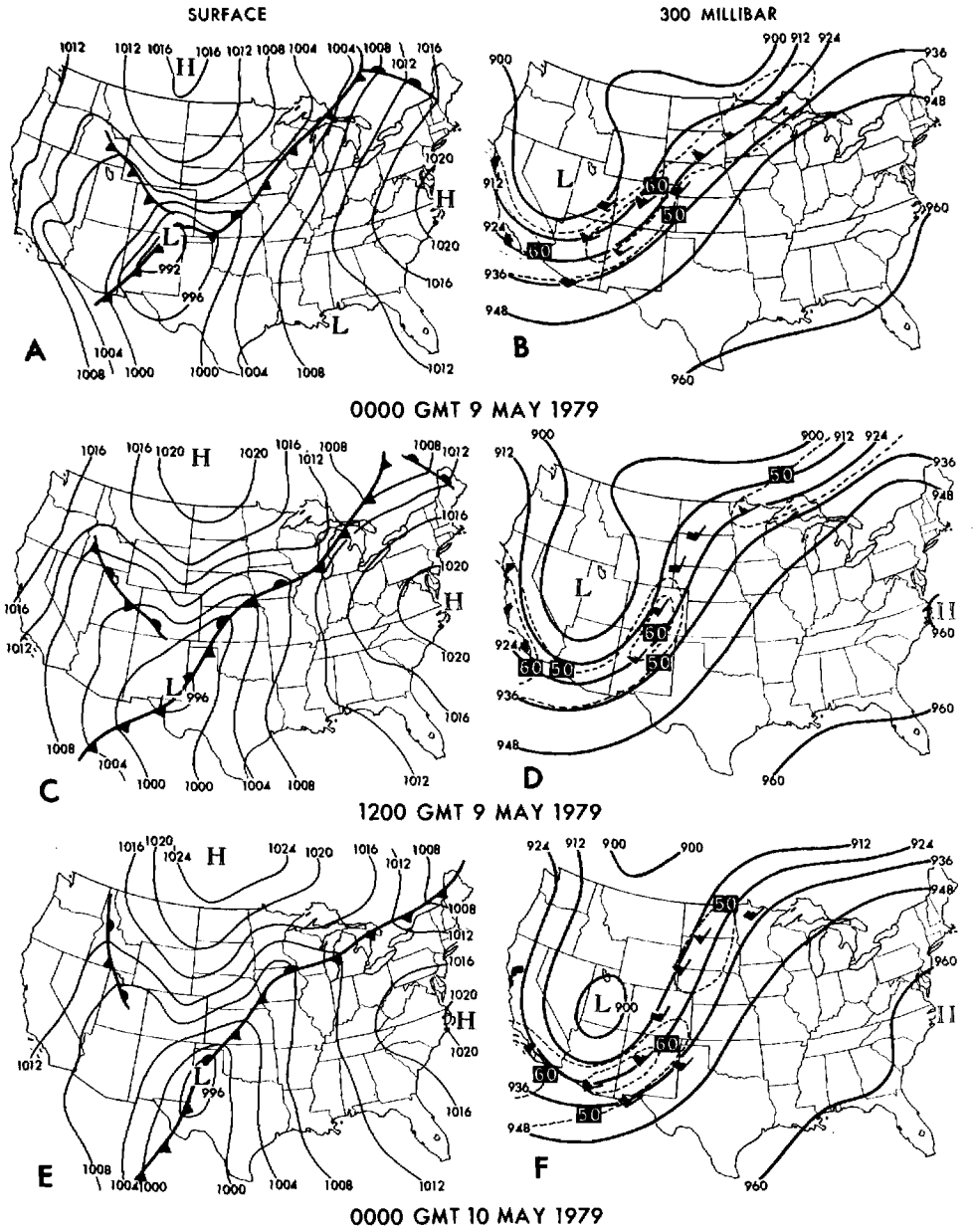

FIG. 1. Surface and 300 mb analyses for 0000 GMT and 1200 GMT, 9 May 1979 and 0000 GMT 10 May 1979.

interesting wave-like signature (Fig. 3). The initial development of individual convective systems occurred in Nebraska around 0400 (all times GMT) and propagated northeastward to southwest Minnesota by 0830 (refer to system B1 in Fig. 3). This convective system had individual cells with tops from 48 000 to 50 000 ft (Fig. 2D). A second convective system (system A2 in Fig. 3) developed in southwest Nebraska by 0545 and propagated northeastward to South Dakota, such that by 0830 a 300–400 km separation distance existed between convective systems B1 and A2. From this point on, convective systems propagated in a more easterly direction, remained to the north of the surface front and maintained a 300–400 km separation until 1330 when they appeared to begin merging. As systems B1 and A2 moved eastward, another weak band of convection developed in southwest Nebraska at 0730 and propagated rapidly into South Dakota by 1030 and is referred to as system A3 in Fig. 3. The convective system A3 was indicated by radar as a 23 000 ft cell imbedded within an area of snow and ice pellets (Fig. 2G and 2H). After 1030, A3 propagated more toward the east, remaining nearly 300–400 km behind system A2 until 1330.

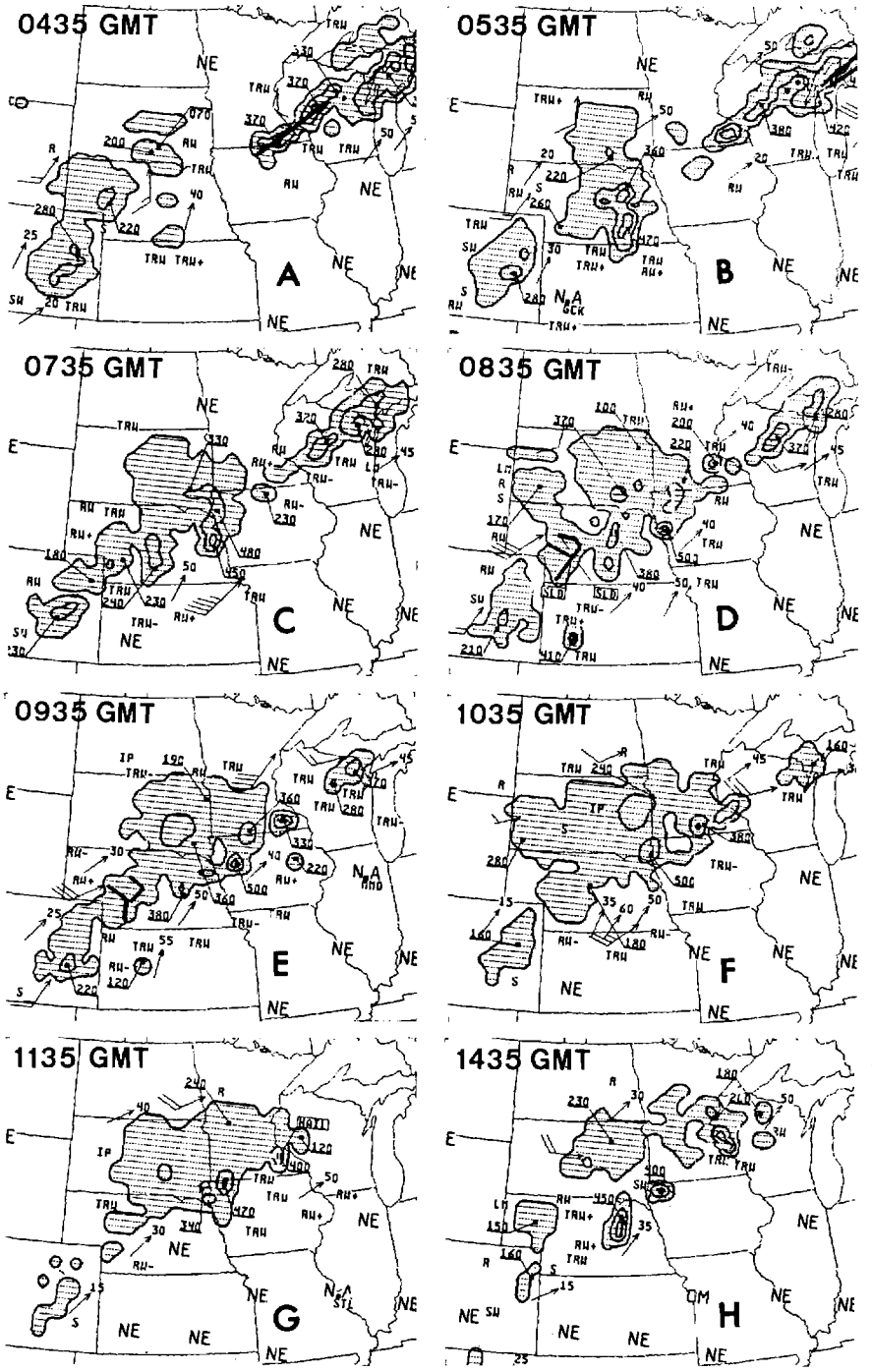

FIG. 2. Radar summaries from 0435 GMT to 1435 GMT, 9 May 1979 (0635, 1235 and 1335 GMT charts were not available).

The satellite imagery reveals that, although the convective systems underwent various stages of development and initially propagated toward the northeast, by 1130 a well-defined train of convective systems extended from South Dakota toward northwest Wisconsin. The systems propagated east–northeast at 25 m s^{-1} from the Dakotas toward Wisconsin and maintained a separation distance of 300–400 km.

Another storm (C1 in Fig. 3) developed in central Nebraska and is depicted both in the radar and satellite images of 0830 GMT. This system propagated north–northeast and by 1035 had developed to a height of

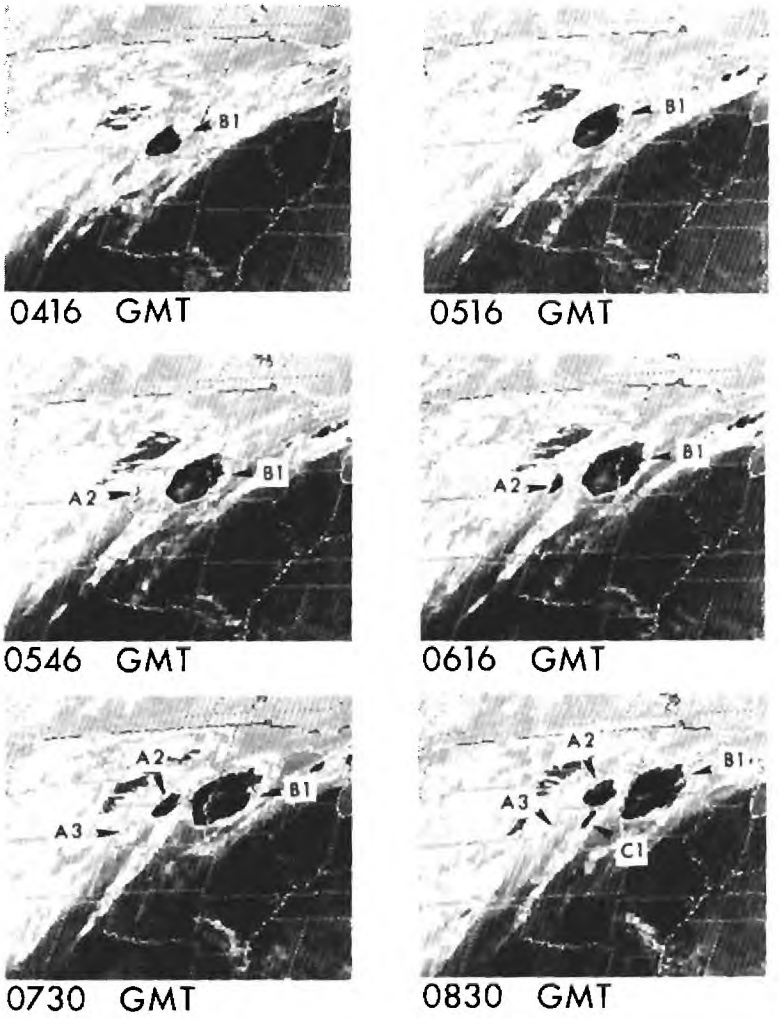

FIG. 3. Enhanced infrared GOES satellite pictures from 0416 GMT to 1430 GMT, 9 May 1979.

50 000 ft. Another interesting storm system (D in Fig. 3) developed over east-central Nebraska at 1330. This storm system, along with a rapidly developing new cell in northwest Iowa (E in Fig. 3), was clearly depicted on the 1430 infrared imagery. These storms grew to 45 000 and 40 000 ft, respectively (Fig. 2H) and were spaced at nearly the same 300 km interval as the earlier storms (B1, A2 and A3). They propagated northeastward at nearly 20 m s^{-1}, remaining northwest of the stationary front (Fig. 1C).

In summary, the most striking features from the surface, 300 mb and radar charts and satellite infrared imagery are as follows:

1) The existence of a stationary front and inverted trough over the United States for nearly 24 h with upper-tropospheric jet streaks nearly parallel to the front, located to the west and north of the surface frontal zone. The entire synoptic pattern is remarkably similar to that in the Uccellini (1975) case study.

2) The wave-like characteristics of the thunderstorm complexes as revealed by the satellite imagery. The storm systems maintained a 300–400 km separation distance after 0730 GMT as the convective activity propagated north–northeast at 25 m s^{-1}.

3) The location of the convective cells relative to the upper-tropospheric jets and surface front. The convective storms developed in regions of strong anticyclonic shear and remained west and north of the stationary front where surface temperatures remained below 6°C.

In the following section, detailed analyses of the surface pressure fields are presented to determine if the characteristics and behavior of the thunderstorm complexes can be related to gravity wave concepts.

3. Wave detection

To determine if the "wavelike" characteristics of the thunderstorm complexes are indeed linked to grav-

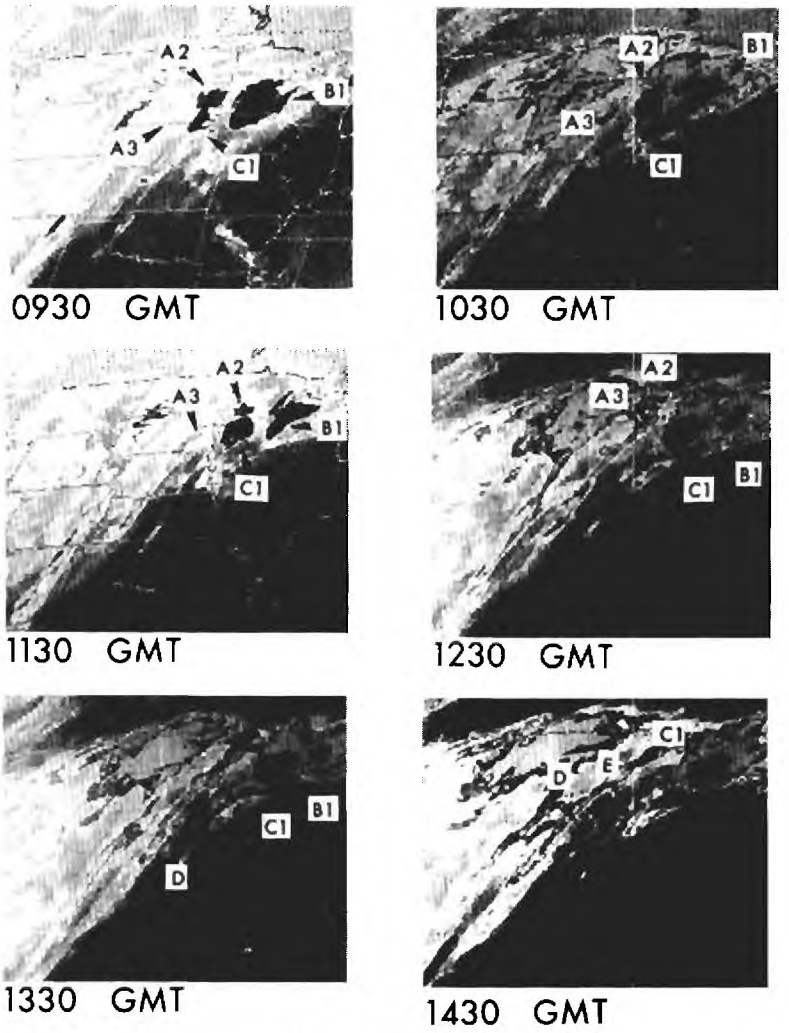

FIG. 3. (*Continued*)

ity wave concepts, a detailed analysis of the surface pressure traces was undertaken for the region in the northern Midwest just north of the Severe Environmental Storms And Mesoscale Experiment (SESAME) regional-scale domain (Fig. 4A). To isolate the waves for this case, pressure traces from 30 stations in the North Central States were analyzed (Fig. 4D). The analysis proceeded as follows.

a. Digitizing

Two types of pressure traces, 4 days per page (Fig. 5A) and 12 hours per page (Fig. 5B) were obtained from the National Climatic Center. Because of the condensed time scale, the 4 days per page traces were digitized at only 6 samples per hour. The 12 hours per page traces were sampled at a rate of 12 samples per hour. Higher sampling rates did not appear necessary. On the other hand, significant aliasing occurred at much lower sampling rates such as 1 sample per hour, indicating that hourly surface data are not sufficient to resolve these waves properly.

b. Filtering and visual cross-correlation

Before filtering the data, the mean and trend were removed using a least-square fit. The data were then filtered by convolving them with a 145 point hamming bandpass filter using a program written by Rabiner *et al.* (1979). After careful consideration of the power spectra (see next section) and visual inspection of the raw data, the band of the filter was selected to be between wave periods of 1.5 and 4.5 h.

The resulting pressure perturbation (p') traces are shown in Fig. 6. Notice the strong wave activity that emerges in the area from southern Nebraska to central Minnesota. This area corresponds with the regions of the intense convective storms (Figs. 2 and 3) and is located to the west of the surface front near the region of noted upper-level jet streaks (Fig. 1). These waves

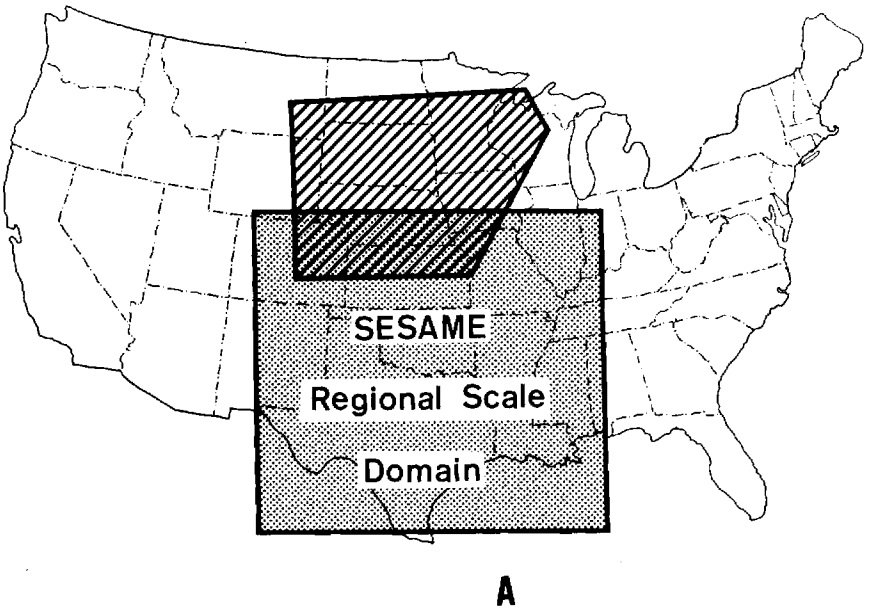

FIG. 4A. SESAME regional scale domain (shaded) and our area of interest (stippled).

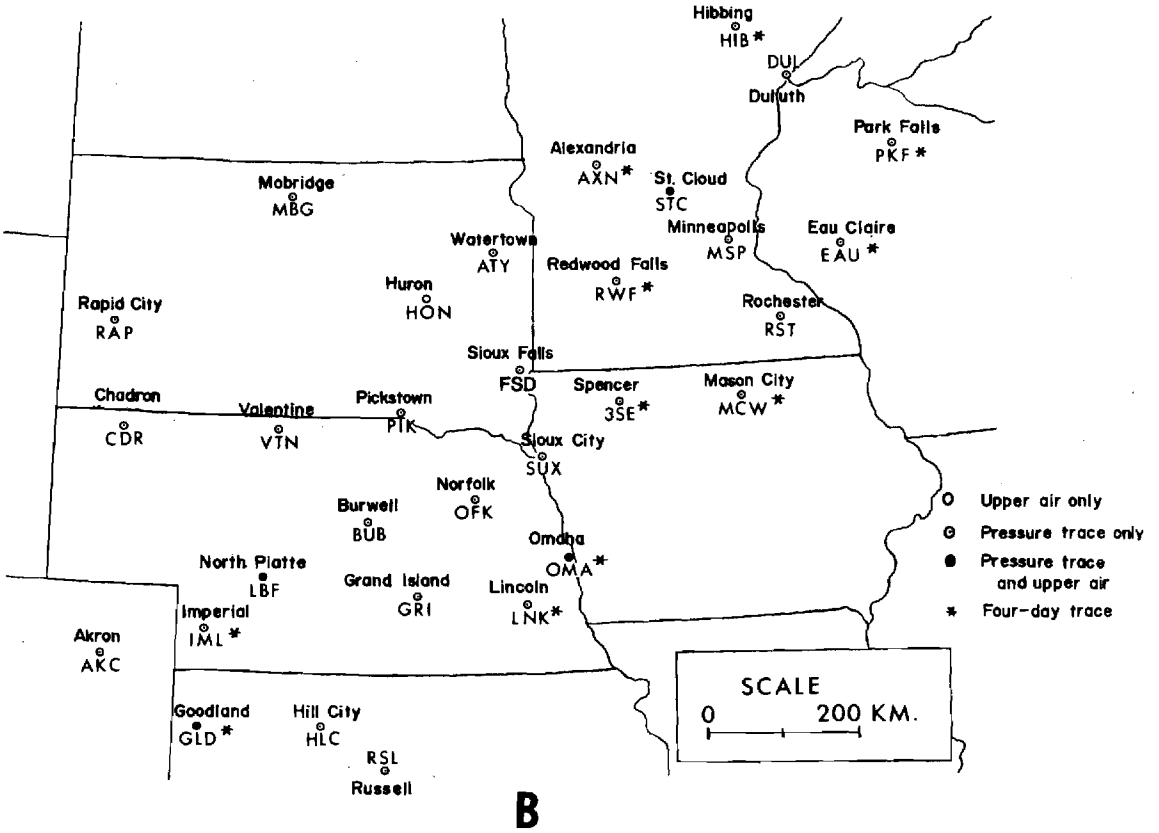

FIG. 4B. Stations for which data were analyzed. Stations having 4-day pressure traces are marked with an asterisk. All other stations have 12 h pressure traces.

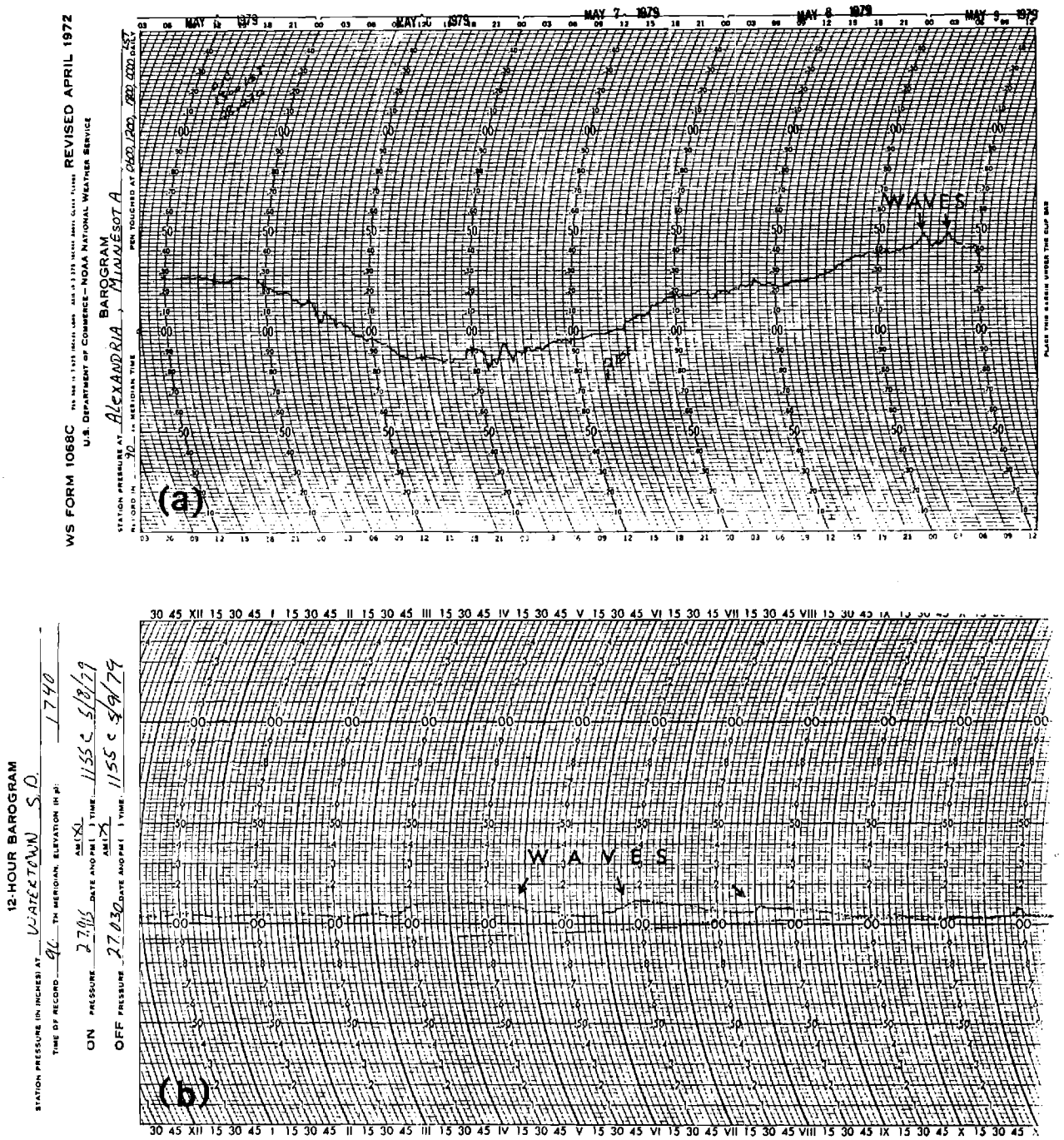

FIG. 5. Sample barograph traces: (a) 4-day/page trace, (b) 12 h/page trace. Probable gravity waves are labeled on each chart.

reach a peak amplitude of nearly 2 mb at Pickstown, South Dakota (PIK) and Sioux Falls, South Dakota (FSD). Minor oscillations such as those of Omaha, Nebraska (OMA) and Rapid City, South Dakota (RAP) are probably below the noise level of 0.2 mb.

Next, the filtered p' traces were examined to determine if any persistent patterns existed between individual stations. We found two tracks along which a coherent wave pattern could be clearly identified. The location of these two tracks is given in Fig. 7, with track A extending from southwest Nebraska to central Minnesota and track B from southern Nebraska to northwest Iowa. The p' traces for track A are shown in Fig. 8 and for track B in Fig. 9. The p' traces have

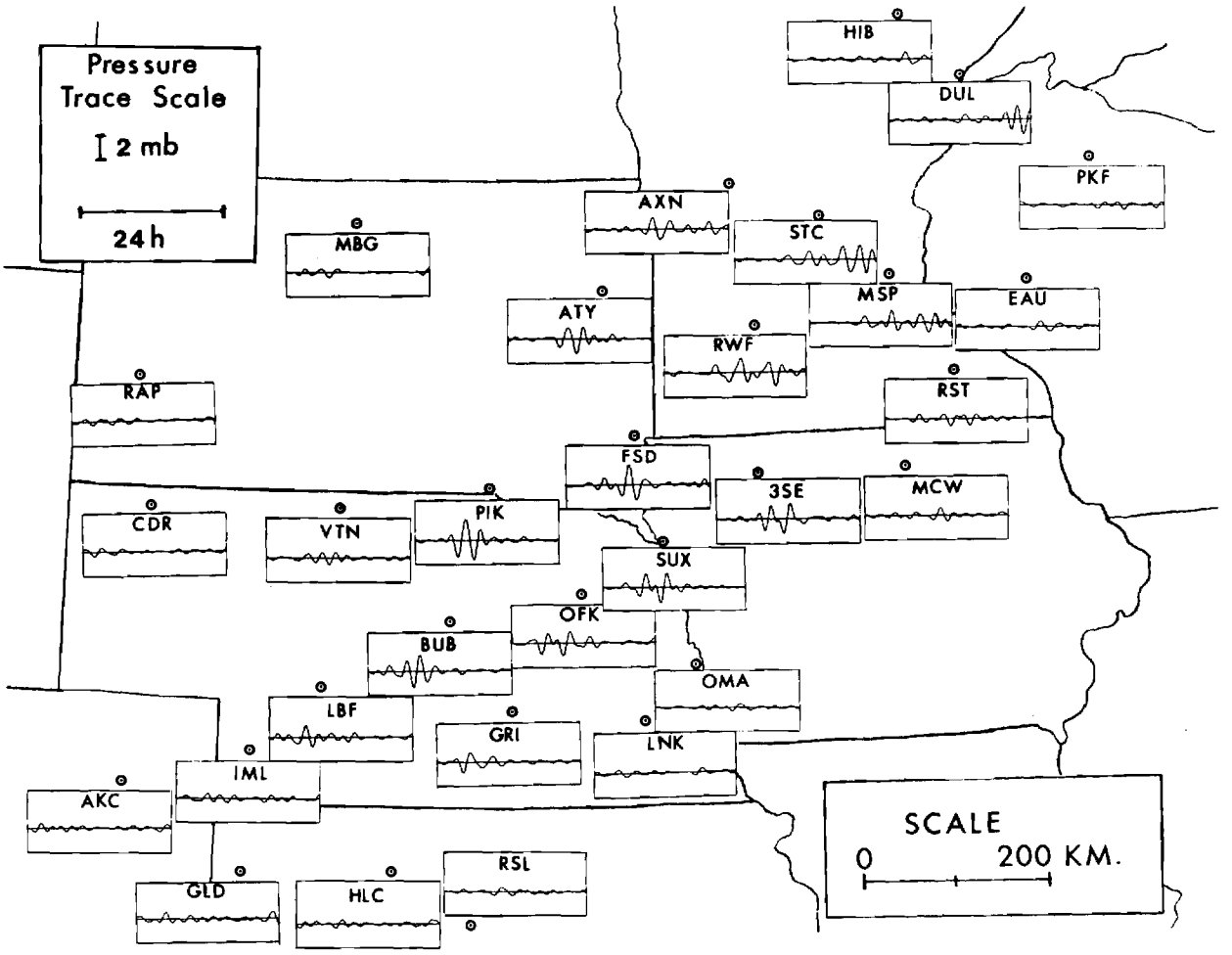

FIG. 6. Pressure traces filtered using a pass band of 1.5–4.5 h.

been shifted in time to line up corresponding pressure ridges and troughs.[3] The progression of these time shifts is a measure of the phase velocity which approaches 30 m s^{-1} along track A and 20 m s^{-1} along track B. The waves maintained a remarkable coherence over a long distance, especially along track A (Fig. 8) indicating that the wave duration approached 10 h. The wave along track A appeared at Imperial, Nebraska (IML) near 0500 with p' values of nearly 0.5 mb. The wave amplitude rapidly amplified at North Platte, Nebraska (LBF) between 0500 and 0600 (Fig. 8), with p' values approaching 1.0 mb. The wave amplitude continued to grow along track A, amplifying to 1.5 mb at Pickstown, South Dakota (PIK), with p' greater than 1 mb along the remainder of the track. It therefore appears that the wave along track A developed near southwest Nebraska and propagated at 30 m s^{-1}, maintaining a period of ~2.5 h.

The wave along track B (Fig. 9) appeared first as a distinct p' trough at Grand Island, Nebraska (GRI) at 0400. The wave then propagated northeastward at 20 m s^{-1} and remained quite coherent along track B with a period of 3.3 h.

In contrast to the apparently good correlation *within each track,* the correlation *between the two tracks* appears poor, as indicated in Fig. 10, where PIK and Norfolk, Nebraska (OFK) have been visually correlated. The correlation appears to be nonexistent between these two stations, even though PIK and OFK are only 150 km apart and both have active wave patterns. The good correlation along each track and poor correlation across the tracks reflect a tendency for the waves to propagate northeastward in this area,

[3] The times on the Burwell (BUB) trace are approximate since the original traces were each 12 h long, but plotted on the 4-day chart with no time calibrations. Furthermore, there were only three surface observations from BUB on 9 May 1979, which were not sufficient to help identify any specific point on the trace.

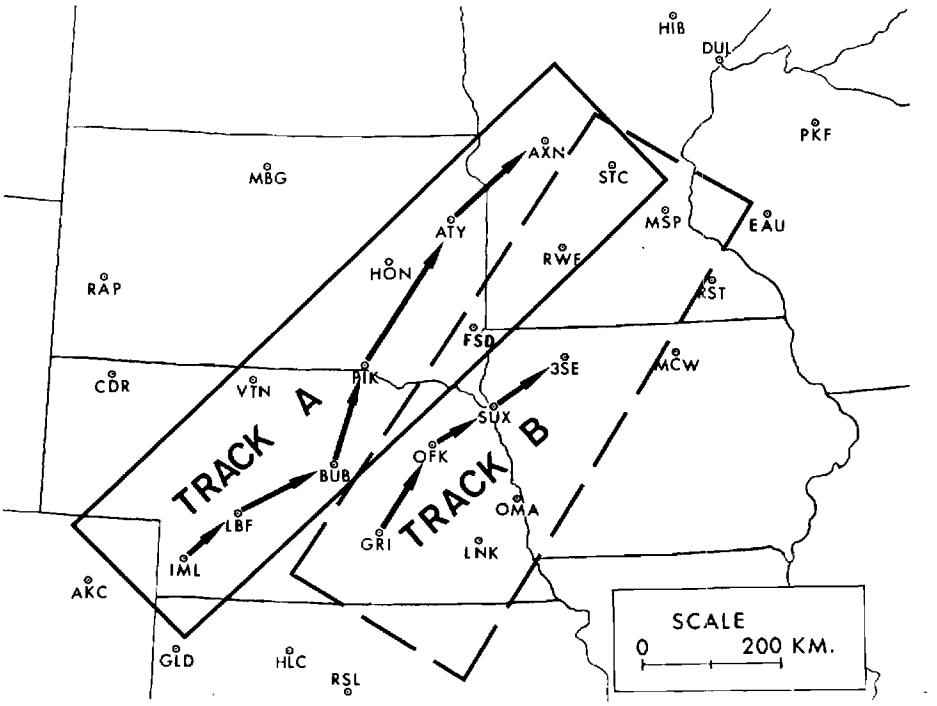

FIG. 7. Tracks over which coherent waves appeared to propagate. Boxes enclose stations used in phase velocity calculations.

a direction which parallels the upper tropospheric flow field as analyzed at the 300 mb level (Fig. 1).

c. *Power spectra*

The power spectra for each of the 30 stations were calculated using two techniques, the weighted autocovariance (Rabiner *et al.*, 1979) and the maximum entropy method (Robinson and Silvia, 1981). Prior to calculating the power spectra, each trace was conditioned by removing the mean and applying a 241-point high-pass hamming filter. The high-pass filter passed all waves with periods < 8 h. Because the waves appeared for only 2–3 cycles at each station, significant side lobes persisted in the autocovariance spectra. This is why the maximum entropy method, a technique specifically designed to analyze short-lived signals, was also employed.

The 95% confidence limits for the autocovariance spectra are approximately −5.2 to 13.2 dB with an equivalent bandwidth of 0.3 cycles h^{-1}. This is based on the formula described in Jenkins and Watts (1968) involving the ratio N/M, where N, the number of sample points, and M, the maximum lag, are both equal to 96 in our case and the data have been tapered with a hamming window. These confidence limits do not necessarily apply to the maximum entropy spectra.

The spectra for the stations along and adjacent to each track (enclosed by the rectangular boxes in Fig. 7, henceforth referred to as areas A and B) were used to identify the dominant wave periods. The dominant frequency for each station along track A falls between 0.32 and 0.40 cycles h^{-1} (2.5–3.1 h period), as evident from Fig. 11. The spectra for Valentine, Nebraska (VTN) and FSD (not shown) also have periods of 2.5 h and cross-correlate well with each other and with the stations along track A. The two remaining stations along track A [Redwood Falls (RWF) and St. Cloud (STC), Minnesota] do not correlate well and their power spectra appear dominated by longer periods of 4.5 and 5 h. Because most of the stations in area A exhibit a dominant period of 2.5 h, this value will be used in all of the track A wave calculations in Section 5.

Along track B, GRI, OFK and Spencer, Iowa (3SE) have spectral peaks near 0.3 cycles h^{-1} (3.3 h period) while Sioux City, Iowa (SUX) has a peak between 0.20 and 0.28 cycles h^{-1} (3.6–5 h periods). See Fig. 12. These four stations suggest a dominant period near 3.3 h. Off the main track, but within area B, Lincoln, Nebraska (LNK) and OMA do not exhibit waves above the 0.2 mb noise level and thus are not considered. The four remaining stations in area B [FSD, RWF, STC and Minneapolis, Minnesota (MSP)] exhibit waves with amplitudes above the noise level but with differing periods. Because of the lack of coherence at

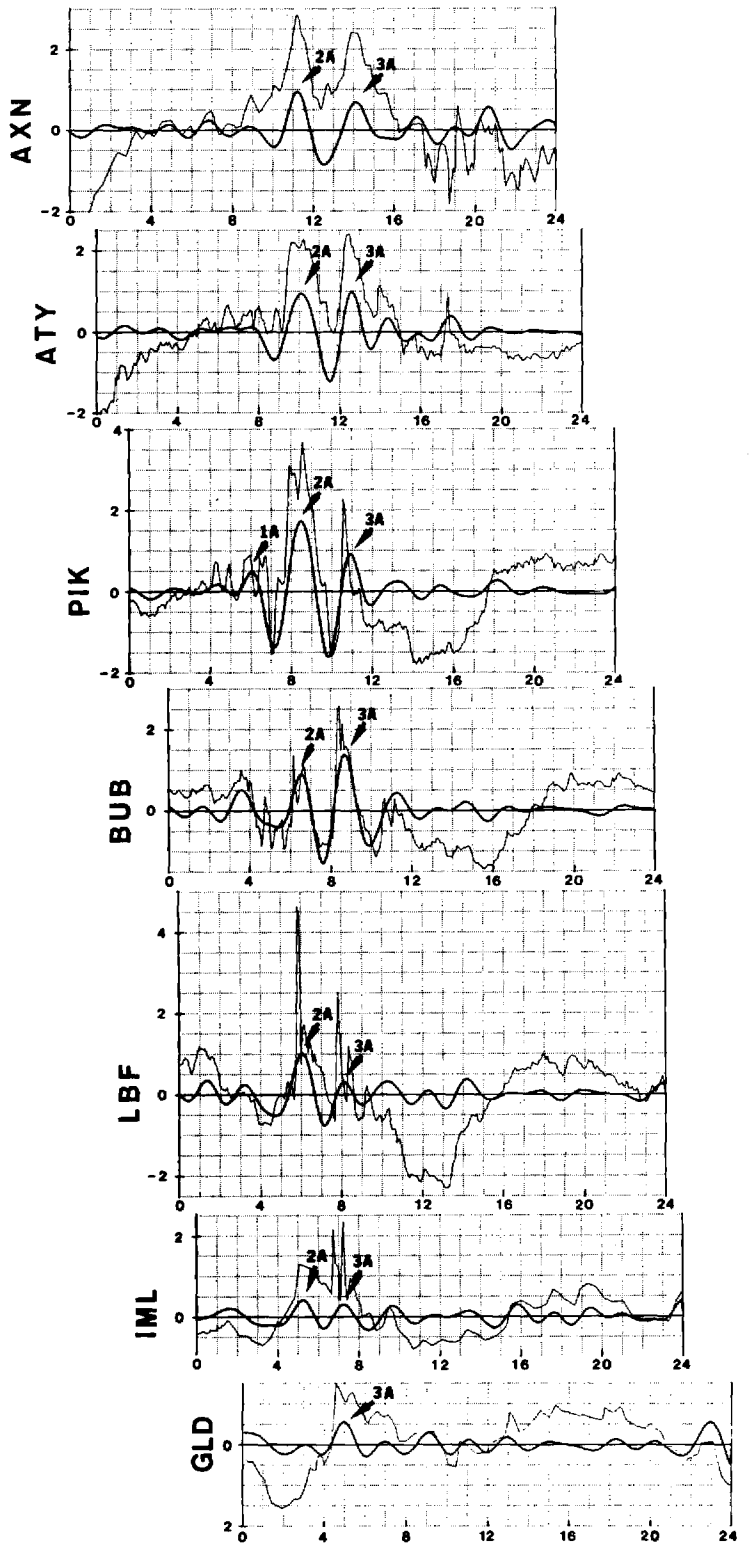

FIG. 8. Pressure traces from stations along track A. For each station the ordinate is pressure (mb) while the abscissa is time (GMT). Dark traces are the bandpass filtered traces while the thin traces are the raw data with the mean and trend removed. The labels A1, A2 and A3 identify the three main pressure maxima that propagated along track A.

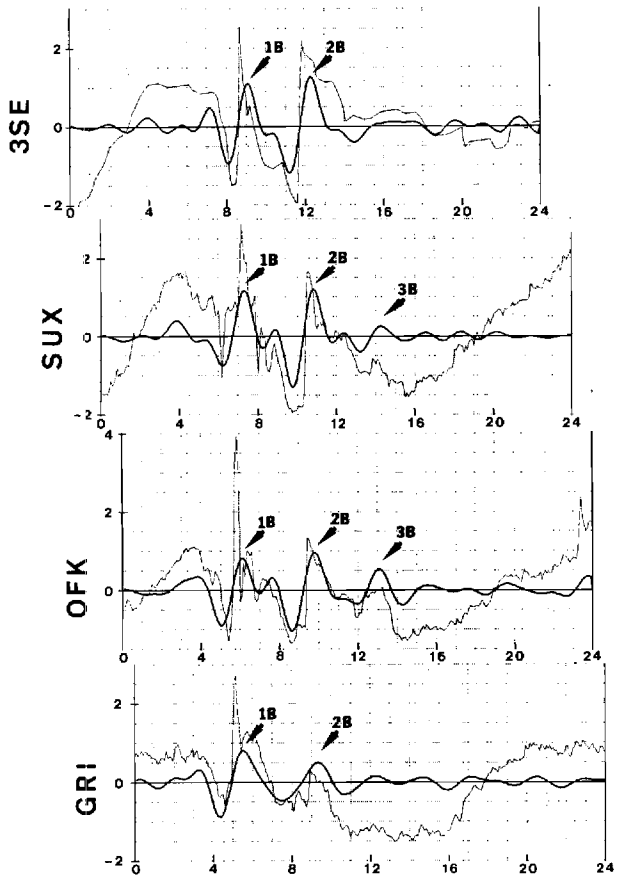

FIG. 9. Pressure traces for stations along track B. Same format as in Fig. 8.

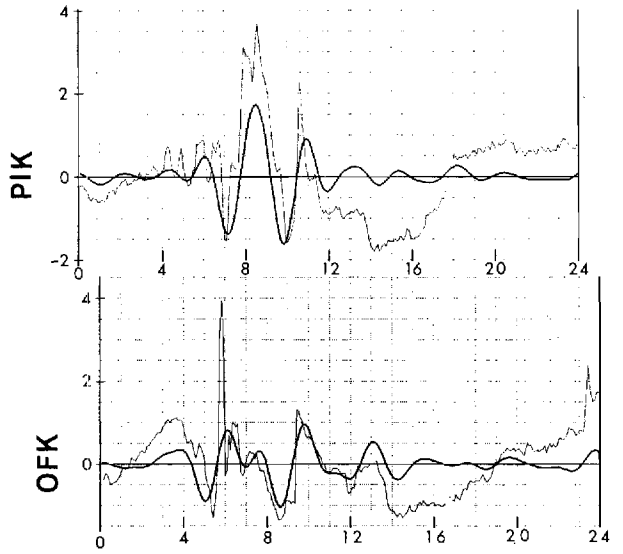

FIG. 10. Pressure traces for one station in track A (PIK) and one station in track B (OFK). Same format as in Fig. 8.

these stations, we used only the main track stations to estimate the dominant wave period of 3.3 h along track B.

d. *Cross-correlation functions*

As noted in Figs. 8 and 9, the stations along each track showed strong visual correlations. To verify these results mathematically, we calculated the cross-correlation functions for those stations that were geographically close and whose spectra revealed similar harmonic content.

The cross-correlation function between two pressure signals, p_i and p_j, is defined as

$$c(\tau) = [a_i(0)a_j(0)]^{-1/2} \int_{-\infty}^{\infty} p_i(t)p_j(t+\tau)dt,$$

where $a_i(0)$ and $a_j(0)$ are the corresponding autocovariances at zero time lag. From this expression, $c(\tau) = 0$ indicates no correlation and $c(\tau) = 1$ a perfect correlation. Fig. 13A shows a cross-correlation function for two uncorrelated stations. Fig. 13B and 13C show cross-correlation functions for two stations along tracks A and B, respectively. Some of the features to notice in these figures are as follows:

1) Fig. 13A appears to be nothing more than noise since nearly all of the 95% confidence bars will cross the zero correlation value. The 95% confidence limits were estimated using the formula $\pm 1.96/\sqrt{N}$, where N is the number of sample points (see Jenkins and Watts, 1968). To allow for the time lags between stations, a time interval of 16 h was sampled at a rate of 12 samples per hour, so that $N = 192$. Also there is little evidence of a fixed periodic structure.

2) A periodic structure does emerge for correlations along tracks A and B. A statistically significant correlation along track A (Fig. 13B) reveals a period of about 2.5 h. For track B (Fig. 13C), the correlation is again statistically significant with the 3.3 h period well represented.

3) The maximum correlations along tracks A and B both occur at a positive time lag. The position of the maximum correlations indicate the relative phase shifts between the station pairs. That is, a given pressure maximum (or minimum) occurred at Pickstown about 1.6 h before appearing at Watertown (Fig. 13B). A given pressure maximum (or minimum) occurred at Grand Island ~0.7 h before it occurred at Norfolk (Fig. 13C). One could argue that such cross correlations can reveal the angular phase shift to within only an integral multiple of 2π. This fact necessitates the use of other supporting evidence to firmly establish the above values.

Finally, if two stations are correlated from different tracks, the cross correlation is poor (Fig. 13D) but not

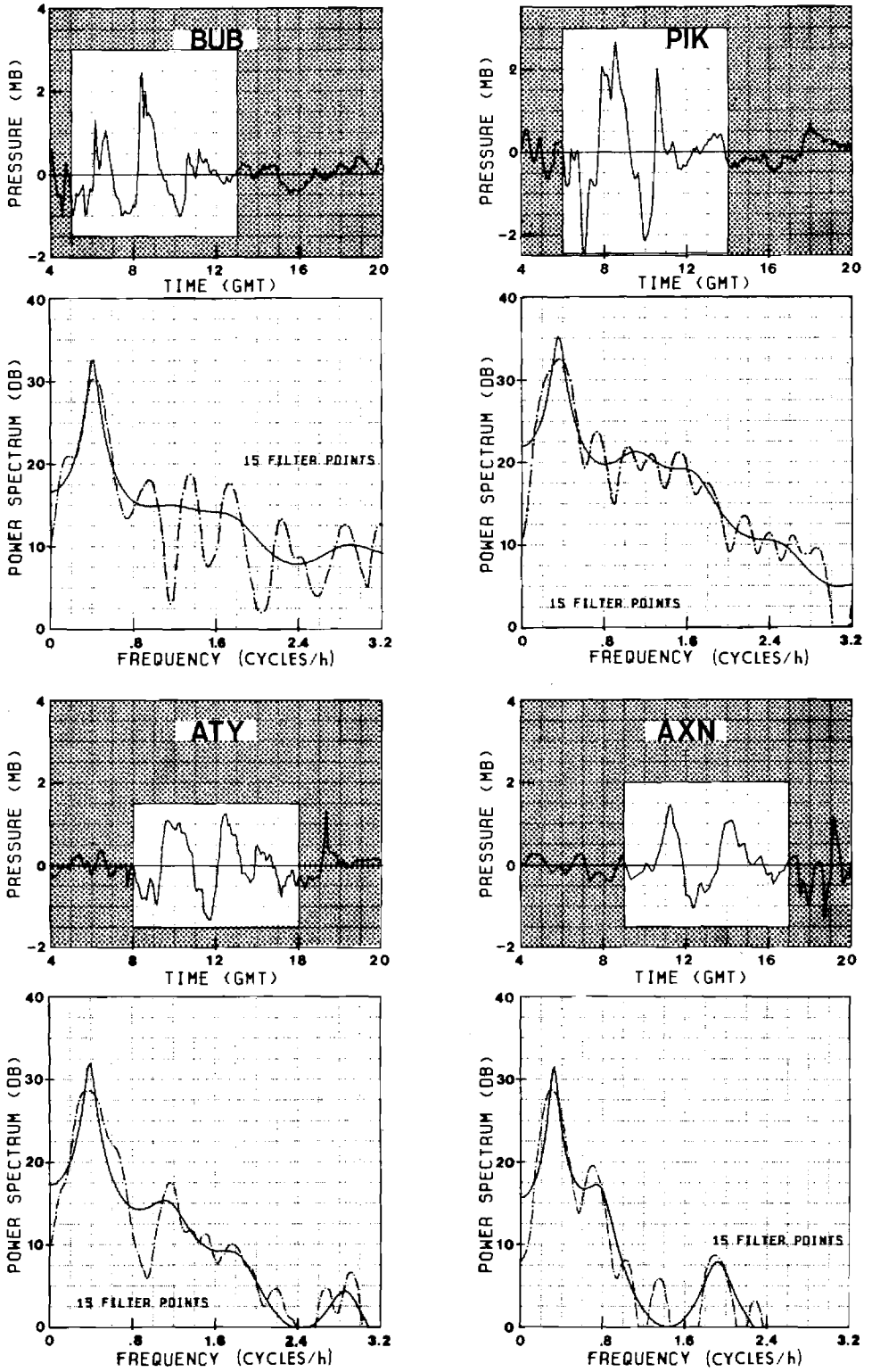

FIG. 11. High-pass filtered traces and power spectra for four stations along track A. Power spectra were calculated for the boxed-in area of each pressure trace. Each power spectrum appears immediately below its corresponding pressure trace. The solid spectral line is the maximum entropy method result while the dashed line is the autocovariance method result. Also listed are the number of filter points used to calculate each maximum entropy spectrum. The spectra are all plotted in the same arbitrary units.

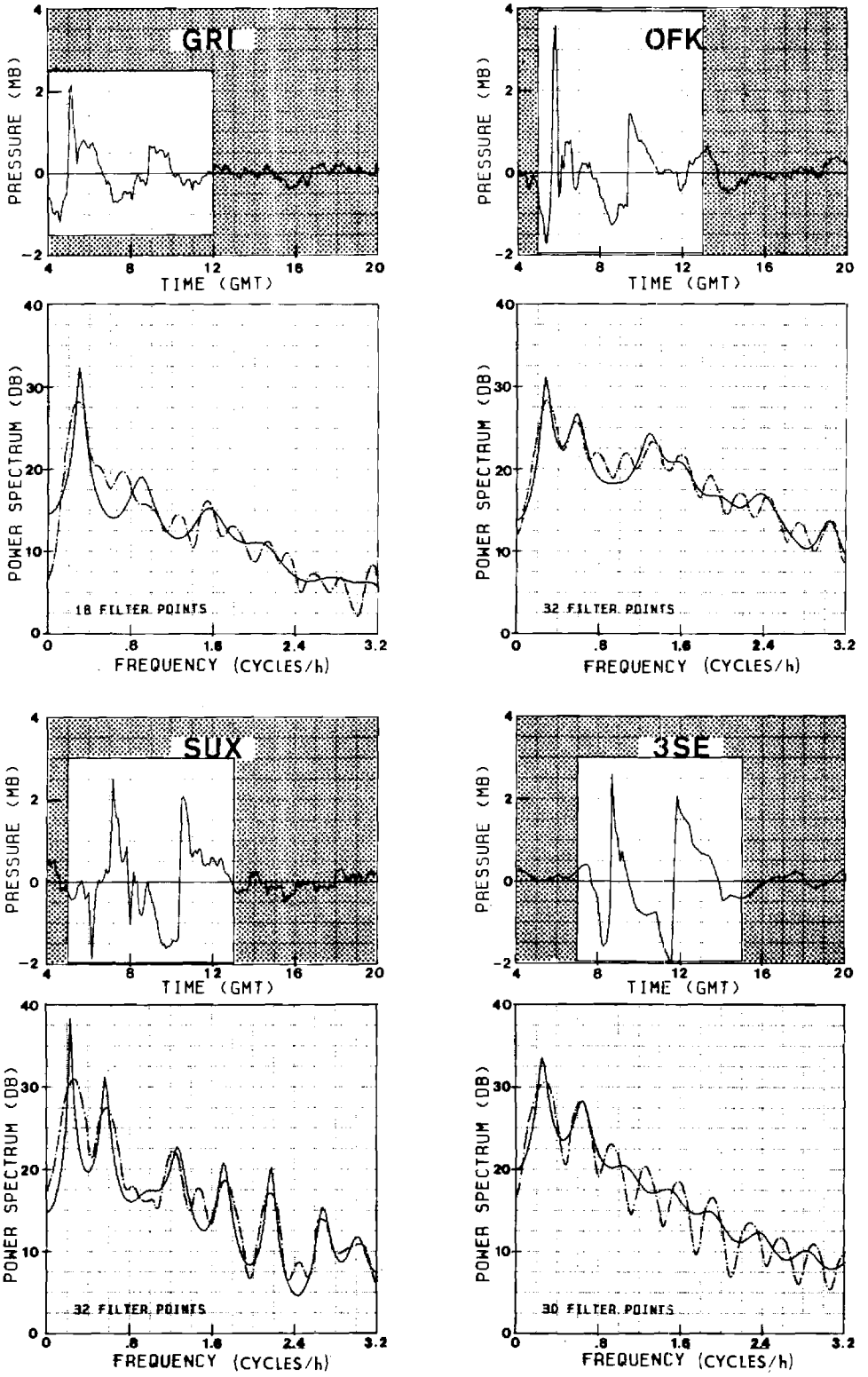

FIG. 12. High pass-filtered traces and power spectra for stations along track B. Same format as in Fig. 11.

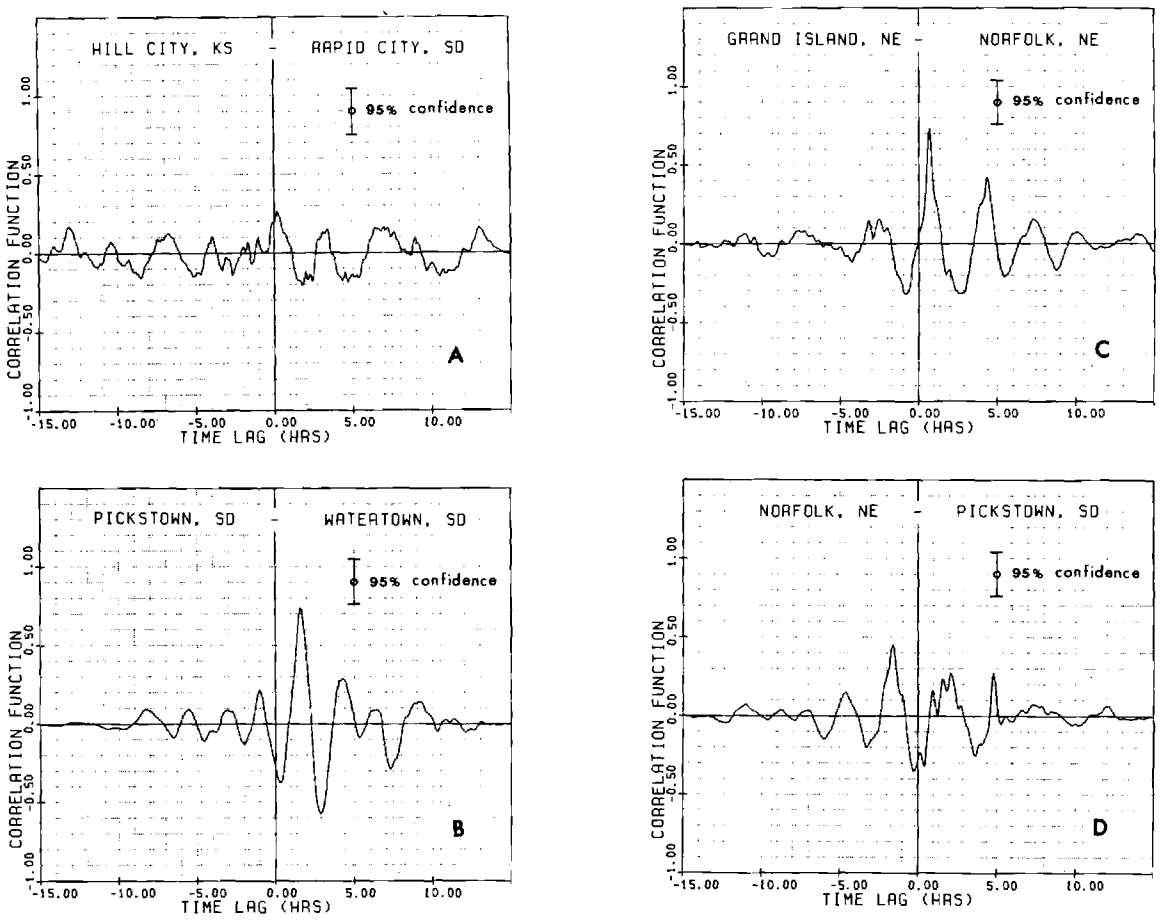

FIG. 13. Cross-correlation functions for: (A) two poorly correlated stations; (B) two stations along track A; (C) two stations along track B; (D) two stations, one for track A and one for track B.

as bad as two stations which do not belong to either track (Fig. 13A).

In summary, the cross-correlation functions between two well-correlated stations can provide two important measurements: the periods of the strongest common waves and the phase shifts between stations. Such phase shifts may result from a wave propagating in a direction **k**, with **k** the wave vector, or from the wave structure in the direction perpendicular to **k**, or both.

e. Phase velocity

A preliminary estimate of the phase velocity for each track was made by first examining the cross-correlation functions within each area (Fig. 7). These indicated that both waves traveled nearly parallel to the jet streak as analyzed at 1200 GMT 9 May 1979 (Fig. 1D) and exhibited a structure perpendicular to their direction.

To gain further insight into the phase velocity and structure of track A, the bandpass-filtered traces in area A were used to construct a time cross section along the heavy solid line in Fig. 14. Each station was projected on such a line along the direction perpendicular to the axis of the jet at 1200 GMT 9 May 1979. These projections are plotted on the vertical axis of Fig. 15, where the solid and dashed lines connect the pressure maxima and minima for the along-track stations and were drawn with the aid of the cross-correlation results. The slopes of these lines are nearly constant and correspond to a mean speed of 30 m s^{-1}. The stations off the main track were not used to construct these lines. As mentioned earlier, STC and RWF exhibit longer period waves and thus are not expected to fit the pattern of the remaining stations. On the other hand, FSD and VTN are $\sim 180°$ out of phase with the rest of the stations. We interpret this phase shift to be a manifestation of the waves transverse structure.

To illustrate this point, we consider a monochromatic wave propagating along the x-axis:

$$a(x, y, t) = a(y) \exp[i(\omega t - k_x x)] + \text{c.c.},$$

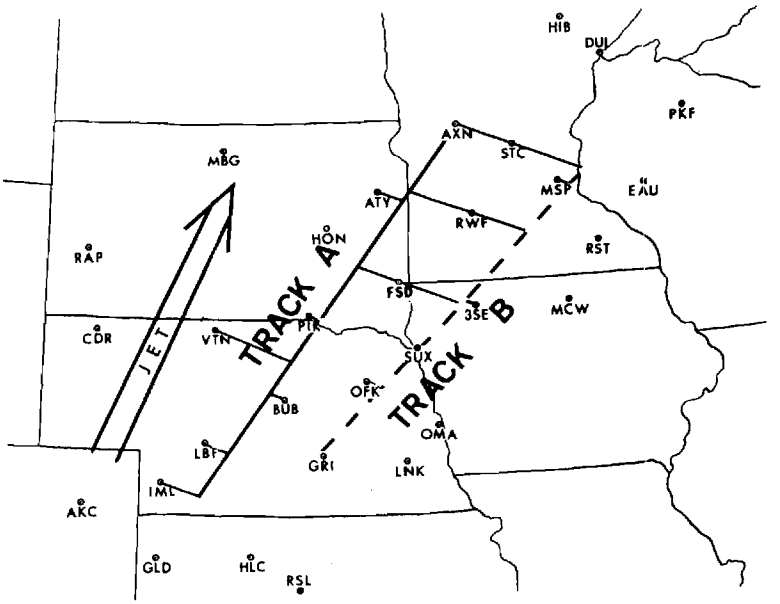

FIG. 14. Solid heavy line (mean position of track A in Fig. 7) is the track used for the time cross section in Fig. 15. The arrow marks the direction of the 1200 GMT 9 May 1979 jet. The thin solid lines are perpendicular to the jet direction and project the positions of the stations of area A onto the heavy solid line. The dashed line plays the same role for track B and is used for the time cross section in Fig. 16.

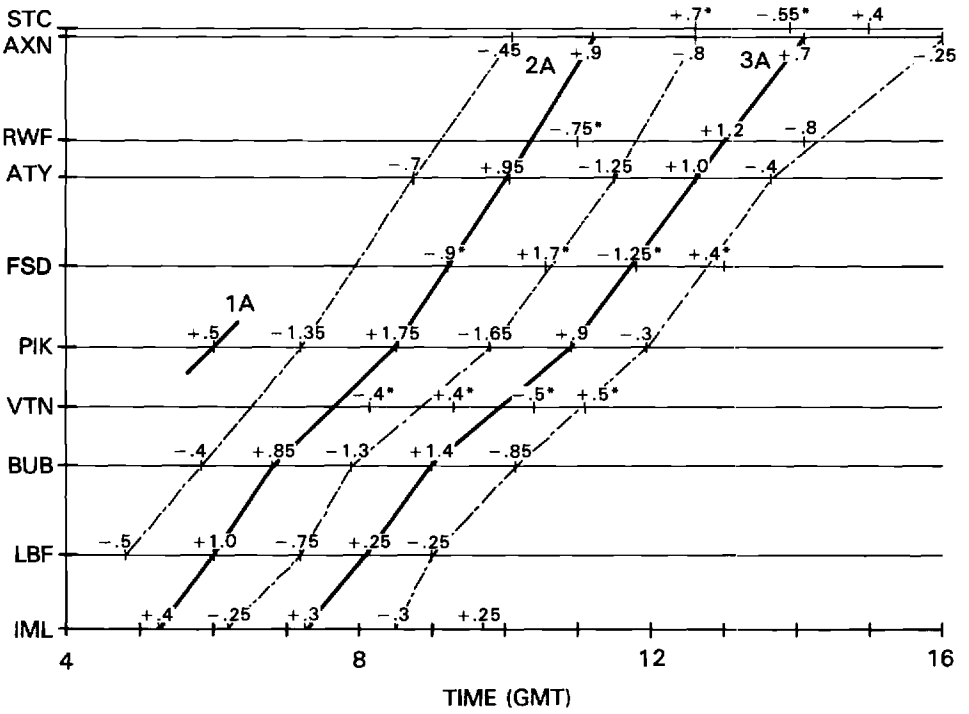

FIG. 15. Time cross section for track A. Plotted values are maxima and minima (mb) from the bandpass-filtered traces. The dark solid lines connect pressure maxima and the dashed lines connect minima. Maxima are also identified as 1A, 2A and 3A. Values marked with an asterisk appear to be out of phase and were thus not used to construct the lines.

where k_x is the wavenumber, ω the pulsation, and c.c. represents the complex conjugate. If $a(y)$ is constant, then any phase shift between stations will depend on the phase factor $(\omega t - k_x x)$. If, on the other hand, $a(y)$ is dependent on y, then such a dependence alone can produce a phase shift between two points. For instance, if $a(y) = \cos k_y y$, then two points at the same x but π/k_y apart will always be 180° out of phase. This point is further discussed in Section 5.

The transverse structure introduces another problem in the computation of the phase velocity. Typically, one uses standard cross-correlation techniques to calculate the phase velocity of a monochromatic wave without a transverse structure. The phase velocity $\mathbf{v}_{ph}$ is calculated so that the equations relating the time lags to $\mathbf{v}_{ph}$ are satisfied in a mean square sense. This approach must be modified for waves with a transverse structure. The simplest way to compensate for the structure is to adjust by 180° the phase shifts between the track and both VTN and FSD. After this adjustment, the standard technique produces an average phase velocity of 29.4 ± 6.8 m s^{-1} at 217° ± 31.8° and a wavelength of 265 km. This agrees well with the preliminary estimates. The results indicate that the wave along track A propagated parallel to the jet streaks analyzed at the 300 mb level (Fig. 1) with a phase velocity below the jet maximum.

Analogous reasoning was applied to the wave along track B. As evident from Fig. 16, the track B wave was not as coherent as the wave along track A. The variability of the slope is an indication of the variability of the phase speed. Stations OFK and SUX exhibit three distinct pressure peaks while the other stations have only two. Station FSD is 180° out of phase with respect to the main track, again indicating a possible transverse structure. The p' traces for STC and RWF, which display longer periods, also fit poorly. The stations that fit best are OFK, SUX, FSD (after a 180° phase shift), 3SE and MSP. Using these stations and a dominant period of 3.3 h, an average phase velocity of 20 ± 2 m s^{-1} at 215° ± 12° was determined. Once again, the direction is nearly parallel to the upper-level flow with a phase velocity well below the wind speeds measured at the jet level.

f. Characteristics of the medium in which the waves propagate

Both waves propagate along the jet direction as characterized by the 1200 GMT 9 May, 300 mb analysis (Fig. 1D). This is also apparent in the 1400 GMT North Platte, Nebraska sounding obtained from the SESAME network (the 1200 GMT sounding was incomplete) which is plotted in Figs. 17 and 18. The atmosphere appears to be statically stable, with rather strong vertical shears resulting in low values of the Richardson number Ri. These values are an indication that the atmosphere may be dynamically unstable. Generally low Richardson numbers are also present at other stations along the track. Information about

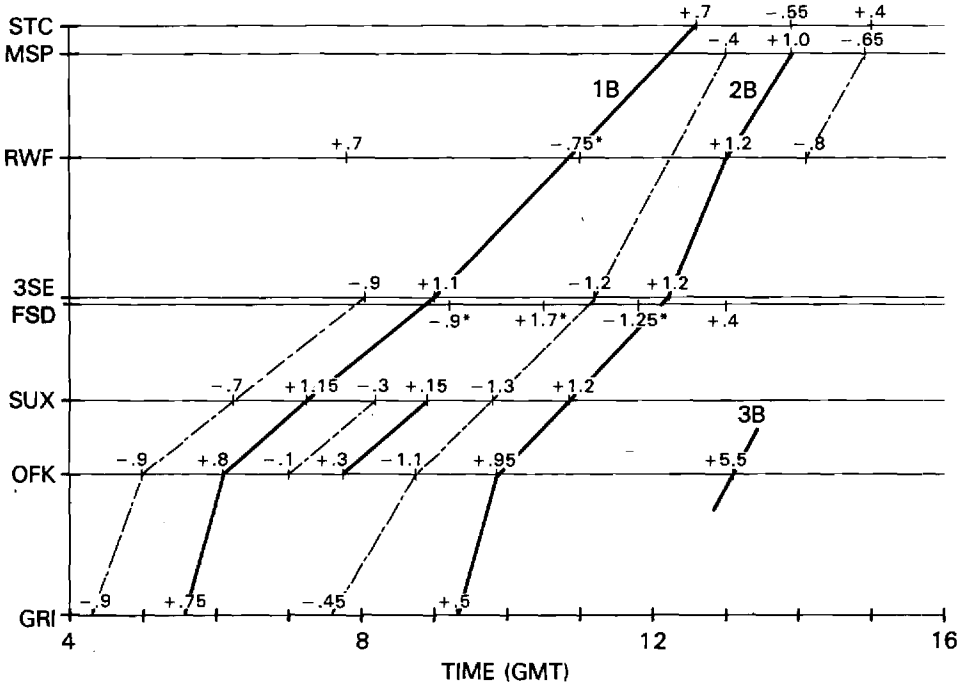

FIG. 16. Time cross section for track B. Same format as in Fig. 15.

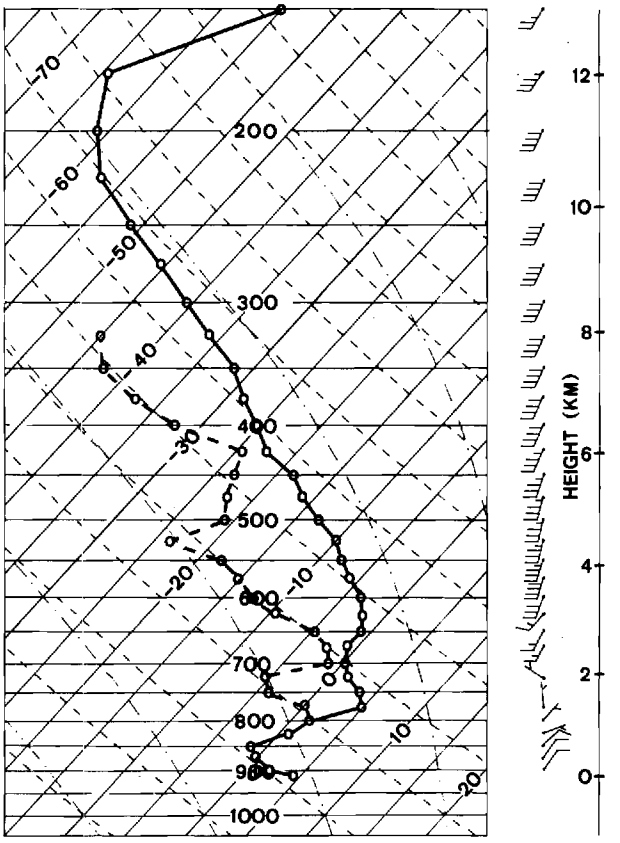

FIG. 17. Skew T–log$p$ diagram for the background temperature (solid line), dew-point temperature (dashed line) and wind vector from the 1400 GMT 9 May 1979 sounding of North Platte, Nebraska.

the atmospheric structure along the jet and across it is provided in Figs. 19 and 20, respectively. These diagrams provide further evidence of the presence of strong vertical gradients of both winds and temperature, much larger than the horizontal ones. The presence of low Richardson numbers and the other characteristics of the system will be further discussed in Section 5.

4. Relating weather to the observed gravity waves

In the previous section, distinct gravity waves were isolated along two major tracks using power spectra and cross-correlation techniques. The p' traces in Figs. 8 and 9 revealed that wave activity was maximized in a region in which convective systems also developed rapidly and appeared to propagate along the wave tracks for nearly 10 h (Figs. 2 and 3). In this section, an attempt is made to determine the extent to which the gravity waves were correlated with the observed thunderstorms. To relate the gravity waves to the convective activity, pressure perturbation (p') maps were constructed at 30 min intervals and then compared with the infrared satellite imagery, radar summaries and histograms of hourly precipitation amounts.

The p' maps were constructed as follows:

1) The p' values were derived from the bandpass-filtered traces using a pass band of 1.5–4.5 h.

2) Based on the phase velocity calculations derived in Section 3, wave disturbances which could be clearly identified at individual stations were moved in a direction of 200°. This procedure is an important step for interpolating p' values between stations oriented parallel to the direction of the major wave tracks (Fig. 14). The time cross sections from Figs. 15 and 16 were used to aid in interpolating data between the stations in an attempt to alleviate the spatial aliasing problems associated with the nonuniform and sometimes sparse station density. Similar time-space conversion techniques have been used by Fujita (1955) as a necessary part of analyzing mesoscale pressure fields near thunderstorms.

3) Finally, satellite and radar data were used to further adjust the analysis in data sparse regions.

The results of the analysis are given for four time periods in Fig. 21. The positive and negative p' centers are encircled and shaded dark and light, respectively. The lines encircling these areas are not necessarily p' isobars but are constructed to illustrate distinct maxima and minima p' values along the wave tracks. Also included in Fig. 21 are the distinct convective systems as determined from the infrared satellite imagery (Fig. 3) and radar data.

The p' maps illustrate the wave tracks at 0530 and 0730 GMT (Figs. 21A and 21B), as originally defined by the correlation and spectral analysis in Section 3. At 0530, convective systems A2 and B1, defined by the satellite imagery (Fig. 3), clearly coincided with wave tracks A and B, respectively. Both convective systems were associated with a trough-ridge couplet 2A and 1B in Fig. 21 during this period.

The radar depiction indicates that the convection was rather weak in southwest Nebraska (system A2) at 0530 (26 000 ft tops embedded within rain, snow and ice pellets—Figs. 2A and 2B), but quite intense in central Nebraska (system B1) at 0535 (47 000 ft moderate to heavy thunderstorms—Fig. 2B). The development of convection along track A coincided with a distinct amplification of the p' values near IML and LBF, as discussed in Section 3 and illustrated in Fig. 8. Yet, there is no correlation between the magnitude of p' along tracks A and B (Figs. 8 and 9) and the intensity of convection (Figs. 2 and 3) in Nebraska. The p' values are of the same order of magnitude, but the intensity and heights of the convection are vastly different.

By 0730 the wave couplets 2A and 1B continued to propagate northeastward along their respective wave

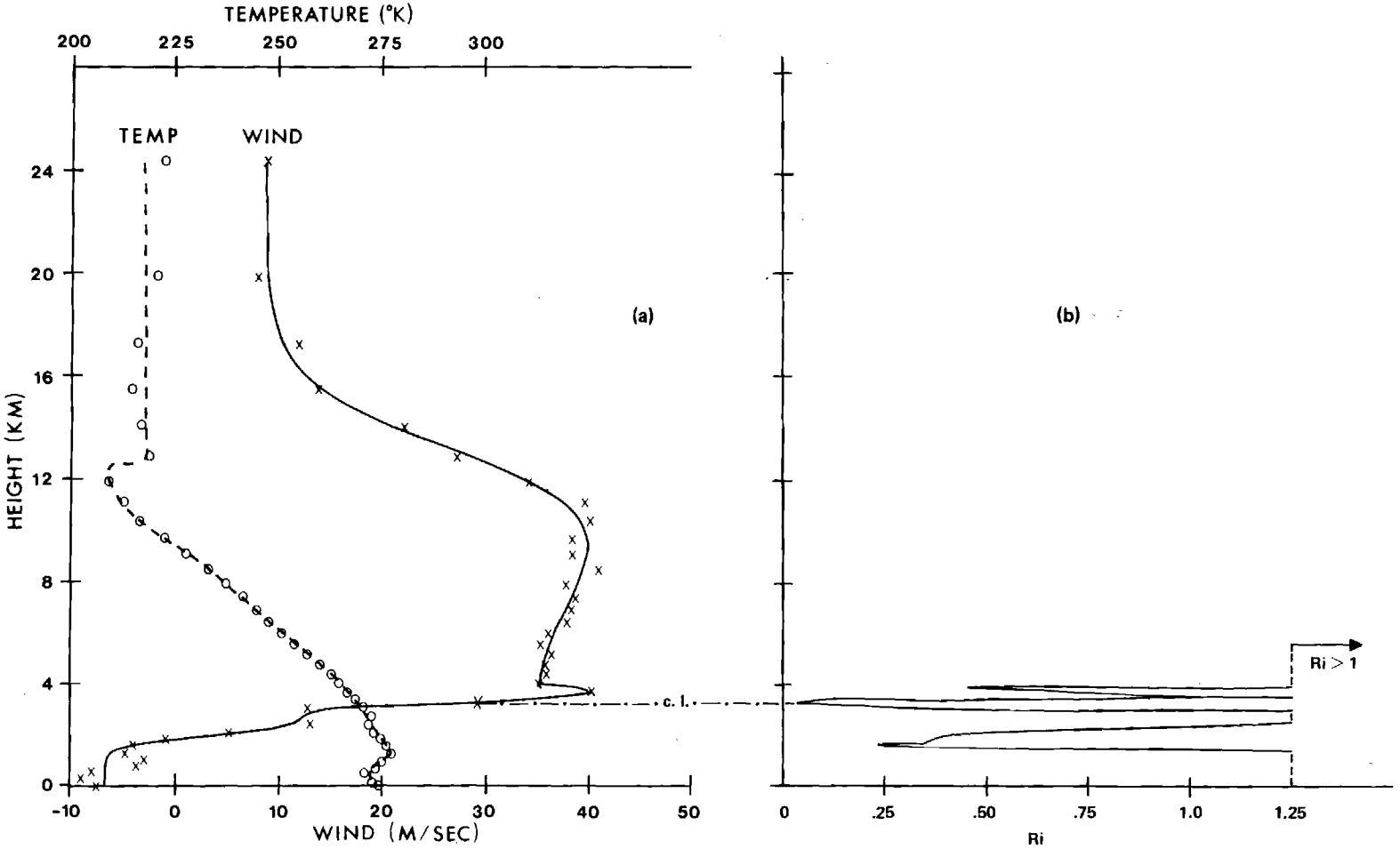

FIG. 18. (a) Mean square fit curves to the wind projected along the 200° direction (solid curve) and to the temperature (dashed line). These are the values of the temperature and wind used in studying the stability of the background state. (b) Profile of the Richardson number Ri as a function of height using the values for the temperature and wind provided in Fig. 18a and in Fig. 17. The dot-dash line between the two graphs indicates the position of the critical level, labeled c.l., for the disturbance discussed in Section 5.

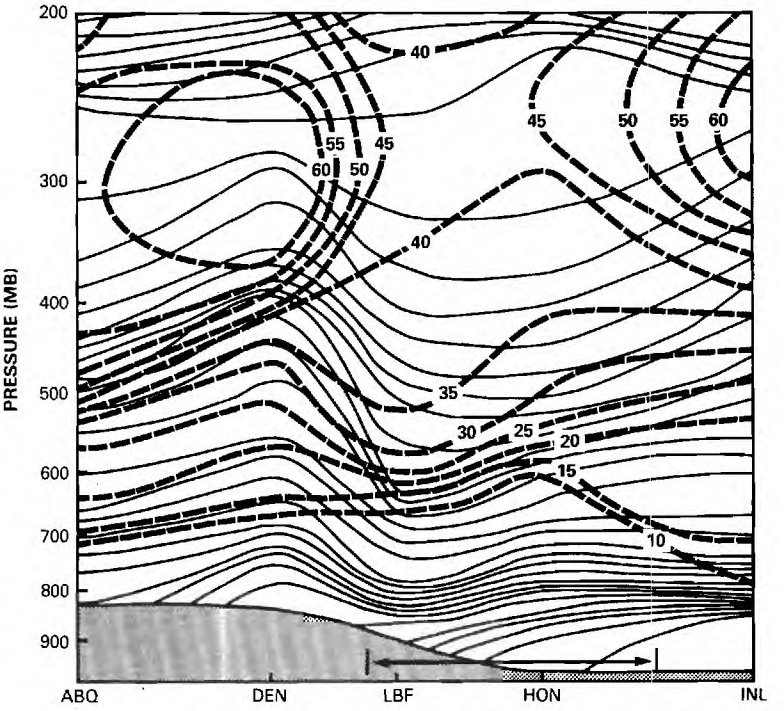

FIG. 19. Wind speed (dashed lines, m s^{-1}) and potential temperature (solid lines, each 2K) as a function of log$p$ for stations roughly aligned along the jet direction. The arrows on the horizontal axis just to the left of LBF and between HON and INL mark the boundaries of the wave corridor A.

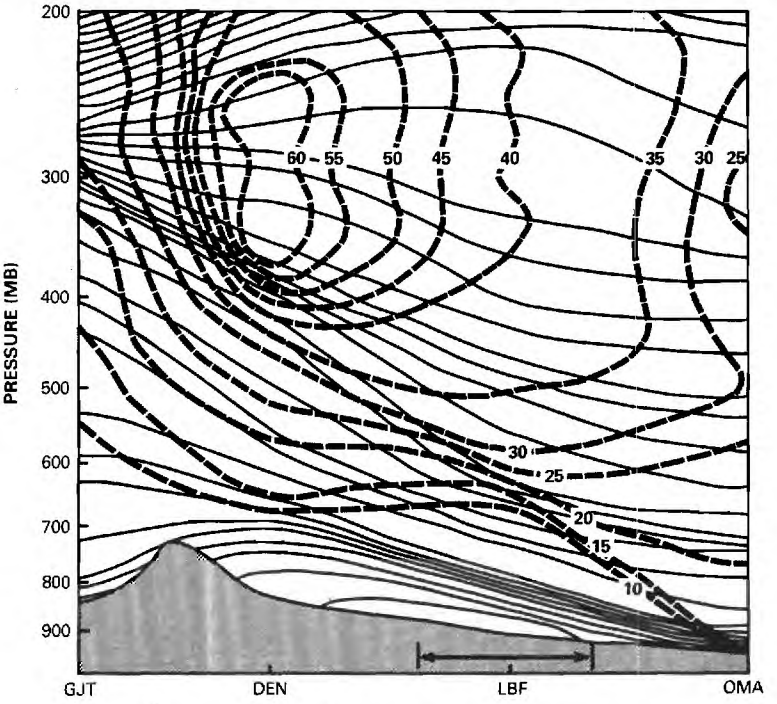

FIG. 20. Same as in Fig. 19, but for stations roughly aligned perpendicular to the jet direction.

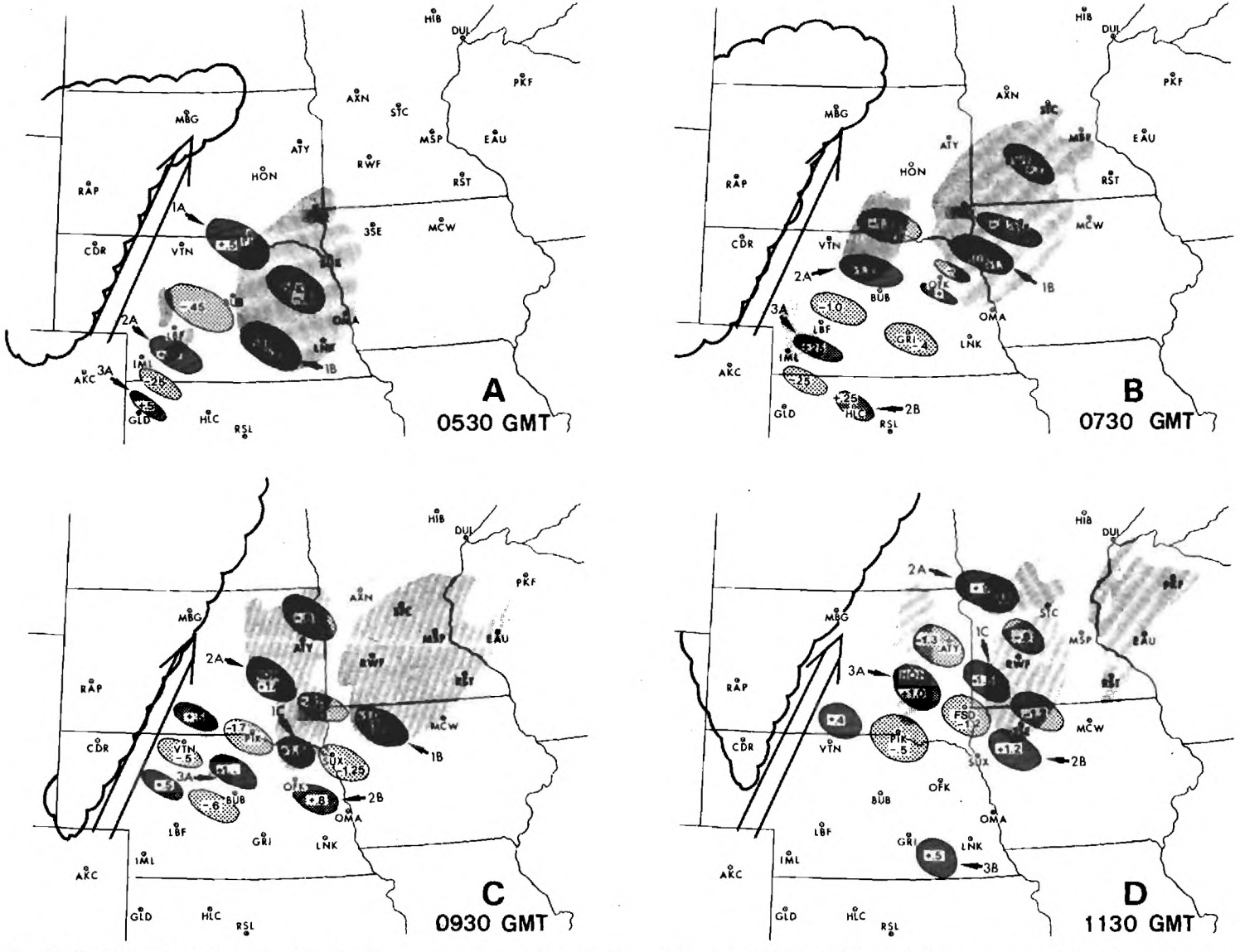

FIG. 21. Positive and negative p' centers. The lines encircling p' maxima (darkly shaded) and p' minima (lightly shaded) are not necessarily p' isobars, but are constructed to illustrate the time progression of p' values along the wave tracks. In addition, the unbordered lightly shaded areas are the thunderstorm outflow clouds as seen on the satellite pictures (Fig. 3). The arrow indicates the direction of the 1200 GMT 9 May jet.

tracks and were still associated with the distinct convective systems. The cells associated with system 1B continued to be quite intense with tops reaching 50 000 ft (Fig. 3D), while the cells with system 2A in South Dakota remained in the moderate range attaining heights near 37 000 ft (Fig. 2D). A new convective system (system A3 in Fig. 3) was now *developing* in southwest Nebraska, as inferred by the satellite imagery sequence (Fig. 3), as wave couplet 3A propagated northeastward into that area from northwest Kansas (Fig. 21B). Because it is shallow (23 000 ft top), this area of convection is not as clearly visible in the satellite picture as B1 and A2. However, it is clearly identifiable with the aid of the radar summaries. This weak convective element was imbedded in an area of rain, snow and ice pellets (Fig. 2C). From the satellite and radar data, this appears to be the first indication of a preexisting wave apparently initiating a distinct convective system. Specifically, the wave appeared at GLD around 0500 where only light rain (0.25 cm h^{-1}) was reported between 0400 and 0500. Both the wave couplet 3A and the convective system A3 propagated northeastward into South Dakota by 1130, with the convection remaining rather weak for this system (Fig. 2G) although p' grew to values greater than 1.0 mb (Figs. 21B–21D).

Another storm (C1) appeared both in the radar and satellite images of 0830 GMT. Its development appeared to be associated with pressure maximum (1C) of Fig. 21C. Its position is consistent with the transverse structure of the track A wave, which would predict a maximum p' at 0830 between BUB and OFK. This is the position where C1 first appeared. However, since C1 appeared in the region of overlap between areas A and B (Fig. 7), C1 might have been the result of an interaction between the two tracks. A precise cause-and-effect relationship cannot be firmly established with the given station density.

After 1130, relating an individual gravity wave to specific storm cells in Minnesota and northern Wisconsin becomes more difficult. This is consistent with the poorer cross-correlations statistics in the same region as discussed in Section 3. This suggests that waves along various tracks could have been interacting with the same convective systems as these storms and tended to slow down, so they turned toward the east.

The impact of the gravity wave-thunderstorm systems upon local rainfall events is illustrated in Fig. 22. Two stations were selected along track A (LBF and STC) and two along track B (OFK and FSD). The station data show the periodic nature of the rainfall and its relationship to the pressure perturbations. Although there is no obvious correlation between the magnitude of p' and the amount of rain at any individual location, the rainfall was generally maximized just prior to the passage of a wave ridge. This observation agrees with the findings of Uccellini (1975) and Miller and Sanders (1980).

In summary, the nature of the convective complexes in this case was closely linked to the observed gravity waves which propagated from southwest and southern Nebraska toward Minnesota along two major tracks. The convection was associated with the waves in the expected manner with the cell intensity and height and associated rainfall rates being maximized near the wave ridge. There is evidence that p' maximum 3A existed without convection and subsequently initiated convective cells along the wave track. There are cases where the waves remained with specific convective cells along a significant portion of the wave track. In all cases, the amplitude of the p' traces (Fig. 8 and 9) increased in magnitude once the convection developed, suggesting perhaps that a wave-CISK mechanism (Raymond, 1976) was aiding the development of the waves. *However, no correlation existed between the magnitude of the convective cells and the magnitude of the p' maxima.* Indeed, the largest p' values were observed along track A with cells approaching only 30 000 ft, while cells along track B consistently approached 50 000 ft even though p' values remained between 1.0 and 2.0 mb. Finally, a wavelength which is transverse to the direction of the main wave tracks was isolated through the p' analysis, a factor which must be accounted for in the theoretical model which follows.

5. Theoretical model

We propose in this section an analytical model for the waves discussed in Sections 3 and 4. The fact that 1) both sets of waves are located in areas marked by strong vertical shears and low Richardson numbers associated with the existence of upper tropospheric jet streaks and 2) both sets of waves are propagating along the jet direction and have a critical level within the jet, points to the possibility of wind shear being the mechanism for the excitation and development of these waves. In addition, both sets of waves develop in an area characterized by shallow, weak convection or no convection, as revealed by radar and satellite imagery. Since strong convection developed further downstream along the wave track, it seems unlikely that convection is responsible for the initial development of these waves. Given the low Ri numbers along the wave track, it appears that the vertical distribution of temperature and wind are such that the atmosphere is able to transfer a portion of its kinetic energy to wave energy. Thus, the model chosen focuses on shear instability as a mechanism that can generate and maintain the gravity waves, in contrast to models that rely on the diabatic heating as a source of wave energy (Raymond, 1976).

To produce an analytical model, a number of simplifying assumptions are introduced:

1) The background wind and temperature are independent of time. This assumption is based on the rather stagnant nature of the synoptic situation as evident in Fig. 2.

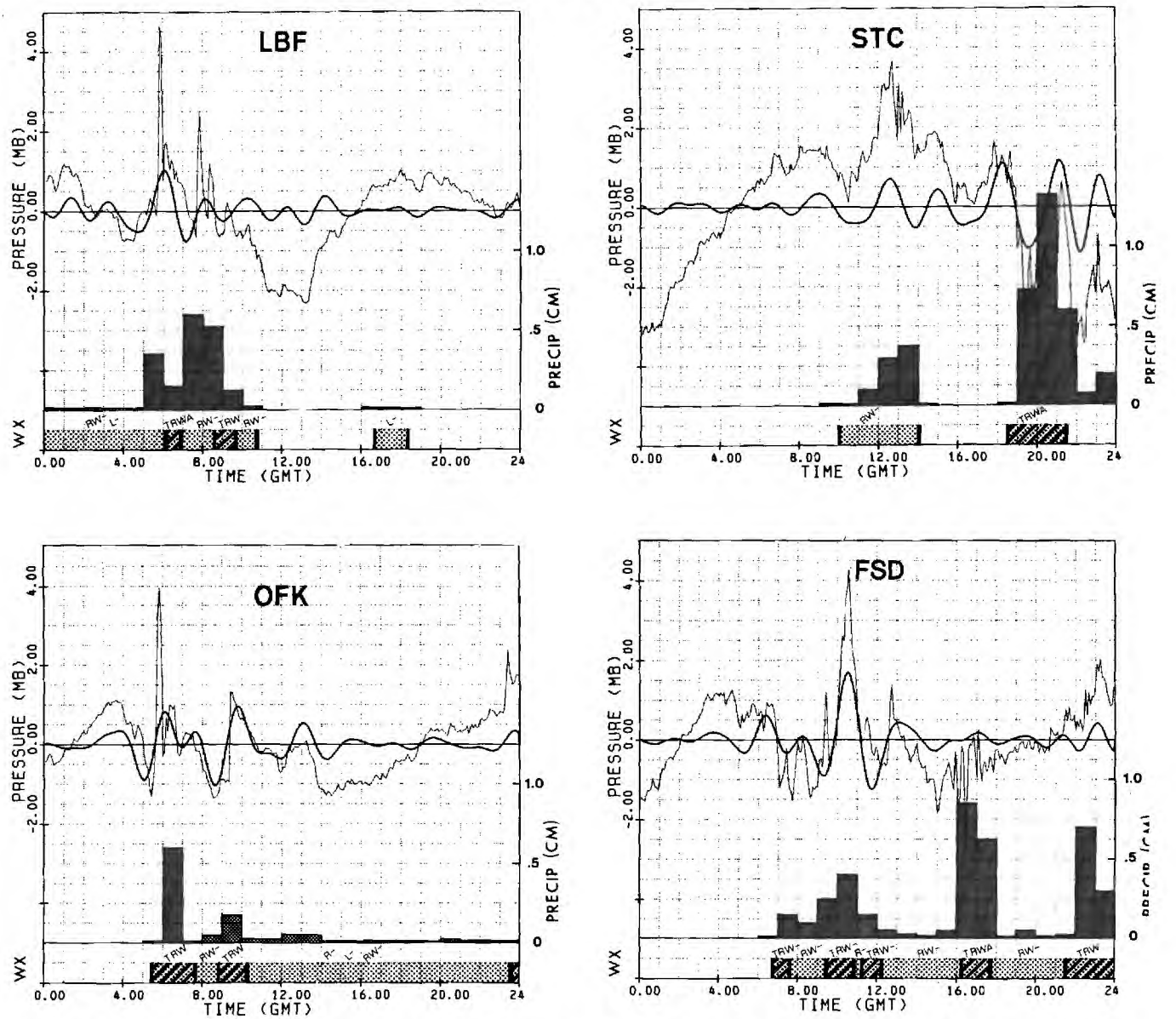

FIG. 22. Filtered and raw pressure traces along with corresponding weather and hourly precipitation. Weather is based on column 5 entries on each station surface weather observation record. Periods of precipitation are shaded and periods of thunderstorms stippled.

2) The background temperature and wind are in thermal balance, but the along-stream gradients are negligible. Rough estimates from the vertical cross section along the jet axis (Fig. 19) indicate maximum horizontal gradients well below the largest values of the vertical gradients. For the same reason, horizontal gradients of background wind in the direction perpendicular to the jet are also neglected.

3) The length of the jet is infinite. This is perhaps the weakest assumption although it is based on the fact that the distance between the trough over southern New Mexico and the ridge over northern Minnesota is of the order of 1800 km, six times the horizontal wavelength measured for the waves in Section 3.

4) The variation of the Coriolis force with latitude is negligible. The Rossby number, based on the horizontal wavelength of 300 km and a mean wind of 30 m s^{-1} (see Holton, 1979) is of the order of 6–8 so that the motion is strongly ageostrophic.

5) The equations of motion are linearized since the perturbation amplitude of 1 mb can be regarded as small compared to the mean pressure and the quadratic terms in the perturbation velocity are assumed small.

6) The disturbance is represented as a superposition of plane waves.

7) The behavior of the signals is assumed to be adequately described by one main frequency component (see power spectra, Section 3), even though the

pressure records reveal that the signals resemble more a wave packet than a monochromatic wave.

8) The Boussinesq approximation is valid.

Under the simplifying hypotheses listed above, the equations of motion can be written as

$$\rho_0 du_1/dt - f_0 v_1 + w_1(du_0/dz) = -\partial p_1/\partial x, \quad (1)$$

$$\rho_0 dv_1/dt + f_0 u_1 = -\partial p_1/\partial y, \quad (2)$$

$$\rho_0 dw_1/dt = -\partial p_1/\partial z - g\rho_1, \quad (3)$$

$$\partial u_1/\partial x + \partial v_1/\partial y + \partial w_1/\partial z = 0, \quad (4)$$

$$d\rho_1/dt + v_1 \partial\rho_0/\partial y - (\rho_0 n^2/g) w_1 = 0, \quad (5)$$

where

$$\left.\begin{aligned} n^2 &= (g/\theta_0)\partial\theta_0/\partial z = g(\beta - g/c^2) \\ \beta &= -\rho_0^{-1}\partial\rho_0/\partial z \end{aligned}\right\}, \quad (6)$$

$$d/dt = \partial/\partial t + u_0 \partial/\partial x. \quad (7)$$

The x-axis is assumed to be parallel to the jet (200°), y is positive to the left of the jet direction and z is positive upward; $u_0(z)$ and u_1 are the background and the fluctuating components of the velocity along the x-axis, v_1 and w_1 are the fluctuating components of the velocity along the y and z direction; p_0 and p_1, ρ_0 and ρ_1 are the background and fluctuating components of pressure and density, respectively; g is the gravitational acceleration, $\theta_0(y, z)$ the background potential temperature, n the Brunt-Väisälä frequency, c the speed of sound and f_0 the Coriolis parameter. Eqs. (1)–(3) are based on the conservation of momentum, (4) on the conservation of mass and (5) on the incompressibility assumption. The background quantities are related by the geostrophic wind and hydrostatic equations

$$\partial p_0/\partial y = -f_0 \rho_0 u_0, \quad (8)$$

$$\partial p_0/\partial z = -g\rho_0. \quad (9)$$

In order to determine the values of wavelengths and periods that an atmosphere governed by (1)–(9) can support, plane wave solutions are derived as follows:

$$\left.\begin{aligned} u_1(x, y, z, t) &= U_1(z)\exp(i\phi) + \text{c.c.} \\ v_1(x, y, z, t) &= V_1(z)\exp(i\phi) + \text{c.c.} \\ w_1(x, y, z, t) &= W_1(z)\exp(i\phi) + \text{c.c.} \\ p_1(x, y, z, t) &= P_1(z)\exp(i\phi) + \text{c.c.} \\ \rho_1(x, y, z, t) &= R_1(z)\exp(i\phi) + \text{c.c.}, \end{aligned}\right\} \quad (10)$$

with

$$\phi = \omega t - k_x x + k_y y.$$

The horizontal wavenumbers in the x and y directions, k_x and k_y, are related to the horizontal wavelengths λ_x and λ_y by $k_x = 2\pi/\lambda_x$ and $k_y = 2\pi/\lambda_y$. They are both assumed to be real numbers. The pulsation ω will, in general, have a real part ω_r and an imaginary part ω_i. When ω_i is negative, the solution will be unstable and grow exponentially in time. Any solution for the system (1)–(9) will then be a linear combination of various components each of which can be expressed by (10). Upon substitution of (10) into the linear system (1)–(9), the relation of U_1, V_1, P_1 and R_1 is obtained in terms of W_1

$$U_1 = \{ik_y^2(du_0/dz)W_1 + [f_0 k_y - ik_x(\omega - k_x u_0)] \times dW_1/dz\} \times [(k_x^2 + k_y^2)(\omega - k_x u_0)]^{-1}, \quad (11)$$

$$V_1 = \{ik_y k_x(du_0/dz)W_1 + [ik_y(\omega - k_x u_0) + f_0 k_x] \times dW_1/dz\} \times [(k_x^2 + k_y^2)(\omega - k_x u_0)]^{-1}, \quad (12)$$

$$P_1 = \rho_0\{-[ik_x(\omega - k_x u_0) + f_0 k_y](du_0/dz)W_1 + i[f_0^2 - (\omega - k_x u_0)^2]dW_1/dz\} \times [(k_x^2 + k_y^2)(\omega - k_x u_0)]^{-1}, \quad (13)$$

$$R_1 = \rho_0(-i(n^2/g)W_1 + f_0(\beta u_0 - du_0/dz) \times \{k_x k_y(du_0/dz)W_1 + [k_y(\omega - k_x u_0) - if_0 k_x]dW_1/dz\} \times [g(k_x^2 + k_y^2)(\omega - k_x u_0)]^{-1})(\omega - k_x u_0)^{-1}. \quad (14)$$

The equation for W_1 becomes

$$d^2W_1/dz^2 + E dW_1/dz + DW_1 = 0, \quad (15)$$

where

$$E = \{-2f_0[f_0 k_x/(\omega - k_x u_0) + ik_y]du_0/dz + [if_0 k_y u_0 + f_0^2 k_x u_0/(\omega - k_x u_0) + f_0^2 - (\omega - k_x u_0)^2]\beta\}[(\omega - k_x u_0)^2 - f_0^2]^{-1}, \quad (16)$$

$$D = \{[n^2 - (\omega - k_x u_0)^2](k_x^2 + k_y^2) - 2if_0 k_x k_y(du_0/dz)^2 \times (\omega - k_x u_0)^{-1} + [k_x(\omega - k_x u_0) - if_0 k_y](d^2u_0/dz^2) + [if_0 k_y - k_x(\omega - k_x u_0) + if_0 k_x k_y u_0/(\omega - k_x u_0)] \times \beta(du_0/dz)\}[(\omega - k_x u_0)^2 - f_0^2]^{-1}. \quad (17)$$

Equation (15) for W_1 can be viewed as either a generalization of the Taylor-Goldstein equation (Thorpe, 1969) to include terms depending on the Coriolis parameter, or a generalization of Eady's equation (Eady, 1949) to include vertical accelerations (Jones, 1967). For a given set of eigenvalues (ω, k_x, k_y), the eigenfunctions W_1 of Eq. (15) will be taken to satisfy the following boundary and radiation conditions:

1) At the ground, the vertical velocity is zero, i.e., $W_1(0) = 0$.

2) Above some height $z = z_f$, the background wind u_0 and temperature T_0 are assumed constant. For $z \geqslant z_f$, W_1 will reduce to

$$W_1 \sim \exp(-E_0 z/2) \times \exp(ik_z z), \quad (19)$$

where

$$k_z = \pm(D_0 - E_0^2/4)^{1/2} = (k_z)_r + i(k_z)_i, \quad (20)$$

D_0 and E_0 being the values of D and E, given by Eqs. (17) and (16), calculated at $z = z_f$. If k_z is real, the

sign in (20) will be chosen so that the wave propagates energy toward infinity. If k_z is complex, the sign in (20) will be chosen so that

$$\lim_{z\to\infty} W_1(z) = 0. \tag{21}$$

Equation (15) is solved numerically using the approach of Lalas and Einaudi (1976). A set of eigenvalues (ω, k_x, k_y) is determined by successive numerical integration until the corresponding eigenfunction $W_1(z)$ satisfies (19) and (20). The values of k_x, k_y and ω_r can be compared with those measured, while ω_i and $W_1(z)$ cannot be tested since no data are available in the present case.

Only the wave along track A is analyzed in detail using the model described above. Two radiosonde sites were located along this particular track, HON and LBF. The LBF soundings were available at nonsynoptic times from the SESAME experiment (Fig. 4). No radiosonde sites were located directly along track B.

The first step is to select a background atmosphere, i.e., the values of u_0 and T_0 to be used in the coefficients D and E of (15). The data from LBF were chosen because it is located at the beginning of wave track A. Furthermore, no pressure trace was available at HON. The temperature, relative humidity and velocity are given in Fig. 17, while the velocity projected along the direction of propagation of the wave and the Richardson number Ri are plotted in Fig. 18. The profile of the Richardson number dips below 0.25 between 3.2 and 3.5 km and it is below 1 over a substantial fraction of the first 4 km. Although the accuracy of computing the Richardson number using radiosondes is somewhat in doubt, the low Ri values are taken to be a good indication that the atmosphere is dynamically unstable against perturbations such as those described by (10).

As discussed in Section 4, the presence of a transverse structure in the pressure data suggests the existence of a pressure field such that

$$p(x, y, z, t) = A_1P(z)\exp[i(\omega_1 t - k_x x + k_y^{(1)}y)] + A_2P_2(z)\exp[i(\omega_2 t - k_x x + k_y^{(2)}y)] + \text{c.c.}, \tag{22}$$

where A_1 and A_2 are some constant to be chosen so as to match the data and $P_1(z)$ and $P_2(z)$ are normalized eigenfunctions for pressure corresponding to the two sets of eigenvalues $(\omega_1, k_x, k_y^{(1)})$ and $(\omega_2, k_x, k_y^{(2)})$, respectively. If, for $k_y^{(1)} = -k_y^{(2)} = k_y$, $\omega_1 = \omega_2 = \omega$, A_1 and A_2 were chosen so that

$$A_1P_1(z = 0) = A_2P_2(z = 0), \tag{23}$$

then (22) could be written as

$$p(x, y, z = 0, t) = 2A_1P_1(z = 0)\times \exp[i(\omega t - k_x x)]\cos k_y y + \text{c.c.} \tag{24}$$

In such a case, the superposition of two plane waves would produce a stationary pattern in the direction y for which the proper choice of the wavenumber k_y could produce the required phase difference between track A and the two stations VTN and FSD. Since both are ~100 km from the main track and 180° out of phase from it, a horizontal wavelength $\lambda_y = 2\pi/k_y = 200$ km, was selected. Using this value for λ_y and $\lambda_x = 290$ km, the following values for $\omega = \omega_r + i\omega_i$ were obtained as eigenvalues of (15):

$$\omega_1 = [5.74 \times 10^{-4} - i(1.38 \times 10^{-4})]\ \text{s}^{-1},$$

for

$$k_y^{(1)} = 3.1 \times 10^{-5}\ \text{m}^{-1},$$

$$\omega_2 = [5.77 \times 10^{-4} - i(1.37 \times 10^{-4})]\ \text{s}^{-1},$$

for

$$k_y^{(2)} = -3.1 \times 10^{-5}\ \text{m}^{-1}$$

which corresponds to the periods of $\tau_1 = 3.04$ h and $\tau_2 = 3.02$ h, and phase velocity of 26.2 m s^{-1} and 26.3 m s^{-1} respectively. The ω_i's correspond to an e-folding time of ~2 h. It appears that the approximation $\tau_1 \simeq \tau_2$ is an acceptable one and that (24) can be taken to be a wave stationary in the y-direction, at least for a period of several hours. The values of period, phase velocity and horizontal wavelength compare well with the measured values of 2.5 h, 29.4 ± 6.8 m s^{-1} and 265 km, respectively. It should be noted that (24) satisfies radiation conditions in the y-direction and its patterns are therefore periodic in y. This is, of course, a limitation of the model which does not include a y dependence of the background wind and is unable to provide a solution which tapers in y. On the other hand, the period and the horizontal wavelength, and consequently, the phase velocity, match the data along track A remarkably well.

To match the pressure maximum along track A of ~1.3 mb peak to peak as estimated from the power spectra, we have chosen the constant A to be

$$A_1 = -1.24 - 0.6i.$$

The vertical displacement ζ_1 and ζ_2 corresponding to the eigenvalues $(\omega_1, k_x, k_y^{(1)})$ and $(\omega_2, k_x, k_y^{(2)})$ are depicted in Fig. 23. The two functions are somewhat different especially near the critical level height of 3.28 km. This is the direct consequence of the coefficients D and E of (15) not being even functions of k_y. This in turn is the result of the asymmetry introduced into the system by the Coriolis force. Finally, it should be noted that since $\zeta_1(z)$ and $\zeta_2(z)$ are not the same, $P_1(z)$ and $P_2(z)$ will also not be the same. It follows then that the stationary pattern corresponding to $z = 0$ is not reproduced exactly at all heights. We have no way to assess how important this point is.

The values of ω and k_x are not very sensitive to those of k_y, including $k_y = 0$. In such a case the transverse structure could be the result of the superposition of the dominant motions along tracks A and B.

The application of this model to the LBF sounding

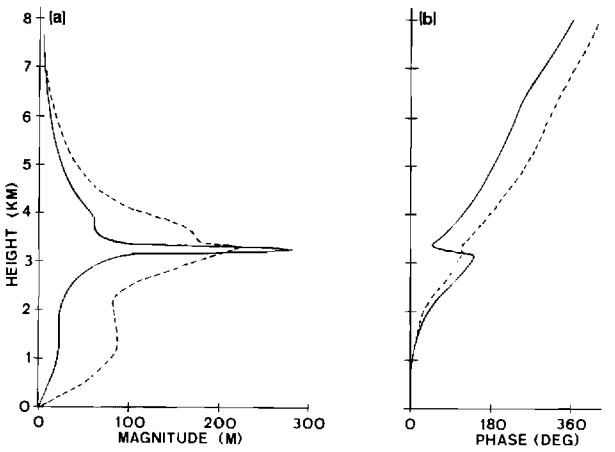

FIG. 23. Vertical displacements of (a) magnitude and (b) phase as a function of height for $k_y^{(1)} = 3.1 \times 10^{-5}$ m^{-1} (solid line) and $k_y^{(2)} = 3.1 \times 10^{-5}$ m^{-1} (dashed line).

produces a vertical displacement of only 300 m over a shallow layer of about 150 m near the 3 km level. The magnitude of the displacement and the small vertical extent of the region of larger displacements were not sufficient to produce a level of free convection at LBF. In fact at the time of the sounding, there was no strong convective activity in the LBF area. Likewise the wave induced displacement in the other available soundings, OMA and HON (the 1200 GMT STC sounding was incomplete). Unfortunately, none of these stations fall directly under the thunderstorm paths where free convection obviously did develop. Thus, we cannot really confirm that the calculated displacements could have triggered these storms. A denser observing system would have helped to clarify this issue substantially. Equally helpful would have been the availability of an MST radar which would have provided the radial velocity as a function of height essentially on a continuous basis (Lu *et al.*, 1984).

In conclusion, the analytic model appears to explain satisfactorily the wave period, horizontal wavelength and phase velocity. For $\lambda_y = 200$ km, the model predicts a horizontal phase speed of 26.2 m s^{-1} and a horizontal wavelength $\lambda_x = 290$ km to be compared with the measured values of 29.4 $\pm$ 6.8 m s^{-1} and 265 km, respectively. The model also provides an explanation for the relative phases of the pressure records of the various stations. In particular, it predicts the structure of the disturbance in the transverse direction y and it explains the phase relation between VTN and FSD and the stations along track A.

6. Summary and discussion

The analysis of a series of severe storms which occurred in the north central United States on 9 May 1979 revealed that large-amplitude, long-period gravity waves were an integral part of the entire system. The waves were coherent along two major tracks and originated near a region marked by strong vertical wind shear. For one of the two wave tracks, only weak convection was present in the region of generation. The gravity waves then propagated parallel to the axis of the jet streak, remaining in a region of strong vertical shears. In at least one area, the gravity waves appeared to initiate convective cells along the wave track, although the wave amplitude and convection appeared to grow simultaneously for most cases. A specific summary of this analysis is listed below.

1) Two major tracks for the large-scale gravity waves are isolated and defined through power spectra analysis, cross-correlation techniques and detailed pressure perturbation analyses. The analysis revealed the following characteristics:

	Track A	Track B
a) duration	10 h	10 h
b) amplitude	3 mb	2.1 mb
c) phase speed	29.4 m s^{-1}	20.2 m s^{-1}
d) period	2.5 h	3.3 h
e) wavelength	265 km	240 km

The above amplitudes are the maximum peak-to-peak values for the bandpass-filtered traces.

2) All waves existed within a 300 km wide band that extended parallel to the jet axis. The gravity waves are located on the anticyclonic side of the jet and to the north and west of the surface stationary front. Thus, the waves are confined in a region marked by significant static stability in the lower troposphere and large vertical wind shear. An analysis of several soundings along the major track (track A) isolated a region of low Richardson numbers and critical levels over a significant portion of the sounding. A linear stability analysis, using an extension of the analytical model derived by Lalas and Einaudi (1976) and applied to the soundings along the wave track, yielded an unstable wave mode for the track A gravity wave with a wave period equal to 3 h and wavelength equal to 287 km. With the low Richardson number observed along the entire track, the results of stability analysis suggest that the shear associated with the upper-level jet could provide a background environment within which a gravity wave could be initiated, with the wave energy maintained over a large distance. The existence of the wave is related, therefore, to extracting kinetic energy from the mean background state as the wave propagates in a direction parallel to the axis of the jet. Thus, in this case, the critical level should not be viewed only as a guiding mechanism which prevents leakage of wave energy upward (see Lindzen and Tung, 1976), but also

as a region where the wave will continue to extract kinetic energy from the basic state along the entire track.

3) One of the waves developed in regions of weak or no convection but then appeared to initiate deep and more intense convective clusters downstream from the point of origin. The convective system and attending rainfall were located at the ridge of the wave in agreement with other case studies (Uccellini, 1975; Miller and Sanders, 1980). The rapid amplification of the waves and the growth of the convection occurred simultaneously several hours after the waves were first isolated, indicating that the convection itself may also play a role in sustaining and strengthening the wave over a long period of time (Einaudi and Lalas, 1975; Raymond, 1976).

While this study further documents the existence of long-period, large-amplitude gravity waves and provides for a possible source mechanism related to shearing instability, many questions are left for future research. In particular, while the model calculations indicate that the observed characteristics of the waves correspond to a mode of the background atmosphere, they do not provide information about the reason such waves are excited over others of different characteristics. No strong maximum was found in the growth rate ω_i as a function of k_x and k_y in the neighborhood of the observed values. In particular, $k_y = 0$ produced no appreciably different values for k_x and ω. The actual selection as well as the characteristics of the waves may in fact be related to many other factors including the dependence of the background wind on both horizontal coordinates x and y and on the humidity distribution. It may very well be that, in some cases, the convective systems are unable to excite or maintain the waves, but are important for the selection of a wave mode of a dynamically unstable atmosphere. More research is also needed to determine the role of the geostrophic adjustment process associated with a supergeostrophic jet flow in exciting inertial-gravity waves as indicated by Matsumoto (1961). Similarly, the role of symmetric instability (Emanuel, 1982) in these cases should also be investigated.

It is possible that the resolution of some of these issues may have to wait for better observing networks and model simulations. The resolution of these problems, however, could be important in increasing our understanding of those processes which initiate and maintain severe convective storms.

Acknowledgments. This research was supported in part by Grant INT-8105101 from the National Science Foundation and through the Severe Storms Branch of the Goddard Laboratory for Atmospheric Sciences. J.G.S. wishes to acknowledge the support of the Air Force Institute of Technology. We would like to acknowledge fruitful discussions with F. Alyea, F. Canavero, D. M. Cunnold, J. J. Finnigan and R. Richiardone. We thank S. Koch and D. Keyser for their comments and reviews which have clarified portions of the manuscript.

REFERENCES

Balachandran, N. K., 1980: Gravity waves from thunderstorms. *Mon. Wea. Rev.*, **108,** 804–816.

Bosart, L. F., and J. P. Cussen, Jr., 1973: Gravity wave phenomena accompanying east coast cyclogenesis. *Mon. Wea. Rev.*, **101,** 446–454.

Eady, E. T., 1949: Long waves and cyclone waves. *Tellus,* **1,** 33–52.

Einaudi, F., and D. P. Lalas, 1975: Wave-induced instabilities in an atmosphere near saturation. *J. Atmos. Sci.*, **32,** 536–547.

Emanuel, K. A., 1982: Inertial instability and mesoscale convective systems. Part II: Symmetric CISK in a baroclinic flow. *J. Atmos. Sci.*, **39,** 1080–1097.

Eom, J. K., 1975: Analysis of the internal gravity wave occurrence of April 19, 1970 in the midwest. *Mon. Wea. Rev.*, **103,** 217–226.

Fujita, T., 1955: Results of detailed synoptic studies of squall lines. *Tellus,* 7, 405–436.

Holton, J. R., 1979: *An Introduction to Dynamic Meteorology,* 2nd ed., Academic Press, 391 pp.

Jenkins, G. M., and D. J. Watts, 1968: *Spectral Analysis and Its Applications.* Holden-Day, 525 pp.

Jones, W. L., 1967: Propagation of internal gravity waves in fluid with shear flow and rotation. *J. Fluid Mech.*, **30,** 439–448.

Koch, S. E., 1979: Mesoscale gravity waves as a possible trigger of severe convection along a dryline. Ph.D. thesis, University of Oklahoma, Norman, 195 pp.

Lalas, D. P., and F. Einaudi, 1976: On the characteristic of gravity waves generated by atmospheric shear layers. *J. Atmos. Sci.*, **33,** 1248–1259.

Lindzen, R. S., and K. K. Tung, 1976: Banded convective activity and ducted gravity waves. *Mon. Wea. Rev.*, **104,** 1602–1617.

Lu, D., T. E. Van Zandt and W. L. Clark, 1984: VHF Doppler Radar observations of buoyancy waves induced by thunderstorms. *J. Atmos. Sci.*, **41** (in press).

Matsumoto, S., 1961: A note on geostrophic adjustment and gravity waves in the atmosphere. *J. Meteor. Soc. Japan,* **39,** 18–28.

Miller, D. A., and F. Sanders, 1980: Mesoscale conditions for the severe convection of 3 April 1974 in the east-central United States. *J. Atmos. Sci.*, **37,** 1041–1055.

Palmén, E., and C. W. Newton, 1969: *Atmospheric Circulation Systems.* Academic Press, 199 pp.

Rabiner, L. R., C. A. McGonegal and D. Paul, 1979: FIR windowed filter design program-WINDOW. *Program for Digital Signal Processing,* IEEE Press, 5.1–1 to 5.1–13.

Raymond, D. J., 1976: Wave-CISK and convective mesosystems. *J. Atmos. Sci.*, **33,** 2392–2398.

Robinson, E. A., and M. T. Silvia, 1981: *Digital Foundations of Time Series Analysis,* Vol. 2. Holden-Day, 534 pp.

Testud, J., G. Breger, P. Amayenc, M. Chong, B. Nutten and A. Souvaget, 1980: A Doppler radar observation of a cold front: Three-dimensional air circulation, related precipitation system and associated wavelike motions. *J. Atmos. Sci.*, **37,** 78–98.

Thorpe, S. A., 1969: Experiments on the stability of stratified shear flows. *Radio Sci.*, **4,** 1327–1331.

Uccellini, L. W., 1975: A case study of apparent gravity wave initiation of severe convective storms. *Mon. Wea. Rev.*, **103,** 497–513.

Wang, P-Y., D. B. Parson and P. V. Hobbs, 1983: The mesoscale and microscale structure and organization of clouds and precipitation in midlatitude cyclones. IX: Wavelike rainbands associated with a cold-frontal zone. *J. Atmos. Sci.*, **40,** 543–558.

Appreed - F2

On the Effect of Dissipation on Shear Instabilities in the Stable Atmospheric Boundary Layer

D. FUÀ

F. EINAUDI

Reprinted from JOURNAL OF THE ATMOSPHERIC SCIENCES, Vol. 41, No. 5, 1 March 1984
American Meterological Society
Printed in U. S. A.

Reprinted from JOURNAL OF THE ATMOSPHERIC SCIENCES, Vol. 41, No. 5, 1 March 1984
American Meterological Society
Printed in U. S. A.

On the Effect of Dissipation on Shear Instabilities in the Stable Atmospheric Boundary Layer

D. FUÀ

F. EINAUDI

On the Effect of Dissipation on Shear Instabilities in the Stable Atmospheric Boundary Layer

D. FUÀ

Istituto di Fisica dell'Atmosfera, Ple L. Sturzo 31, 00144 Roma, Italy

F. EINAUDI

School of Geophysical Sciences, Georgia Institute of Technology, Atlanta, GA 30332

(Manuscript received 6 July 1983, in final form 9 November 1983)

ABSTRACT

We are presenting the results of a stability analysis of a background wind shear in the presence of stable stratification and of height dependent coefficients of eddy viscosity and eddy thermal conduction. It is shown that the vertical gradients of the eddy coefficients substantially affect the phase velocities, growth rates and vertical structure of the gravity wave and are responsible for the appearance of some counter-gradient heat fluxes and Reynolds stresses. It is suggested that these gradients may explain the observed counter-gradient fluxes in the stable atmospheric boundary layer.

1. Introduction

The development of the MST radars in the last five years has substantially increased our ability to detect gravity wave activities in the atmosphere in general and in the troposphere in particular. Using mean and fluctuating components of the wind determined by such radars and temperature measured by nearby radiosonde ascents, VanZandt *et al.* (1979) and Klostermeyer and Rüster (1980) have successfully interpreted their data in terms of gravity waves generated by shear in the tropospheric jet stream.

The Boulder Atmospheric Observatory (BAO)'s 300 m tower in Erie, Colorado, instrumented at eight levels with three component sonic and "Gill" propeller anemometers, fast-response temperature sensors and accurate, slow-response quartz thermometers (see Kaimal and Gaynor, 1983), has similarly led to new insight into the role of gravity waves in the stably stratified atmospheric boundary layer.

Hunt *et al.* (1983) and Lu Nai-ping *et al.* (1983) have discussed several features of wave and turbulence structures observed at the BAO, pointing out the role of wavelike motions in transporting significant amounts of heat, at times in the counter-gradient direction.

Einaudi and Finnigan (1981) and Finnigan and Einaudi (1981), also using the BAO data, have presented a detailed study of a gravity wave-turbulence event. Because of the particularly monochromatic nature of the disturbance, the mean, wave and turbulent components were separated using a phase average operator. The measured period, horizontal wavelength and vertical structure were shown to be in good agreement with linear theory. The interaction between the wave and the coexisting turbulence were shown to depend critically on the phase relationship between the gradients of the periodic components of the wind and of the periodic fluctuations of the turbulent Reynolds stresses.

The interpretation of the data in all these cases requires accurate modeling. A good analytical model will have to produce good agreement for the period and the horizontal wavelength as well as for the vertical structure of the disturbance. Our ability, for example, to interpret a counter-gradient heat flux in terms of a linear gravity wave depends on our ability to represent accurately the amplitudes and relative phase of the periodic fluctuations in the vertical velocity and potential temperature.

It is the purpose of this paper to investigate the role of a height dependent eddy viscosity κ and thermal diffusivity κ_Θ on the stability of a background wind shear in the presence of stable stratification. It will be shown that the gradients in κ and κ_Θ may be important in determining the amplitude of the disturbance, its vertical structure, its period and horizontal wavelength and, to the extent that linear theory is applicable, should be included when modeling events in the atmospheric boundary layer.

In Section 2, the equations of motion are outlined and the method of solution is discussed. The numerical solutions are presented and discussed in Section 3.

2. The equations of motion for a dissipative model

The linearized equations of motion for a stratified atmosphere in the presence of a background wind and with the Coriolis terms neglected can be written as

$$\bar{\rho}\left[\frac{d\tilde{u}_i}{dt} + \tilde{u}_j \frac{\partial}{\partial x_j}\bar{u}_i\right] + \frac{\partial \tilde{p}}{\partial x_i} + \delta_{i3} g \tilde{\rho} + \frac{\partial \tilde{r}_{ij}}{\partial x_j} = 0, \quad (1)$$

$$\frac{d\tilde{\rho}}{dt} + \bar{\rho}\frac{d\tilde{u}_j}{\partial x_j} + \tilde{u}_j \frac{\partial \bar{\rho}}{\partial x_j} = 0, \quad (2)$$

$$\bar{\rho}\left[\frac{d\tilde{\Theta}}{dt} + \tilde{u}_j \frac{\partial}{\partial x_j}\bar{\Theta}\right] + \frac{\partial \tilde{e}_j}{\partial x_j} = 0, \quad (3)$$

where

$$\tilde{r}_{ij} = -\bar{\rho}\bar{\kappa}\tilde{S}_{ij}; \quad \tilde{S}_{ij} = \frac{\partial \tilde{u}_i}{\partial x_j} + \frac{\partial \tilde{u}_j}{\partial x_i}, \quad (4)$$

$$\tilde{e}_i = -\bar{\rho}\bar{\kappa}_\Theta \frac{\partial \tilde{\Theta}}{\partial x_i}, \quad (5)$$

$$\frac{d}{dt} \equiv \frac{\partial}{\partial t} + \bar{u}_j \frac{\partial}{\partial x_j}.$$

Eqs. (1), (2) and (3) are the equations of momentum, continuity and heat transport. Dependent and independent variables are all nondimensional. The spatial coordinates x_i and time t are related to the corresponding dimensional variables, labeled with an asterisk, by

$$x_i = \frac{x_i^*}{h}, \quad t = \frac{t^* V}{h}, \quad (6)$$

where V and h are the characteristic velocity and length for the system; x_3 is directed vertically upwards. Pressure p, density ρ, potential temperature Θ and velocity u_i are normalized as follows

$$p = \frac{p^*}{\bar{\rho}_g^* V^2}, \quad \rho = \frac{\rho^*}{\bar{\rho}_g^*}, \quad \Theta = \frac{\Theta^*}{\bar{\Theta}_g^*}, \quad u_i = \frac{u_i^*}{V}, \quad (7)$$

where $\bar{\rho}_g^*$ and $\bar{\Theta}_g^*$ are the values of $\bar{\rho}^*$ and $\bar{\Theta}^*$ at the ground. The overbars in (7) and in the rest of this paper refer to mean quantities while the tildes refer to fluctuating ones. The coefficient of eddy viscosity κ, thermal conductivity κ_Θ and g are given by

$$\bar{\kappa} = \frac{\bar{\kappa}^*}{Vh}, \quad \bar{\kappa}_\Theta = \frac{\bar{\kappa}_\Theta^*}{Vh}, \quad g = \frac{g^* h}{V^2}, \quad (8)$$

where g^* is the acceleration of gravity; δ_{ij} is the Kronecker delta. The functions $\tilde{r}_{ij}$ and $\tilde{e}_i$ are the fluctuating parts of the Reynolds stress and heat flux respectively. Eddy viscosity and turbulent thermal conductivity are parameterized in analogy with molecular viscosity and conduction as discussed by Fuà *et al.* (1982). We have neglected terms containing the second viscosity coefficient because it is negligible for gravity waves in the troposphere (Klostermeyer, 1980). The relation

$$\tilde{\Theta}/\bar{\Theta} - \frac{1}{\gamma}\tilde{p}/\bar{p} + \tilde{\rho}/\bar{\rho} = 0, \quad (9)$$

with γ the ratio of the specific heats at constant pressure and volume, completes the set of 6 equations in 6 unknowns.

We carry out the stability analysis of (1), (2), (3) and (9) for the case of an atmospheric background dependent on x_3 only with $\bar{u}_2 = \bar{u}_3 = 0$. For such an atmosphere, one seeks solutions of the form

$$a(x_1, x_3, t) = a(x_3) \exp[i\alpha(ct - x_1)] + \text{c.c.}, \quad (10)$$

and one can cast the equations as

$$d\Phi/dx_3 = \mathbf{A}\Phi \quad (11)$$

where Φ is the complex column vector

$$\Phi = \begin{pmatrix} \phi_1 \\ \phi_2 \\ \phi_3 \\ \phi_4 \\ \phi_5 \\ \phi_6 \end{pmatrix} = \begin{pmatrix} d\tilde{u}_1(x_3)/dx_3 \\ \tilde{u}_3(x_3) \\ d\tilde{u}_3(x_3)/dx_3 \\ \tilde{\Theta}(x_3) \\ d\tilde{\Theta}(x_3)/dx_3 \\ \tilde{p}(x_3) \end{pmatrix}, \quad (12)$$

and $\mathbf{A}$ is the complex height dependent 6×6 matrix. (Elements are defined in the Appendix.) The quantity α is the nondimensional horizontal wavenumber, assumed real, and $c = c_r + ic_i$ is the normalized frequency of oscillation, in general complex; $i = \sqrt{-1}$ is the imaginary unit. It should perhaps be mentioned that for a plane wave solution of the type given by (10), the system of equations (11) does not depend on the choice of $\bar{u}_2$. The presence of any $\bar{u}_2(x_3) \neq 0$ would only affect the second-order differential equation governing the behavior of $\tilde{u}_2$. Once the solutions of (11) are calculated, $\tilde{u}_2$ and all related fluxes can be easily computed. Thus, for example, the extension to an Ekman layer profile is straightforward.

We define the turbulent Reynolds and Prandtl numbers, Re and Pr, both constant, as

$$\text{Re} = \frac{1}{(\bar{\kappa})_{\min}}, \quad \text{Pr} = \frac{\bar{\kappa}}{\bar{\kappa}_\Theta} = \frac{(\bar{\kappa})_{\min}}{(\bar{\kappa}_\Theta)_{\min}}, \quad (13)$$

where $(\bar{\kappa})_{\min}$ and $(\bar{\kappa}_\Theta)_{\min}$ are the minimum values of the eddy diffusivity and heat conduction. Thus, $\bar{\kappa}(x_3)$ and $\bar{\kappa}_\Theta(x_3)$ will have the following expressions

$$\bar{\kappa}(x_3) = \frac{\kappa_0(x_3)}{\text{Re}}, \quad \bar{\kappa}_\Theta(x_3) = \frac{\kappa_0(x_3)}{(\text{Pr} \times \text{Re})}, \quad (14)$$

with $\kappa_0(x_3)$ larger or equal to unity. Throughout the calculations, Pr is set equal to 1.

The linear system (11) is subject to six boundary conditions. Three conditions are applied at the ground where $\tilde{u}_1$, $\tilde{u}_3$ and $\tilde{\Theta}$ are set equal to zero, correspondent to the assumption of no slip at the rigid isothermal

bottom. The remaining three are radiation conditions imposed at values of x_3 large enough for the background wind and temperature to be treated as constant; the amplitude of the three solutions associated with viscosity, thermal conduction and buoyancy carrying energy into the shear layer are set equal to zero.

System (11) is a "stiff" system since, at any given height, it involves solutions, gravity waves and two dissipative waves, with vastly different height dependence. Such systems usually require special treatment (Acton, 1970). Klostermeyer (1972, 1980) uses a multilayer approach and a Gauss-Seidel group iteration to study the propagation of gravity waves in the thermosphere and the troposphere. We use a continuous model and a code developed by Scott and Watts (1977). The code determines the eigenvalues of (11) and the corresponding eigenfunctions satisfying the appropriate boundary conditions by successive iterative integrations carried out by the method of superposition of linear independent solutions. In addition to root-finding procedures and a Runge-Kutta-Fehlberg integration scheme with global extrapolation for estimating the integration errors, the code utilizes a Gram-Schmidt reorthonormalization scheme which is applied each time a loss of independence of the solutions is detected. We have been able to calculate eigenvalues of (11) for Reynolds numbers up to 5000 and we believe that even higher values for Re could be used although the procedure becomes very time consuming.

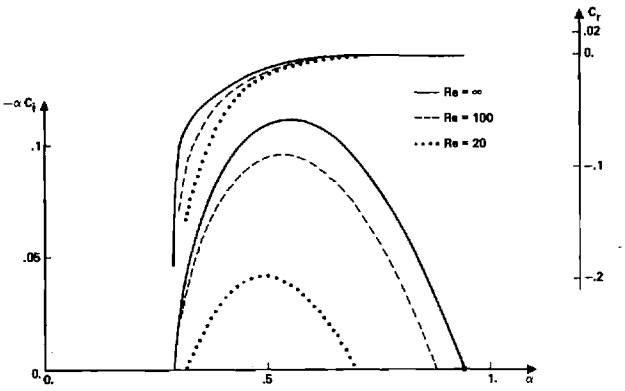

FIG. 2. Values of c_r and αc_i as a function of α for Re equal to 20, 100 and ∞ for a background defined by Model 1a: $\bar{u}_1$ as given in Fig. 1b and $\bar{T}$ is constant. The parameters used are $h/H = 0.001$, $J = 0.1$ and $\bar{T} = 280$ K.

3. Numerical results and discussion

The analysis is carried out on two background systems referred to as Model 1 and 2. Model 1 consists of an isothermal atmosphere in the presence of a background wind:

$$\bar{u}_1(x_3) = \tanh(x_3 - x_0). \tag{15}$$

We refer to this background as Model 1a when $x_0 = 5$ and Model 1b when $x_0 = 2$. The values of h/H

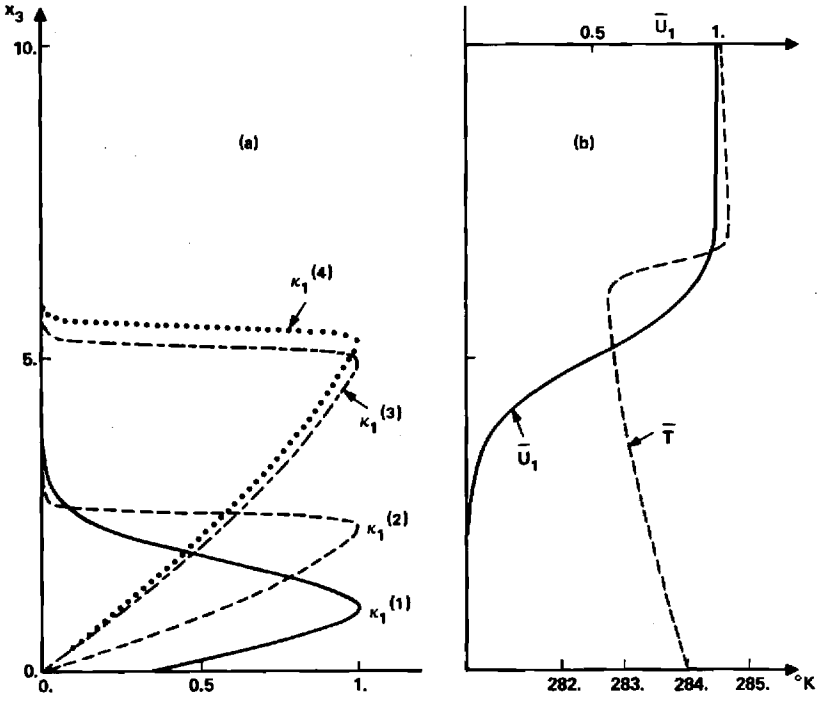

FIG. 1. (a) Profiles of the function $\kappa_1(x_3)$ defined by Eq. (16); $\kappa_1(x_3)$ is proportional to the x_3-dependent part of the eddy diffusion coefficient. (b) Background wind profile $\bar{u}_1$ and temperature $\bar{T}$ used in Model 2.

$= 0.001$, with H the scale height, and $J = n^2h^2/V^2 = 0.1$, with n^2 the Brunt-Väisälä frequency squared, are used throughout the calculations for Model 1. Model 2 is defined in terms of $\bar{u}_1$ and $\bar{T}$ plotted in Fig. 1b.

Both models are analyzed in conjunction with var-

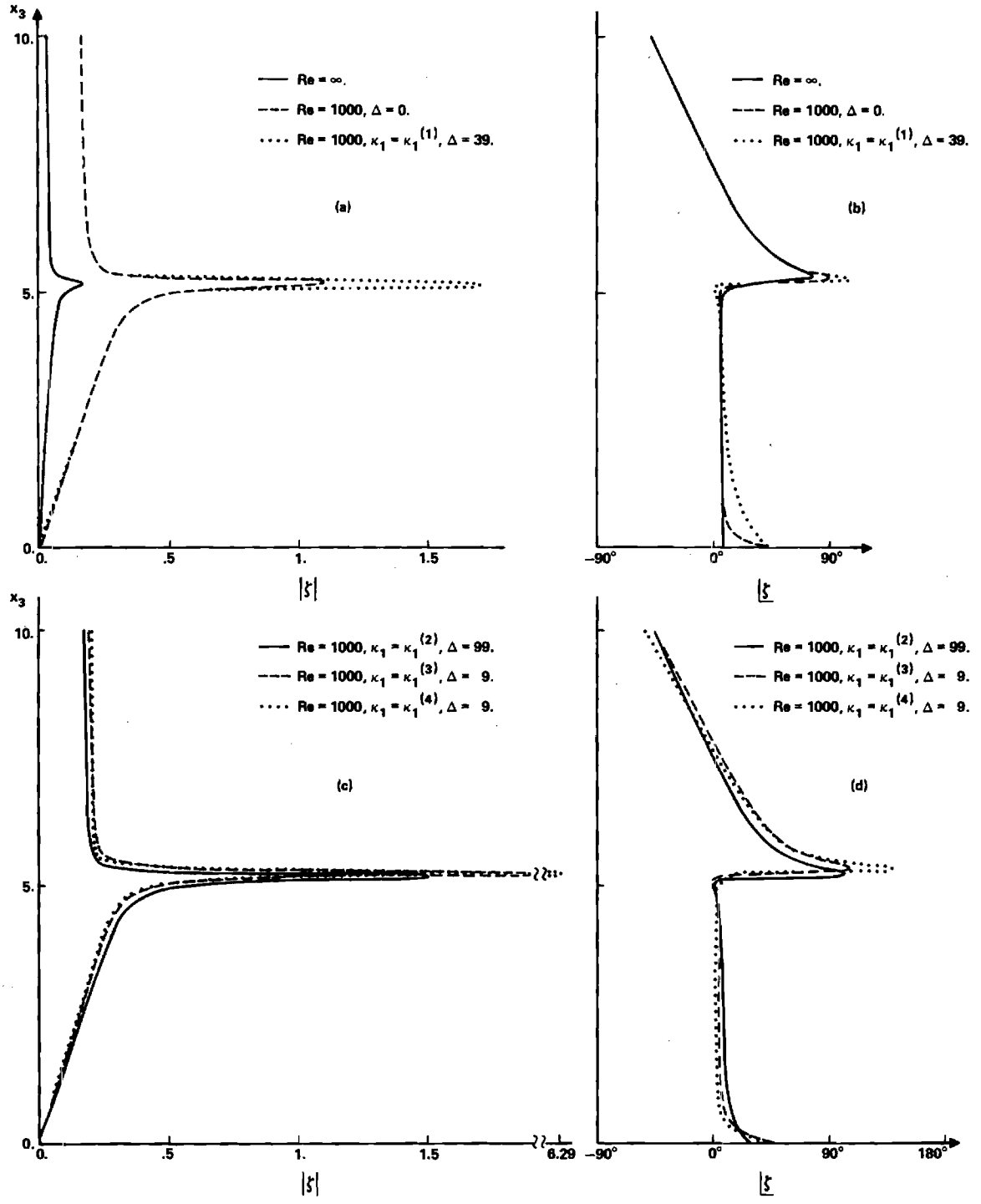

FIG. 3. Amplitudes and phases of the vertical displacements for a background defined by Model 1a. (a) and (b) describe the cases Re = ∞; Re = 1000 with $\Delta = 0$; and Re = 1000 with $\kappa_1 = \kappa_1^{(1)}(x_3)$ and $\Delta = 39$. The corresponding eigenvalues $(c_r, -c_i)$ are (0.1816, 0.0678), (0.1853, 0.0505) and (0.1689, 0.0269) respectively. (c) and (d) describe the cases Re = 1000 with $\kappa_1 = \kappa_1^{(2)}(x_3)$ and $\Delta = 99$; Re = 1000 with $\kappa_1 = \kappa_1^{(3)}(x_3)$ and $\Delta = 9$; and Re = 1000 with $\kappa_1 = \kappa_1^{(4)}(x_3)$ and $\Delta = 9$. The corresponding eigenvalues $(c_r, -c_i)$ are (0.1812, 0.0302), (0.2586), 0.0344) and (0.2821, 0.0024) respectively. All phases are relative to the pressure at the ground. The amplitudes are normalized so that the nondimensional pressure at the ground is equal to 0.1.

ious profiles of $\bar{\kappa}(x_3)$ which, for convenience of presentation, are written as

$$\bar{\kappa}(x_3) = \kappa_0(x_3)\,\mathrm{Re}^{-1} = [1 + \Delta \cdot \kappa_1(x_3)]\,\mathrm{Re}^{-1}. \quad (16)$$

The profiles of $\kappa_1(x_3)$ are given in Fig. 1a. A given normalized eddy diffusivity $\bar{\kappa}(x_3)$ will be specified by the choice of $\kappa_1(x_3)$, the Reynolds number and the numerical constant Δ. These profiles are a combination

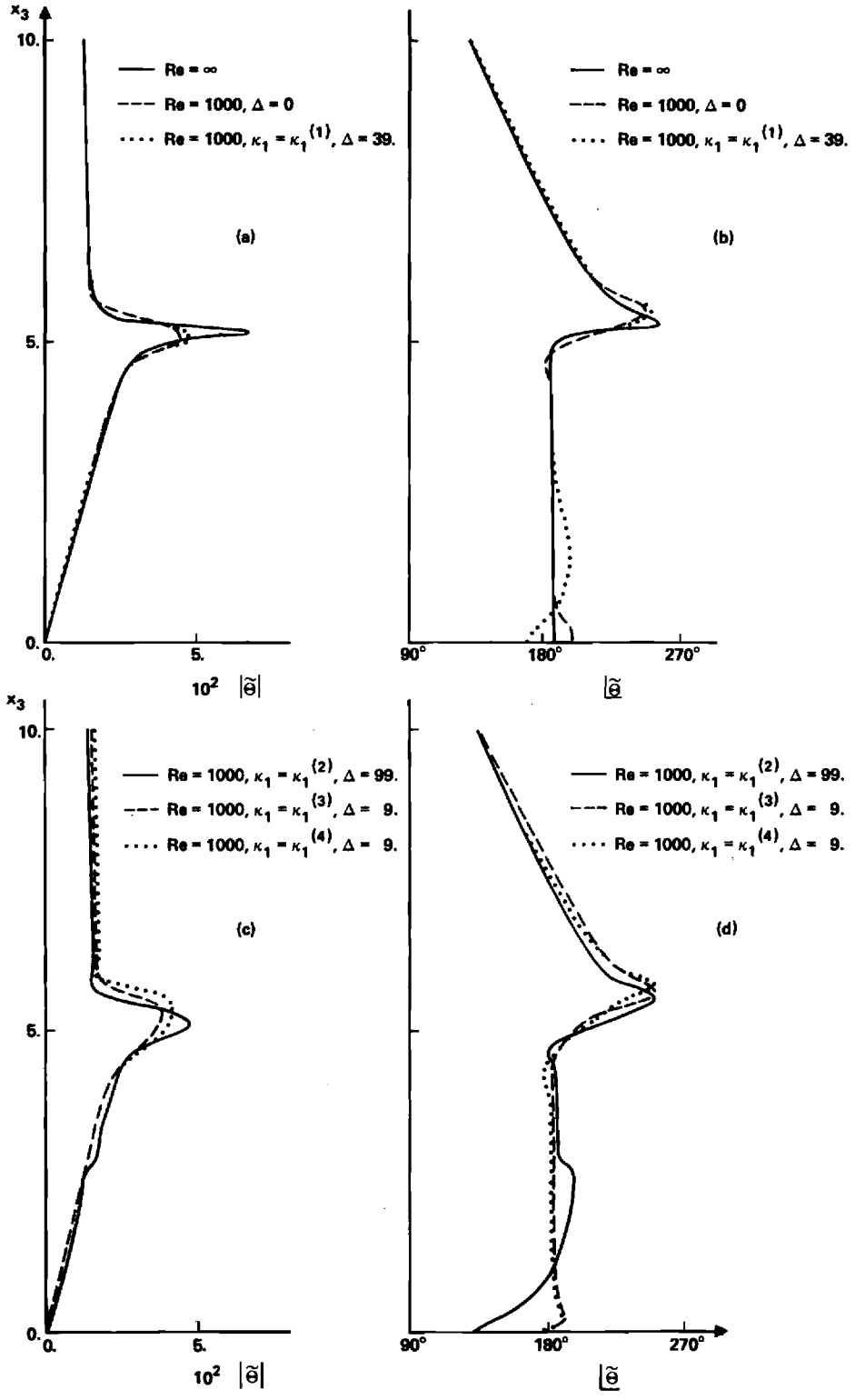

FIG. 4. As in Fig. 3 but for the amplitudes and phases of the potential temperature fluctuations $\tilde{\Theta}$.

of hyperbolic tangent and/or Gaussian functions and are in shape and magnitude quite similar to those given by Brost and Wyngaard (1978).

The cases where $\Delta = 0$ correspond to $\bar{\kappa}$ and $\bar{\kappa}_\Theta$ both constant and have been studied by Davis and Peltier (1977), where additional references may be found. They

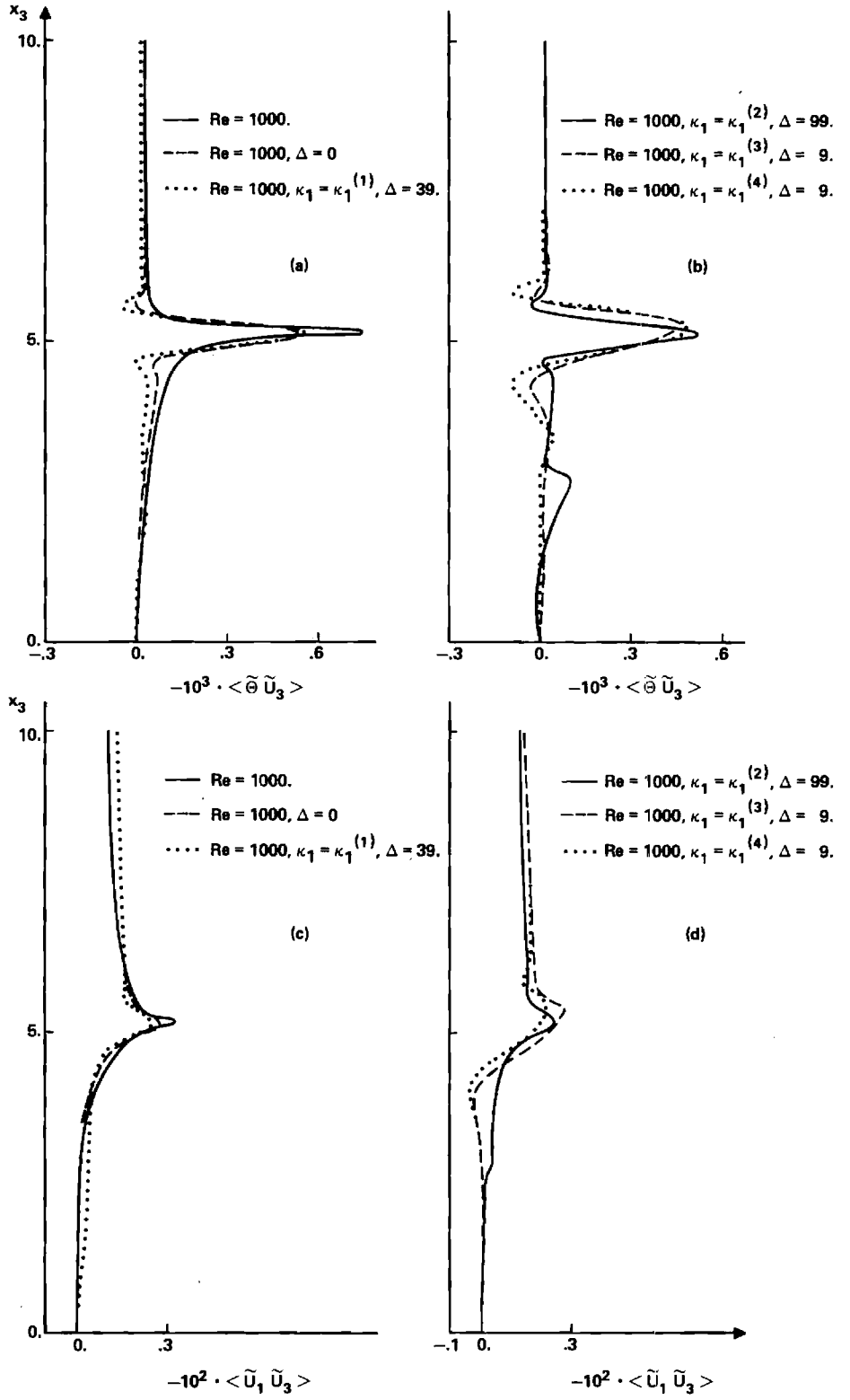

FIG. 5. Normalized heat fluxes, (a) and (b), and normalized Reynolds stresses, (c) and (d), for the cases described in Fig. 3.

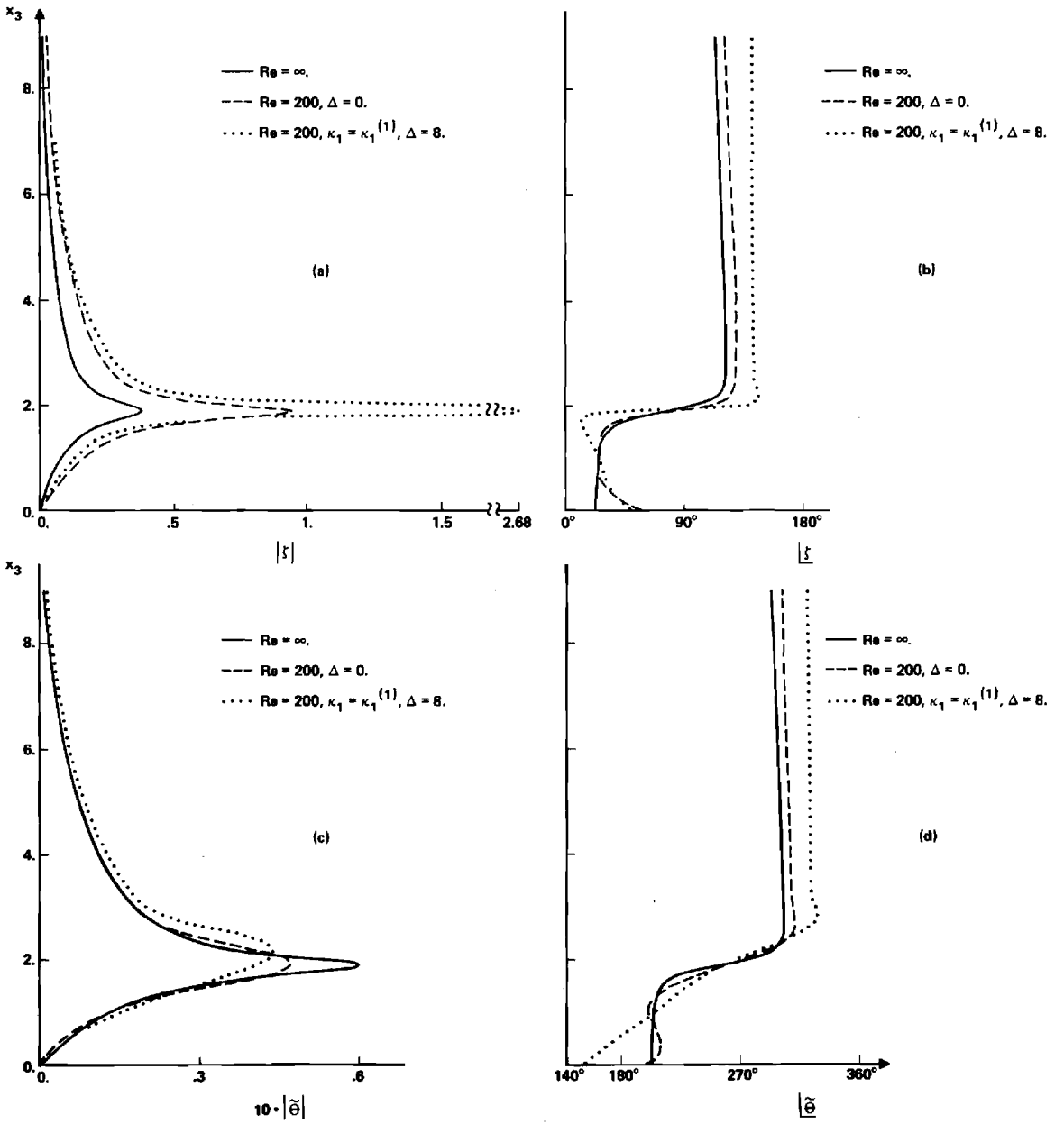

FIG. 6. (a) and (b): Amplitudes and phases of the vertical displacements for a background as in Model 1a, except that the inflection point x_0 is at 2 (Model 1b). The horizontal normalized wavenumber is now $\alpha = 0.5$. The three cases correspond to: Re = ∞; Re = 200 with Δ = 0; and Re = 200 with $\kappa_1 = \kappa_1^{(1)}(x_3)$ and Δ = 8. The corresponding eigenvalues $(c_r, -c_i)$ are (−0.1197, 0.1710), (−0.1245, 0.1364) and (−0.0843, 0.0453) respectively. (c) and (d): as in (a) and (b), but for $\tilde{\Theta}$.

carry out an extensive analysis on the effect of dissipation on the domain of instability, growth rates, phase velocities and vertical structure of the waves, for a background system characterized by a hyperbolic tangent profile for both velocity and temperature with Pr = 1 and Re < 50. Their results and in particular the reduction in the growth rates appear to extend, as they suggest, to larger values of Re as indicated in Fig. 2. The smooth transition to higher values of Re is confirmed by the calculation of the eigenvalues $(c_r, -c_i)$ performed for Model 1a and $\alpha = 0.2$ as a function of Re. Here, $(c_r, -c_i)$ has the values (0.1853, 0.0505), (0.1824, 0.0582), (0.1814, 0.0625), (0.1812, 0.0634) and (0.1815, 0.0678) as Re takes the values 1000, 2000, 4000, 5000 and ∞ respectively. Similar results are obtained if, instead of the no-slip condition at the surface, we impose the free-slip condition, as was done by Davis and Peltier (1977). In this case, for Re = 1000, $(c_r, -c_i)$ is equal to (0.1905, 0.0550). In fact, none of the results presented in this paper is sensitive to this particular boundary condition.

The results in Fig. 2 and in the rest of the paper are

obtained by integrating the equations up to $x_3 = 10$, where all the background quantities are constant.

The effect of a height dependent $\bar{\kappa}$ and $\bar{\kappa}_\Theta$ is presented for three sets of calculations.

In Figs. 3–5 the results for Model 1a are presented. The wave-number is $\alpha = 0.2$ and the unstable mode is a propagating one (see Lalas and Einaudi, 1976; Davis and Peltier, 1976). Amplitudes and phases for the vertical displacement $\tilde{\zeta}$ and potential temperature fluctuations $\tilde{\Theta}$ are plotted in Figs. 3 and 4, while the normalized heat fluxes and Reynolds stresses are given in Fig. 5 for the inviscid case and various profiles of κ_1.

Similar calculations were performed for Model 1b and $\alpha = 0.5$. Here, the inflection point in the velocity profile is closer to the ground and the mode is a classical Kelvin-Helmholtz mode exponentially decaying away from the critical level, with minimal phase variation. The results for this case are summarized in Figs. 6 and 7.

Finally, the results for Model 2 which displays an elevated temperature inversion are presented in Figs. 8–10. The phase and amplitude structure indicate that this mode, with $\alpha = 0.2$, is a propagating one.

The amplitudes of the waves have all been normalized so that the nondimensional pressure at the ground is equal to 0.1. We have adopted such normalization so as to have a uniform reference level independent of the position of the critical level. In addition, pressure measurements from microbarographs are quite reliable and often have less noisy spectra than those for other variables. This point should be kept in mind in a qualitative comparison with the results of Davis and Peltier (1977) and Klostermeyer (1980).

Numerous features appear common to the cases examined:

1) The background potential temperature has positive vertical gradients, i.e., $d\bar{\Theta}/dx_3 > 0$, in all cases examined. The heat fluxes associated with the wave are counter-gradient over various height ranges as evident in Figs. 5a, b; 7a; and 10a, b. While this phenomenon is also present in the case of constant eddy diffusivity at the edges of the region about the critical level, it is clearly much more pronounced when the height dependence of $\bar{\kappa}$ is introduced. New regions where the heat fluxes are counter-gradient appear and are, in some cases, substantial. For the Kelvin-Helmholtz wave in Fig. 7a, the counter-gradient heat fluxes are entirely due to the x_3 dependence of $\bar{\kappa}$ since they are absent for Re = 200 and $\Delta = 0$ case. In most cases, a counter-gradient heat flux is present in the region close to the ground.

2) Similar countergradient Reynolds stresses are present in some of the cases analyzed, as revealed in Figs. 5d and 10d. They are clearly related to the variations in $\bar{\kappa}(x_3)$.

3) The values of $(c_r, -c_i)$ for the various cases are reported in the captions for Figs. 3, 6, and 8. The values of c_r are all within a factor of 2 from each other. The values of c_i vary over a broader range. For $\kappa_1 \neq \kappa_1^{(4)}$, the values of c_i are all within a factor of 3.7 from each other. For the case $\kappa_1 = \kappa_1^{(4)}$ in Fig. 3, $|c_i|$

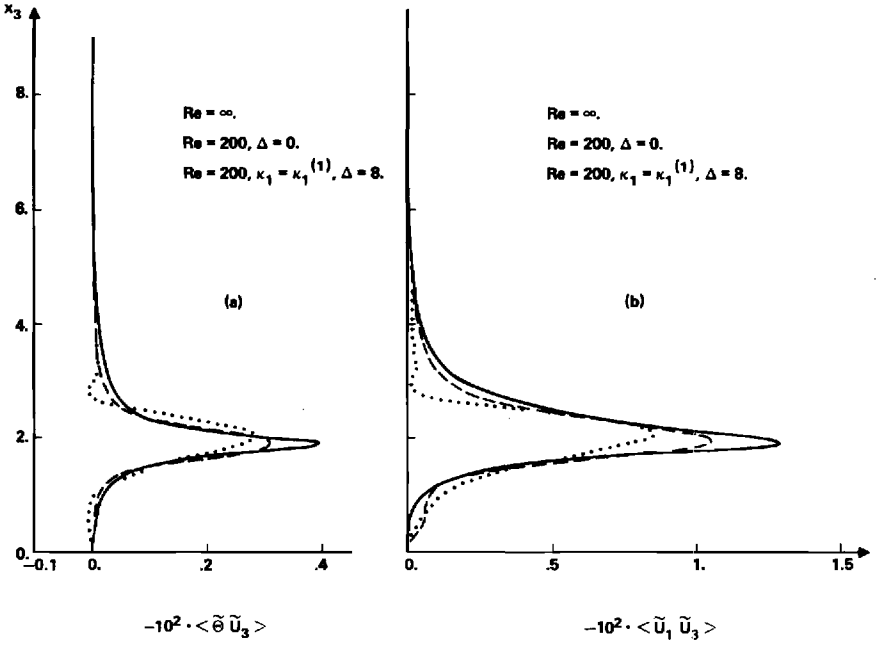

FIG. 7. Normalized heat fluxes (a) and normalized Reynolds stresses (b), for the cases described in Fig. 6.

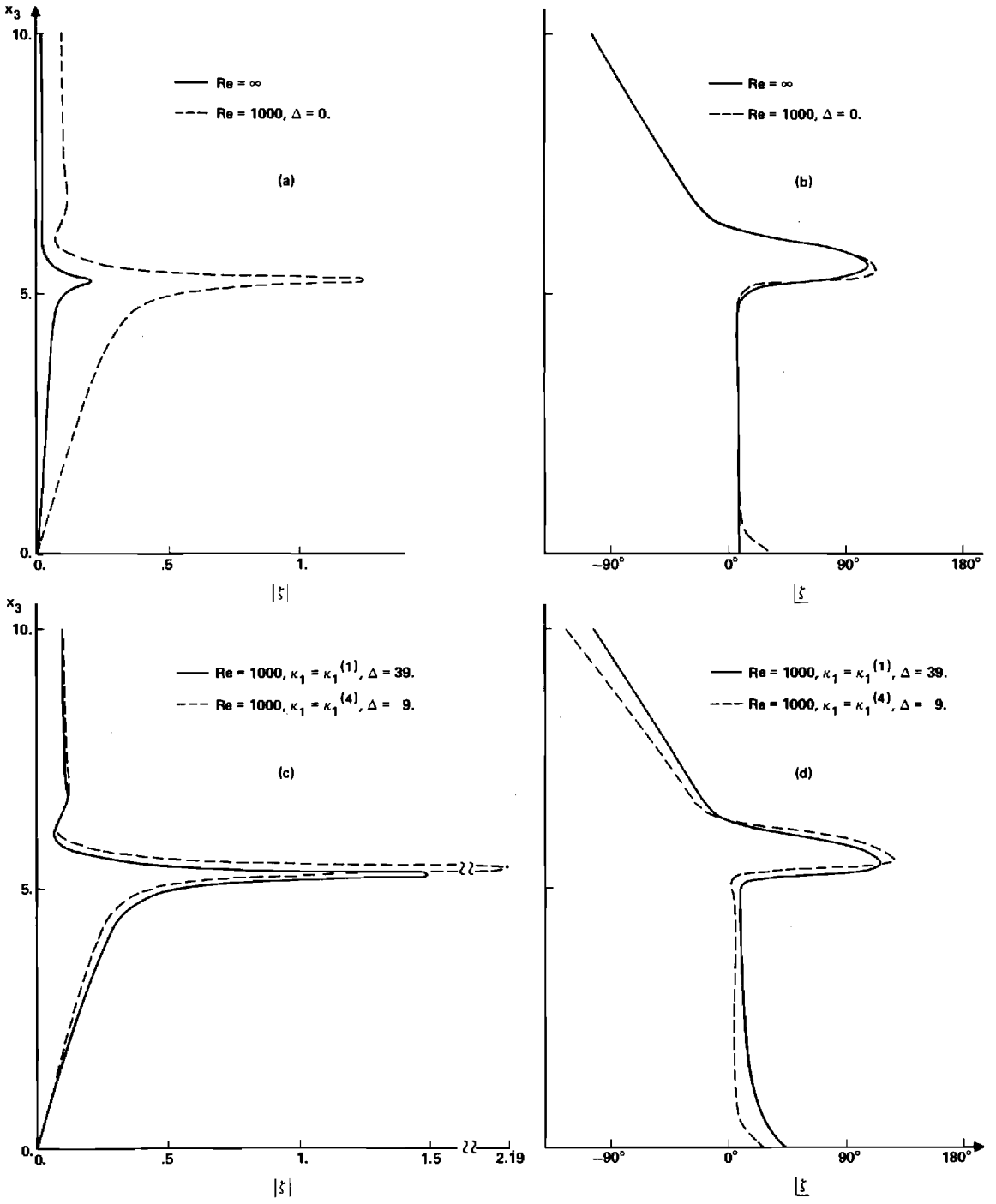

FIG. 8. Amplitudes and phases of the vertical displacements for a background defined by Model 2: $\bar{u}_1$ and $\bar{T}$ are given in Fig. 1b. The characteristic scales are h = 40 m and V = 2 m s^{-1}; α = 0.2. (a) and (b) describe the cases Re = ∞; and Re = 1000 with Δ = 0. The corresponding eigenvalues (c_r, $-c_i$) are (0.2629, 0.087) and (0.2661, 0.0741) respectively. (c) and (d) describe the cases Re = 1000 with $\kappa_1 = \kappa_1^{(1)}(x_3)$ and Δ = 39; and Re = 1000 with $\kappa_1 = \kappa_1^{(4)}$ and Δ = 9. The corresponding eigenvalues (c_r, $-c_i$) are (0.2593, 0.0602) and (0.3692, 0.0421) respectively.

for the inviscid case is approximately 1.3 times larger than $|c_i|$ for κ_1 = 1/1000 and 28.2 times $|c_i|$ for $\kappa_1 = \kappa_1^{(4)}$. This is clearly due to the fact that $\kappa_1^{(4)}$ extends into the region containing the critical level and strongly affects the wave growth.

4) From the graphs it is clear that the amplitude

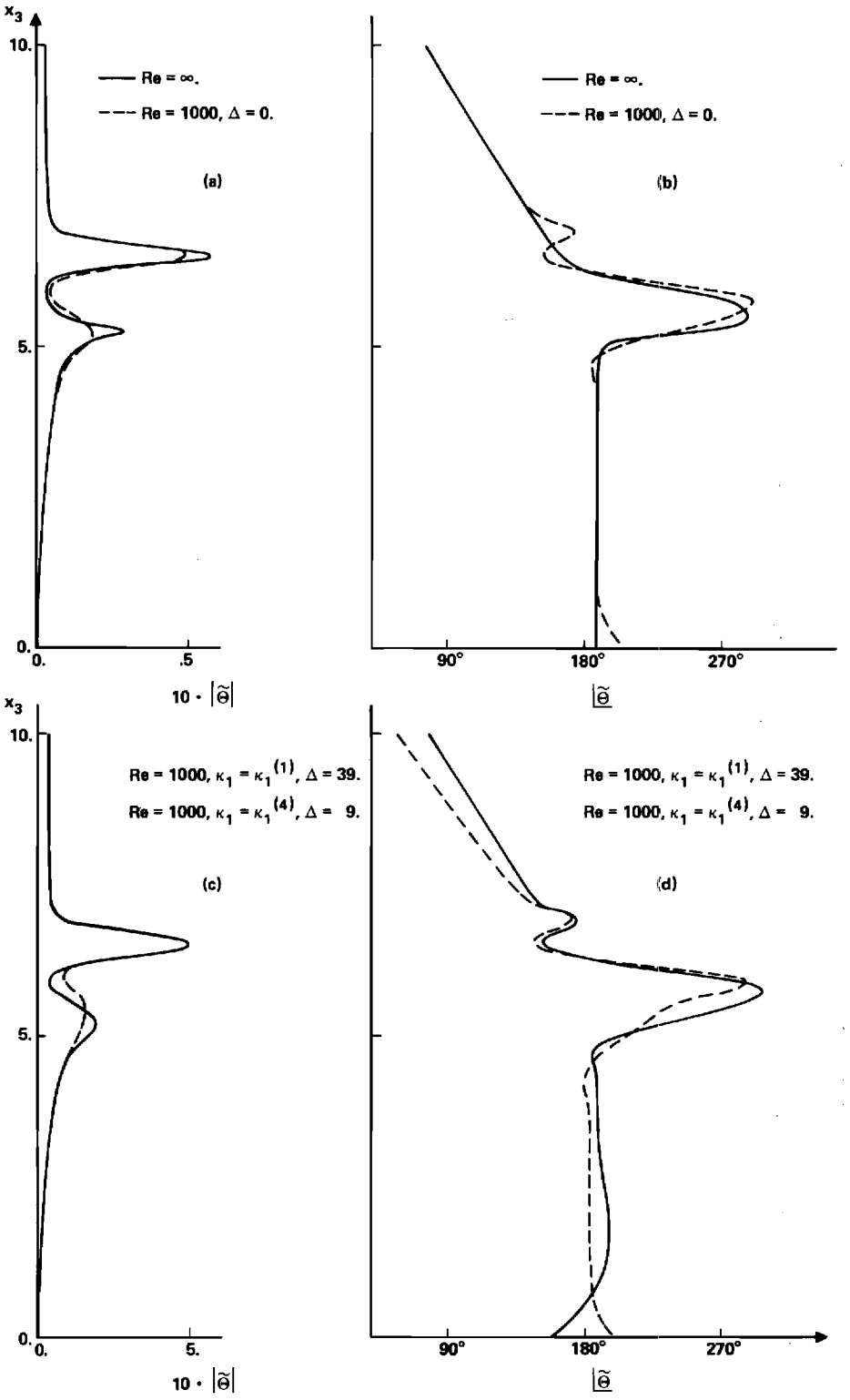

FIG. 9. As in Fig. 8 but for $\tilde{\Theta}$.

and phase of the vertical displacements and $\tilde{\Theta}$ are strongly influenced, over some height ranges, by the variations in $\bar{\kappa}$. Similar variations occur for $\tilde{u}_1$, $\tilde{u}_3$, and $\tilde{p}$, not shown here. Some of these changes can be traced to those in c_r and, more importantly, in c_i discussed above. Others are due to the local effect of the gradients

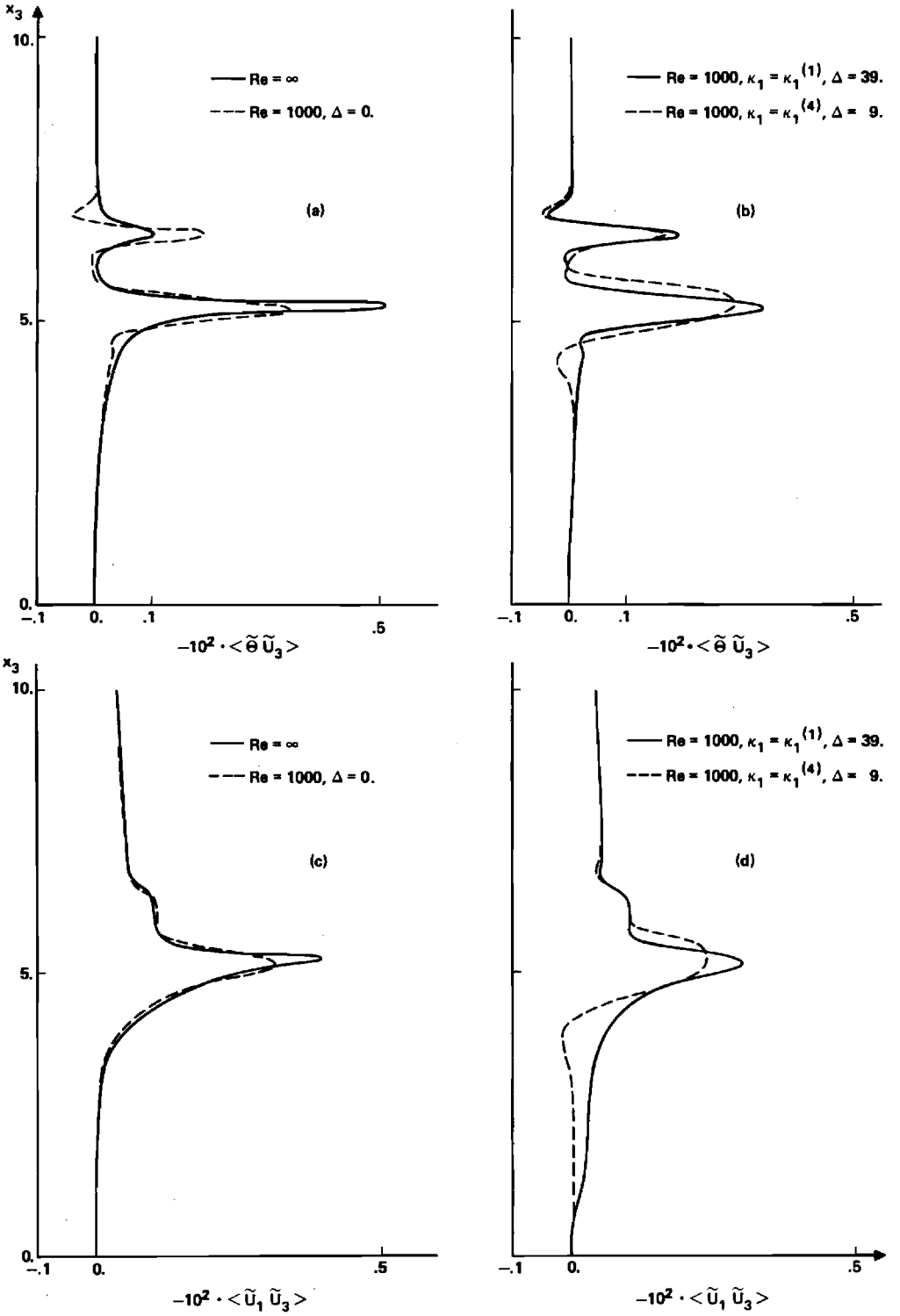

FIG. 10. Normalized heat fluxes, (a) and (b), and normalized Reynolds stresses, (c) and (d), for the cases described in Fig. 8.

of $\bar{\kappa}$. These changes in phase are indeed responsible for the appearance of counter-gradient heat fluxes and Reynolds stresses.

For Model 1, the calculations have been carried out for $h = 8.2$ m, $V = 0.48$ m s^{-1} and $T = 280$ K so that the minimum value J of the Richardson number is

APPENDIX

Elements of the Matrix A

These are the elements of the matrix **A** of Eq. (11):

$$a_{11} = \frac{-(\bar{\rho}\kappa_0)'}{\bar{\rho}\kappa_0}$$

$$a_{12} = \bar{u}' \frac{\mathrm{Re}}{\kappa_0} + \frac{i\alpha(\bar{\rho}\kappa_0)'}{\bar{\rho}\kappa_0} - i\bar{\rho}'\left(i\Omega_0 \frac{\mathrm{Re}}{\kappa_0} + 2\alpha\right)\Big/\bar{\rho}$$

$$a_{13} = -i\alpha + \Omega_0 \frac{\mathrm{Re}}{\kappa_0}$$

$$a_{14} = -\alpha\Omega_0\left(i\Omega_0 \frac{\mathrm{Re}}{\kappa_0} + 2\alpha\right)\Big/\bar{\Theta}$$

$$a_{15} = 0$$

$$a_{16} = \mathrm{Re}\left[\Omega_0\left(i\alpha\Omega_0 + 2\alpha^2 \frac{\kappa_0}{\mathrm{Re}}\right)C_0^{-2} - i\alpha\right](\bar{\rho}\kappa_0)^{-1}$$

$$a_{2i} = 0 \text{ for } i \neq 3$$

$$a_{23} = 1$$

$$a_{31} = -F\alpha\left[1 + \frac{i\alpha\Omega_0\kappa_0}{C_0^2\,\mathrm{Re}}\right]$$

$$a_{32} = -F\left[i(\bar{\rho}'/\bar{\rho})' + \alpha^2 \frac{\Omega_0}{C_0^2}\left(i\Omega_0 + \alpha \frac{\kappa_0}{\mathrm{Re}}\right)\right]$$

$$a_{33} = F\left[\frac{2\alpha\Omega_0(\bar{\rho}\kappa_0)'}{\bar{\rho}C_0^2\,\mathrm{Re}} - i\frac{\bar{\rho}'}{\bar{\rho}}\right]$$

$$a_{34} = F\alpha\left[\Omega_0 \frac{g_0}{C_0^2} + \bar{u}_1' + \Omega_0 \frac{\bar{\Theta}'}{\bar{\Theta}}\right]\Big/\bar{\Theta}$$

$$a_{35} = -\alpha F \frac{\Omega_0}{\bar{\Theta}}$$

$$a_{36} = -\alpha F\left[\bar{u}_1' + \Omega_0 g_0 \frac{(1-\gamma)'}{C_0^2}\right](\bar{\rho}C_0^2)^{-1}$$

$$a_{4i} = 0 \text{ for } i \neq 5$$

$$a_{45} = 1$$

$$a_{51} = a_{53} = a_{56} = 0$$

$$a_{52} = \bar{\Theta}'\,\mathrm{Pr}\,\frac{\mathrm{Re}}{\kappa_0}$$

$$a_{54} = i\alpha\Omega_0\,\mathrm{Re}\,\frac{\mathrm{Pr}}{\kappa_0} + \alpha^2$$

$$a_{55} = -(\bar{\rho}\kappa_0)'/(\bar{\rho}\kappa_0)$$

$$a_{61} = -F\alpha\bar{\rho}\,\frac{\kappa_0}{\mathrm{Re}}$$

$$a_{62} = F\bar{\rho}\left[\alpha\Omega_0 - i\alpha^2 \frac{\kappa_0}{\mathrm{Re}} - 2i\kappa_0(\bar{\rho}'/\bar{\rho})'/\mathrm{Re}\right]$$

$$a_{63} = 2iF\frac{\kappa_0'\bar{\rho}}{\mathrm{Re}}$$

$$a_{64} = F\bar{\rho}[ig_0 + 2\alpha\kappa_0(\bar{u}_1' + \Omega_0\bar{\Theta}'/\bar{\Theta})/\mathrm{Re}]/\bar{\Theta}$$

$$a_{65} = -2\bar{\rho}F\alpha\kappa_0\Omega_0/(\bar{\Theta}\,\mathrm{Re})$$

$$a_{66} = -F[2\alpha\kappa_0(\bar{u}_1' + \Omega_0\gamma g_0/C_0^2)/\mathrm{Re} + ig_0]/C_0^2$$

$$F = [i - 2\alpha\Omega_0\kappa_0/(\mathrm{Re}\,C_0^2)]^{-1}$$

$$C_0^2 = \gamma R\bar{T}/V^2, \quad \Omega_0 = c - \bar{u}_1.$$

R is the gas constant and prime refers to derivative with respect to x_3.

equal to 0.1 and $h/H = 0.001$, H being the scale height. Using the value 1.25 kg m^{-3} for ρ_g^*, the coefficient of eddy diffusivity $\kappa^*(x_3)$ for Re = 1000 varies over ranges comprised between 0.07 m^2 s^{-1} and 7 m^2 s^{-1} depending on the profiles of κ_1 and the values of Δ used. The results for this model are actually applicable over a very broad range of physical situations. This follows from the fact that although the calculations are carried out for the complete set of equations, only minor variations are introduced if the Boussinesq approximation is adopted, as investigated in detail by Lalas and Einaudi (1976). It follows that essentially the same results are obtained if we set $h/H = 0$. In this approximation, the results are applicable to situations in which n^2, rather than $\bar{T}$, is set equal to the mean value in the layer of interest: the only basic parameter is the minimum of the Richardson number $J = n^2h^2/V^2$ which is set equal to 0.1 in the present calculations.

The calculations for Model 2 have been carried out with $h = 40$ m and $V = 2$ m s^{-1}. For the profiles of $\kappa_1(x_3)$ and the values of Δ used, $\kappa^*(x_3)$ varies between 0.08 m^2 s^{-1} and 3.2 m^2 s^{-1}.

The values of κ^* for both models are well within the expected values for a stably stratified boundary layer (Brost and Wyngaard, 1978; Finnigan and Einaudi, 1981).

4. Conclusions

We have presented here the stability analysis of a background wind in the presence of stratification and of height dependent coefficients of eddy viscosity and thermal diffusivity. The results show that the amplitude and phase of each gravity wave variable are affected by the vertical gradients of the eddy coefficients as are the phase velocity and the growth rate of the wave.

It follows that when a comparison is attempted between a set of experimental data with sufficient height resolution, as in the case at the BAO, and a linear model output, the actual profiles for the turbulent heat fluxes and Reynolds stresses should be included. This is a particularly critical point in the analysis of the energy budgets for the wave and the coexisting turbulence as done by Finnigan and Einaudi (1981).

The inclusion of these terms will also be essential in any attempt to study a boundary layer wave event in which the critical level is sufficiently close to the ground.

Finally, it is suggested that the counter-gradient heat fluxes often observed in the atmospheric boundary layer (Lu Nai-Ping *et al.*, 1983) may be due to gravity waves in the presence of turbulence whose intensity is dependent on height. It is understood, of course, that other mechanisms, such as nonlinear wave behavior, may produce the same effect. Gradients in the eddy coefficients are shown to be responsible for the appearance of counter-gradient Reynolds stresses in some situations.

Acknowledgments. We are grateful to Drs. D. P. Lalas and R. Richiardone for various discussions on this subject. We are also indebted to Drs. M. R. Scott and H. A. Watt for providing us with the integrating routine and several discussions on its characteristics. This work was supported in part by the NOAA Grant NA80RAD00013 and in part by NSF Grants ATM-8213784 and INT-8105101. The early stages of this work were carried out at the computing facility of the National Center for Atmospheric Research, which is sponsored by the National Science Foundation.

REFERENCES

Acton, F. S., 1970: *Numerical Methods that Work.* Harper and Row, 541 pp.

Brost, R. A., and J. C. Wyngaard, 1978: A model study of the stably stratified planetary boundary layer. *J. Atmos. Sci.*, **35**, 1427–1440.

Davis, P. A., and W. R. Peltier, 1976: Resonant parallel shear instability in the stably stratified planetary boundary layer. *J. Atmos. Sci.*, **33**, 1287–1300.

—— and ——, 1977: Effects of dissipation on parallel shear instability near the ground. *J. Atmos. Sci.*, **34**, 1868–1884.

Einaudi, F., and J. J. Finnigan, 1981: The interaction between an internal gravity wave and the planetary boundary layer. Part I: The linear analysis. *Quart. J. Roy. Meteor. Soc.*, **107**, 793–806.

Finnigan, J. J., and F. Einaudi, 1981: The interaction between an internal gravity wave and the planetary boundary layer. Part II: Effect of the wave on the turbulence structure. *Quart. J. Roy. Meteor. Soc.*, **107**, 807–832.

Fuà, D., G. Chimonas, F. Einaudi and O. Zeman, 1982: An analysis of wave-turbulence interaction. *J. Atmos. Sci.*, **39**, 2450–2463.

Hunt, J. C. R., J. C. Kaimal, J. E. Gaynor and A. Korrell, 1983: Observations of turbulence structure in stable layers at the Boulder Atmospheric Observatory. *Studies of Nocturnal Stable Layers at BAO*, Rep. 4, Jan. 1983, U.S. Department of Commerce, 129 pp. A NOAA publication available from NOAA/ERL, Boulder, CO 80303.

Kaimal, J. C., and J. E. Gaynor, 1983: The Boulder Atmospheric Observatory. *J. Climate Appl. Meteor.*, **22**, 863–880.

Klostermeyer, J., 1972: Numerical calculation of gravity wave propagation in a realistic thermosphere. *J. Atmos. Terr. Phys.*, **34**, 765–774.

——, 1980: Computation of acoustic-gravity waves, Kelvin-Helmholtz instabilities and wave-induced eddy transport in realistic atmospheric models. *J. Geophys. Res.*, **85**, 2829–2839.

—— and R. Rüster, 1980: Radar observation and model computation of a jet stream-generated Kelvin-Helmholtz instability. *J. Geophys. Res.*, **85**, 2841–2846.

Lalas, D. P., and F. Einaudi, 1976: On the characteristics of gravity waves generated by atmospheric shear layers. *J. Atmos. Sci.*, **33**, 1248–1259.

Lu Nai-ping, W. D. Neff and J. C. Kaimal, 1983: Wave and turbulence structure in a disturbed nocturnal inversion. *Bound.-Layer Meteor.*, **26**, 141–155.

Scott, M. R., and H. A. Watts, 1977: Computational solution of linear two-point boundary value problems via orthonormalization. *SIAM J. Numer. Anal.*, **14**, 40–70.

VanZandt, T. E., J. L. Green, W. L. Clark and J. R. Grant, 1979: Buoyancy waves in the troposphere: Doppler radar observations and a theoretical model. *Geophys. Res. Lett.*, **6**, 429–432.

Appendix F3

October, 1985

Time and space variability of spectral estimates of atmospheric pressure

Flavio Canavero*
Franco Einaudi

School of Geophysical Sciences
Georgia Institute of Technology
Atlanta, GA 30332

*Permanent address:
Dipartimento di Elettronica
Politecnico di Torino
10129 Turin, Italy

1. Introduction

An essential element for our grasping of the behavior of the atmosphere and the ocean is the understanding of the energy exchanges among the dynamical motions at different spatial and temporal scales. Spectra are suitable tools for such a purpose: in fact, they represent the energy distribution among the sinusoidal components of any atmospheric variables, viewed as a random process. First spectra of oceanic and atmospheric variables were published by Munk et al. (1959), and Gossard (1960). The interest in the subject has intensified in recent years because of the development of remote sensing techniques which have substantially improved our ability to measure various atmospheric variables and because of the increased recognition of the meteorological significance of subsynoptic scale motions. As examples, the development of MST radars has made it possible to measure radial velocity spectra in the troposphere, stratosphere and mesosphere while such research initiatives as the Global Atmospheric Sampling Program (GASP) has provided information concerning kinetic energy spectra from a few kilometers to about 14 kilometers.

Spectra of atmospheric pressure were determined by Gossard (1960) over a wide frequency range (periods from 0.2 s up to 1 week), by Herron et al. (1969) for periods from 30 s to 10 hours and by Bull et al. (1981) over a shorter interval (2 to 128 min). Wind spectra are well covered in the literature: the papers by VanZandt et al. (1978), Balsley and Gage (1980), Ruster et al. (1980), Balsley and Carter (1982), VanZandt (1982), Lilly and Petersen (1983), and Nastrom and Gage (1983, 1985) present observations from a variety of sensors distributed in different geographical areas and looking at various altitude ranges. Temperature spectra also have begun to be published (Nastrom and Gage, 1985).

Observed spectra usually have a very similar appearance in which very few linear segments of somewhat varying slope can be used to approximate their shape. Spectral estimates of kinetic energy by various authors are summarized and discussed by Lilly (1983) in a composite figure in which the spectral obtained in the frequency domain f by Vinnichenko (1970) and Balsley and Carter (1982) have been transferred into the wave number domain k by use of the Taylor hypothesis. Typically, longer wavelength portions of the spectra are steeper than shorter wavelength ones. Thus, for example a k^{-3} dependence in the planetary wave numbers 10 to 30 (with corresponding horizontal wavelengths between 1000 and 3000 km) appears well documented (Wiin-Nielsen, 1967; Kao and Wendell, 1970; Kao, 1970; Chen and Wiin-Nielsen, 1978) while a $k^{-5/3}$ behavior seems appropriate for wavelengths less than 400-700 km (Gage, 1979; Balsley and Carter, 1982; Lilly and Petersen, 1983; Nastrom and Gage, 1983).

The interpretation of this common appearance is the subject of intense research. The k^{-3} dependence at the large scale extremum of the spectrum and the $k^{-5/3}$ at the opposite side are explained by the theory of geostrophic turbulence (Charney, 1971; Rhines, 1979) and of isotropic three-dimensional turbulence (Kolmogorov, 1941), respectively. In the intermediate range, the so-called mesoscale, where spectral levels are much higher than predicted by the decay of geostrophic turbulence, the $k^{-5/3}$ dependence is an unsettled issue. Two possibilities have been discussed for the mesoscale range: quasi-two-dimensional turbulence (Gage, 1979), leading to an upscale of energy as discussed by Lilly (1983), and a universal spectrum produced by internal and inertio-gravity waves as proposed by Dewan (1979) and VanZandt (1979).

The above slopes refer to spectra of the horizontal wind; temperature is shown to display a similar behavior (Nastrom and Gage, 1985). A model of the atmospheric pressure spectrum, deduced according to the physical interpretation of the wind spectra available in the literature, consists of an f^{-5} behavior at very long periods and of an $f^{-7/3}$ in the mesoscale range as well as at lower periods where isotropic three-dimensional turbulence dominates (Lumley and Panofsky, 1964). The transition scales (either temporal and spatial) from one regime to another are vague.

Although quite similar in appearance, the slopes and the levels of the spectra vary substantially in time and space, probably as a result of sources and sinks as well as of nonlinear transfer processes. This paper deals with this question of the non-stationarity in time and space of spectra, through measurements of atmospheric pressure collected in Northern Italy in connection with the ALPEX Experiment. The records provide information on their harmonic content for periods ranging from 20 s up to about one week. Thus, the variability of the spectra can be analyzed in detail over a very broad range of frequencies.

In section 2, the network and data collection are briefly described. The ad hoc procedure used to analyze the nonstationarity and to calculate the spectra of the data are presented in section 3, and the results are discussed for two different stations in section 4.

2. Experimental setup and data collection

An experimental campaign was conducted in Northern Italy from mid-April to mid-June 1982. The first 15 days overlapped with the ALPEX Intensive Observation Period (IOP). During that period, surface pressure measurements were carried out at 7 sites located South of the Alpine ridge

at an approximate distance of 50 Km from each other, and covering an area of about 100 x 40 km. The map of Fig. 1 shows the topography of Northern Italy and the location of the stations. The vast plain surrounded by the Alps to the North and West, and by a lower mountain ridge (The Apennines) to the South is the Po Valley. The height of the mountains ranges from about 800 m up to more than 3000 m. Six measurement stations were located in the plain at different distances from the mountains, and one was placed in a valley at the Southern edge of the Alps. In this paper, comparisons are presented between data from station A in the middle of the plain and station B in the mountains: the line of sight distance between these two stations is 275 Km.

Each station was equipped with an absolute microbarometer, two temperature sensors and a data logger. The pressure sensor was a sensitive capsule transducer connected to the atmosphere through a large pipe and housed in a box with high thermal capacity. One of the temperature sensors was used to monitor the capsule temperature. The records are very smooth and present only traces of the daily temperature cycle (±*^{o}C, maximum). Since the sensitivity to temperature of the microbarometer is *, the absence of significant errors induced by temperature is assured. The pressure transducer provided a continuous voltage that was sampled every second and converted into a 16-bit value by the data logger. At this point the nominal resolution was 4.5 μbar, comparable with the instrumental errors. The data logger performed an on-line average over 10 samples and stored the mean on diskette every 10 s. The averaging process is equivalent to a rudimentary, but easy to implement filter, needed to eliminate the fast varying electronic noise and high frequency turbulence from the sampled signal (see section 3 for more details). Digital pressure

data were converted off line to a magnetic tape format and blended with air temperature data sampled by the same data logger at 10 minute intervals. As a consequence of the average and conversion, the final resolution of the pressure data is approximately 9 μbar.

Each station was equipped with a high precision clock, whose time was checked by the operator once every few days, at the moment of the diskette replacement. No clock failures were reported. The data base contains time references so that comparisons among events at different sites can be done. The average duration of the campaign at each site is approximately 60 days. Two stations only operated approximately 2/3 of the time, due to power failures and a malfunctioning automatic restart. Of the two stations whose data are presented here, one (station A) has only a few missing data; the other (station B) has a week-long gap in mid-May.

3. Data processing

The length and the sampling interval of the available data base allowed us to conduct a spectral analysis ranging from a time period of more than a week down to 20 s.

Spectral estimation techniques range from the conventional method employing the Fast Fourier Transform (FFT) to recent more sophisticated procedures like maximum entropy, autoregressive, maximum likelihood, etc. An extensive literature exists on this subject: a tutorial paper by Kay and Marple (1981) gives a unified overview and contains detailed bibliographical references to the various aspects of the problem. In a nutshell, the conventional FFT spectral estimation has the advantage of computational efficiency, but shows two important limitations: one is the inability to resolve close peaks, the other is a possible distortion of the

spectral shape due to leakage of energy from high density regions. The recent nonconventional techniques were devised in an attempt to overcome the above limitations of the FFT-based method. Such procedures, in turn, suffer a lack of generality, because they were developed for specific applications in radar techniques, geophysical prospecting, imaging, biomedicine, econometrics, etc., and assume different models for the input time process. The present study is not intended to investigate particular wave events, as was the case in the paper by Stobie et al. (1983) where maximum entropy was proven to be very efficient in detecting short lasting waves. Hence, the authors used the conventional FFT spectral estimation, believing with Tukey (1984) that it is sufficiently general to be adopted when only the gross features of the spectrum are investigated and no a-priori model of the random process is required or known.

A basic, often unstated, hypothesis underlying spectral estimation is the stationarity of the random process at hand. The next subsection is devoted to a discussion of the stationarity properties of the atmospheric pressure records. The way we dealt with the inherent limitations of the FFT spectral estimation technique is explained in subsection 3b.

3a Nonstationarity of the pressure records

A stationary random process is one whose statistical moments, calculated from the ensemble of its realizations, are independent of time (Bendat and Piersol, 1971; chap. 1). Thus, nonstationarity implies a variability of the spectral characteristics of the process. Since a visual inspection of the pressure records reveals the intermittent presence of random amplitude disturbances superimposed on almost daily wavelike

fluctuations, it is legitimate to wonder about the stationarity of atmospheric pressure (see Fig. 2).

Because of the wide variety of signal characteristics that can be found in a real time series, a general theory for nonstationary random processes is not known. Instead, different methods have been envisaged to explain particular categories of experimental data.

The approach described here relies on Priestley's (1965) idea of an evolutionary spectrum, i.e., of an "instantaneous" spectrum, $S(\omega;t)$, which evolves in time t. The pulsation ω is the only variable the spectral density S depends on, when the process is stationary. The meaning of the evolutionary spectrum becomes more clear for a process that is characterized by two distinct time scales. Let us suppose that the fluctuations are band-limited with an upper period T_1, and that their energy changes with a time scale T_2, much larger than T_1. Then, we can assume that the spectral characteristics of the process do not significantly vary over a certain number of periods T_1, so that traditional spectral analysis techniques can be applied. They give the ω-dependent part of the evolutionary spectrum, and ω is scaled with $1/T_1$, while the "slower" time variations are scaled with T_2. In practice, the evolutionary spectrum can be estimated by partitioning the random process into time segments, and by applying traditional techniques of spectral analysis to each interval. Let the original time series x(t) be subdivided into segments, each with N samples Δt apart. The j-th segment (with j varying from 1 to J) is

$$x_j(n) \equiv x[t = (j - 1)\, N\, \Delta t + n\, \Delta t], \qquad (1)$$

where n = 0, 1, 2, ..., N-1 is the sequence index. The discrete-time approximation of the spectral density $S(\omega,t)$ is a matrix S_{jk}, where j represents the segment number, and k is a frequency label:

$$S_{jk} = (2\Delta t/N) \mid X_{jk} \mid^2. \tag{2}$$

The quantity X_{jk} is the Fourier transform estimate of the time segment $x_j(n)$,

$$X_{jk} = \sum_{n=0}^{N-1} x_j(n)\, e^{-i2\pi kn/N}, \quad -[(N-1)/2] \leq k \leq [N/2], \tag{3}$$

where $i = \sqrt{-1}$ and [.] denotes the largest integer less than or equal to the argument. Since x(t) is real, X_{jk} is symmetric, and the factor 2 in Eqn. (1) accounts for the negative part of the spectrum, so that k=0, 1, 2, ... K=[N/2]+1.

Visual inspection of sample records and a general knowledge about atmospheric phenomena suggest a description of the mesoscale features of the pressure time series in terms of evolutionary spectra. In fact, the regime of the atmosphere at such scales is modulated by longer-lasting processes, which are the cause for nonstationarity. An example of such a dual scale phenomenon is a squall line. The inner scale T_1 can be represented by the lifetime of a single cell (e.g., 30 min; Lilly (1979); the process of generation and decay of a system of cells lasts for a time T_2, considerably longer than T_1 (e.g., 1 day), but eventually the squall line disappears and a new regime (for example, fair weather) takes over.

Nonstationarity is a consequence of the different energetic content of the changing regimes.

The pressure records collected during the experimental campaign were tested for nonstationarity. Then, once nonstationarity was ascertained, an attempt was made to determine the time scale T_2.

The search for stationarity in our data used a modified version of a scheme developed for the analysis of bursts of acoustic noise (Tsao, 1984). This choice was based on the similarity, though incomplete, of the two processes. Only a brief description of the method is given here; the interested reader is referred to the paper by Tsao (1984) and to the references therein.

The main assumption of Tsao's method is that the spectral estimate S_{jk} can be factorized into a term B_j depending only on the time subinterval, a term C_k depending on the frequency and a term D_{jk}, called the interaction term, reflecting a non-separable time and frequency behavior:

$$S_{jk} = A\, B_j\, C_k\, D_{jk}, \tag{4}$$

where A is a constant scale factor. Obviously, for a stationary process,only the C_k term will survive, whereas the absence of the D_{jk} term means that the process maintains the same spectrum during its evolution, apart from a scale factor depending on the running time. Expressing the spectral density in dB as usually done, Eqn.(4) becomes

$$Y_{jk} = 10 \log S_{jk} = \alpha + \beta_j + \gamma_k + \delta_{jk}, \tag{5}$$

where $\alpha = 10 \log A$, and so on.

The application of the variance analysis allows us to test the significance of each term in Eqn. (5).

A simplification of the above scheme can be introduced. Since coarser frequency intervals than those defined by Eqn. (3) are sufficient for a preliminary search for stationarity, a size reduction of matrix S_{jk} is obtained by grouping M frequencies together to form K/M bands. Formally, this is done by replacing Eqn. (2) with

$$S'_{jp} = \frac{1}{M}\left\{\frac{2\Delta t}{N}\sum_{k=(p-1)M}^{pM} |X_{jk}|^2\right\}, \quad p = 1, 2, \ldots, K/M, \qquad (6)$$

where p is the band index. The ratio K/M is assumed to be an integer, without lack of generality. This change will formally modify Eqn. (5) to

$$Y'_{jp} = \alpha' + \beta'_j + \gamma'_p + \delta'_{jp}, \qquad (7)$$

where the primed quantities refer to the new time segment-frequency band classification.

The quantity S'_{jp} represents by the Parseval theorem the variance of the random process in the considered frequency band, and can be directly calculated from the pressure records in the time domain, without the need for any Fourier transform calculations. This simplified procedure is considered to be sufficient at this stage where one deals with a preliminary test of the process stationarity. Moreover, computation time is saved by doing variance calculations, and the matrix S'_{jp} requires (K/M)(M-1)xJ less storage locations than using all K frequencies.

The original pressure record was passed through a battery of bandpass digital filters to generate a set of 10 time series, each of which "only" contained fluctuations in one single band. Filtering attenuates the frequency components outside the pass band: the bigger the separation from the band limits the larger the attenuation. The characteristics of the bands are listed in Table 1: the bandwidth is defined as the frequency interval between the -3 dB points of the transfer function, i.e., the maximum allowed amplitude attenuation in the pass band is 0.7. A combination of a lowpass and a highpass filter was used, so that a data reduction can be made, whenever possible. It is more convenient to postpone any further details of the filtering and decimation scheme to the next subsections. We also assume that the nonstationarity is unaffected by this process, since we used linear filters.

The variance of each time segment has been calculated as follows

$$\sigma^2_{jp} = \frac{1}{N} \sum_{n=0}^{N-1} (\xi_{jp}(n) - \bar{\xi}_{jp})^2, \qquad (8)$$

where $\xi_{jp}(n)$ represents the n-th sample of the j-th time segment for the p-th band, and it is the result of the bandpass filtering applied to the original time series x(t). The quantity ξ_{jp} is the mean value of the j-th segment for the p-th band. As stated before, σ_{jp}^2 is equivalent to S'_{jp} (Eqn. (6)), so that its value expressed in dB is used to generate the matrix Y'_{jp}.

So far, the length T_p of the time segment, for band p has not been specified. Obviously, its choice is unimportant only if the series is

stationary. Furthermore, we are not able to predict the nonstationarity time scale $(T_2)_p$. Nevertheless it is possible to find a lower limit for T_p considering the process of generation of the matrix Y'_{jp}. The filtering applied to the data base assumes that the fluctuations having periods longer than the reciprocal of the lower out-off frequency $(f_L)_p$ of band p were eliminated. Therefore, any changes of the variance of Eqn. (8), calculated for $T > 1/(f_L)_p$, indicate nonstationarity as implied by its definition. The time scale $(T_2)_p$, which is not known at this stage, might be much larger than T_p. Hence, we must choose the number of segments J so that the total time JT_p is sufficiently large. For convenience in the variance anlaysis, the time T_p was chosen to be independent of p and equal to one day which is larger than T_{10}. The above choice of T_p assures large J's for our 60-day data base. The limitation in dealing with the bands of Table 1 resides in the inability to test nonstationarity of phenomena with characteristic periods higher than a day, which would require much longer data bases.

The analysis was conducted over a sample of 14 segments, spanning from April 20 to May 3, for station A. A standard easy-to-use computer routine was adopted for the variance analysis (Hemmerle, 1982). The 14 x 10 Y'_{jp} matrix, generated as shown before, is assumed to satisfy the model of Eqn. (7): the variance analysis tests the significance of the β', γ', and δ' terms.

The results of the variance analysis are summarized in Table 2, where it is shown that the null hypothesis for any single term of the mdoel of Eqn. (7) is significantly rejected with a marginal probability less than 1%. This technique demonstrates that the pressure is nonstationary for all

the bands that were analyzed; it does not provide any information on the time T_2 when nonstationarity sets in.

The evaluation of the time scale $(T_2)_p$ is crucial for the development of the spectrum analysis technique, as discussed before. The test for stationarity proposed by Bendat and Piersol (1971; chap. 7) was used to determine the quantity $(T_2)_p$, because of its simplicity.

The difference in the current approach from Tsao's (1984) resides in the use of Eqn. (8), instead of Eqn. (6) which requires an FFT calculation for each time segment. Since the stationarity analysis must be taken before the evaluation of the spectrum of the process (in fact, the results of the former analysis will influence the choice of the latter), a method working in the time domain seems more appropriate. Moreover, our technique is computationally faster. The bandpass filtering, while essential for our approach, also becomes unavoidable when the Tsao's technique has to be applied to a data base like the one under examination, in order to reduce any possible contamination of the high frequencies by the large low-frequency amplitudes (this issue will be discussed with more details in the next subsection).

The method consists of calculating the variances of portions of the original process and counting the number of crossings of the median level: nonstationarity is claimed when this figure is significantly different from half the number of subsegments, as it would be in the case of white stationary noise. The time T_2 is estimated by increasing the number of portions until the test successfully indicates that nonstationarity has emerged. The results of the analysis are presented in Fig. 3 where the time T_2 is plotted vs. characteristic periods of the pressure fluctuations. Each point on the curve has been obtained as the average of various trials

which show a somewhat high scatter; this is partly due to the primitiveness of the analysis and partly perhaps to the different meteorological situations coincident with segments under examination. Nonetheless, the information contained in Fig. 3 is crucial insofar as it gives quantitative information about the time one would expect the stationarity to last. A criterium for the time segmentation of the signal, to be discussed in the next subsection, is based on this information.

3b Spectral analysis

The available data base consists of approximately 60 days of pressure records, sampled every 10 s, so that the spectral analysis can span over more than 5 orders of magnitude in frequency. It is also well known (e.g., Gossard, 1960) that the spectral density of the atmospheric pressure associated with large periods (greater than 24 hours, say) is many orders of magnitude higher than that found at smaller time scales.

The whole data set cannot be analyzed at one time not only for the large amount of samples, but also for the following reasons. First of all, leakage (Koopmans, 1974, chap. 9) will occur: high peaks of the spectrum will influence distant frequencies through the secondary lobes of the transform of the boxcar function which delineates the sample in time. Although this phenomenon can be controlled with tapering windows in the time domain, we believe that the high frequency part of the spectrum would be inevitably distorted by the highly energetic part at lower frequencies. The second, but most important reason, is the nonstationarity of the atmospheric pressure. In fact the analysis of the data base in one batch would contradict the idea of evolutionary spectrum, as stated in the previous subsection.

The strategy devised to overcome such problems consisted in dividing the frequency axis into bands and making an appropriate analysis in each band. The data set for any band was generated through a convenient filtering of the original records, so that it contained information relative to that band only. Leakage effects are expected to be negligible, because their origin was removed. The length of the segments to be used for spectral analysis was set according to the restrictions imposed by nonstationarity characteristics of any given band.

The subdivision of the observable frequency interval is illustrated in Fig. 4, where the transfer functions of the bandpass filters are drawn. Since the scope of a linear filter is to weight differently the Fourier components of the input signal, its transfer function $H(\omega)$ is defined by the following input/output relationship:

$$Y(\omega) = H(\omega)\, X(\omega) \tag{9}$$

where $Y(\omega)$ and $X(\omega)$ represent the Fourier transform of the output and input signal, respectively. In Fig. 4, the quantity $10 \log |H(\omega)|^2$ is plotted, and it is clear that the top flat part of the curves represents the pass band, whereas the negative dB values indicate attenuation in the stop band.

A total of 9 bands were utilized to cover the portion of the frequency axis for which sufficient data to perform the spectral estimation are available. The bandwidth between the -3 dB points of the filter transfer function is 2 octaves for the first 5 windows, and one octave for the last 4 (the octave is a frequency interval whose upper value is twice the lower one). The reason for choosing two different bandwidths is a compromise between having a low number of windows and yet being able to resolve the

spectral features. A small number of bands is required in order to reduce the processing time, since the analysis procedure that is described below must be repeated for every frequency window. On the other hand, it is known that sharp peaks in the spectrum must be expected at time periods longer than 6 hours, whereas at lower periods the spectral behavior is smoother. Slightly larger windows for higher frequencies simplify the analysis, while retaining adequate frequency resolution. The arguments used to set a relationship among the bandwidth, frequency resolution, and data lengths will be discussed later in this section.

It is noteworthy that the first band extends for 2 octaves from the Nyquist frequency of the sampled process ($f_s = (2 \times 10)^{-1}$ Hz). Negligible aliasing is then expected: in fact, the averaging done by the recording system as mentioned in section 2, and the knowledge that the spectrum presents a marked negative slope in the turbulence region, assure that the folded spectrum will quickly die out.

Data filtering was done in two steps for all but the first band. The original pressure records were initially low-passed to remove the energy components at frequencies higher than the upper cut-off of the band. At this stage, the process is over-sampled, and it can be decimated. The decimation process consists of retaining one out of N_d samples of the original data base. The N_d value was chosen so that the Nyquist frequency for the decimated record was well into the attenuation region of the low-pass filter in order to avoid aliasing. An estimate was done for the filter in use, assuming an attenuation of 60 dB and remembering that the negative slope of the spectrum helps in avoiding aliasing. Consequently, the new Nyquist frequency f_d was set to 4 times the low-pass cut-off frequency ($f_d = 4f_L$), so that $N_d = f_s/f_d$. The filtering process was

completed by high-passing the decimated record. At this point the original data base was replaced by 9 data sets each containing information on one frequency band only.

The spectral estimation method deserves some discussion, because of the opposite requirements of stationarity, uncertainty and resolution. A non-parametric technique, estimating the spectrum of a signal from the absolute value squared of its FFT was adopted. Basically, this is the time series periodogram, which is known to be a somewhat erratic estimator of the spectrum. A smoother version is obtained by taking a moving average of the raw periodogram values: this is the so-called Daniell estimator (Koopmans, 1974). The consequence is a broadening of the effective resolution bandwidth. Moreover, the finiteness of the data sample causes the Fourier transform to convulve with a sinc-shaped function, so that the form of the spectrum can be distorted. The distortion is eliminated when the sinc function approaches a δ function. Time windowing is done to approximate this process of convergence to a δ function. The relationship among the length N of the data segment under examination, the number m of adjacent spectrum values for the moving average, and the bandwidth uncertainty, β, for the Daniell estimator with time tapering is given by Koopmans, 1974)

$$N = m/(\beta\kappa\Delta t) \tag{10}$$

where κ represents the effect of the tapering window w(t):

$$\kappa = \int_0^{N\Delta t} w^4(\tau)\, d\tau \;/\; \left[\int_0^{N\Delta t} w^2(\tau)\, d\tau\right]^2. \tag{11}$$

The estimated spectrum is shown (Jenkins and Watts, 1968) to approximately follow a χ^2_r distribution with r degrees of freedom. The quantity r is relatd to the moving average width, m, by

$$r = 2m/\kappa. \tag{12}$$

The q% confidence interval is

$$\frac{r\hat{S}(f)}{a} \leq S(f) \leq \frac{r\hat{S}(f)}{b}, \tag{13}$$

i.e., the "true" spectral value S(f) for a given frequency f is comprised in the interval that depends on the estimated $\hat{S}(f)$, with a q% probability. The values of a and b are set according to

$$P(a \leq \chi_r^2 \leq b) = q/100. \tag{14}$$

Eqn. (13) also holds if the logarithm of all three terms is taken.

The wish for small error bars (i.e., large m) and high frequency resolution (i.e., small β) calls for the analysis of long data records, but it is in contrast with the need for the time series to be short enough to be considered stationary. On the other hand, reducing N while keeping m fixed makes the resolution larger and has the effect of smearing out possible peaks of the spectrum. Finally, reducing N with β fixed makes the

spectrum unreliable, because the confidence limits of the estimates become larger.

The strategy in compromising on the choice of the above parameters resulted in subdividing the frequency scale in two parts. The first 5 high-frequency bands show a marked nonstationarity as discussed in the previous subsection. The requirement for small error bars was established by postulating that a ± 2 dB error bar at 95% confidence level is acceptable. We chose r=32 effective degrees of freedom (corresponding to + 2.4/ - 1.9 dB error bar for the spectral estimate), and correspondingly we set the number of points for the moving average according to Eqn. (12). On the other hand, the effective resolution bandwidth was assumed to be at most half the lower frequency f_L of the band, i.e.,

$$\beta \leq f_L/2. \tag{15}$$

The corresponding number of samples for each segment was then calculated from Eqn. (10). The time interval $N\Delta t$ was compared with the nonstationarity time scale for the appropriate frequency band and a possible necessary reduction was obtained by compromising on β and by reducing the number of degrees of freedom (i.e., accepting larger error bars).

The remaining 4 low frequency bands are designed with a smaller effective resolution so that the peaks can be emphasized. Eqn. (15) has been substituted by the more stringent requirement $\beta \leq f_L/10$. The nonstationarity at these time scales is less severe. Instead, the total length of the data base forces an upper limit for N, so that the confidence

interval becomes the dependent parameter: somewhat higher error bars must be expected for the low frequency part of the spectrum.

Table 3 summarizes the characteristics of the 9 frequency bands, as they resulted from the application of the outlined strategy. The ratio effective-to-nominal resolution bandwidth (which happens to equal the number of degrees of freedom) ranges from 32 to 4. This in turn is reflected into the error bar values.

The analysis of the filtered signal for any single band is performed through three major steps, the first of which was the application of the smoothing window to each data segment whose length is discussed above. The particular window used here is one with very good sidelobe behavior (Nuttal, 1981)

$$w(t) = \frac{1}{W} \sum_{k=o}^{K} a_k \cos\left[2\pi kt/(N\Delta t)\right], \text{ for } |t| \leq N\Delta t/2, \qquad (16)$$

where W is a normalizing factor such that $\int w^2\, dt = 1$, and $N\Delta t$ is the segment length. Following Nuttal (1981), in order to minimize the maximum sidelobe K was chosen equal to 3 with weights $a_0 = 0.355768$, $a_1 = 0.487396$, $a_2 = 0.144232$, and $a_3 = 0.012604$. The drawback is a larger main lobe. However, the main lobe width of the window of Eqn. (16) is comparable with the expected bandwidth resolution (see β above).

The second step was to take the FFT of the windowed data segment, doubled in size with padding zeros in order to oversample the spectrum and gain a better approximation to it. Obviously, padding with zeros does not increase the bandwidth resolution of the calculated spectrum.

Finally, the spectral density was estimated via a moving average process

$$S(f_i) = \frac{1}{m} \sum_{\ell=i-m/2}^{i+m/2} |X(f_\ell)|^2 , \qquad (17)$$

where m is the width of the moving average, and f_i represents the discrete frequency at which the FFT is determined.

The choice of the outlined analysis procedure rather than the popular Welch method, (e.g., see Oppenheim and Schafer, 1975) is justified mainly by the fact that we are dealing with sample sizes that are limited, either by the intrinsic nonstationarity of the data or by the duration of the collection campaign itself. The resulting spectra are individually archived for a subsequent statistical analysis, whose aims and results are the subject of the next section.

4. Results

An overview of the energetic content of the pressure records is presented first; then, a more detailed analysis attempts to disclose spatial and temporal features of the process spectral density. Fig. 5 shows a comparison between the spectra for the two stations under investigation. Each diagram represents in a log-log scale the mean spectrum, obtained from the contributions of the 9 separate frequency bands. Each contribution is the average over all calculated spectra in the appropriate band. The upper and lower curves (not shown for periods higher than approximately 6 hours) are the envelope of all spectra. The

individual spectra have been compensated for the attenuation introduced by the bandpass filter:

$$\tilde{S}(f_i) = \frac{1}{|H(f_i)|^2} \hat{S}(f_i) \qquad (18)$$

where $\tilde{S}$ is the plotted quantity (in a logarithmic scale); $\hat{S}$ is the estimate, according to Eqn. (17); H is the filter transfer function plotted in Fig. 4 for all bands. The quantity f_i represents each of the discrete frequencies at which the estimate took place.

The mean spectrum shows a continuous and smooth behavior for lower periods, without any apparent structure. The reason is likely to reside in the averaging process itself, that tends to flatten all fluctuations. In fact, if one looks at the individual spectra, a substantial variability is present, as evidenced by the large gap between the maximum and minimum values reached by the estimates. Furthermore, this variability is statistically significant since it occurs over a range of values whichis much larger than the confidence interval of the power densities.

The two lines representing the extreme values are shown for the first 5 bands, where the departures from the mean are significant. At higher periods, the increased confidence limits and the relatively small number of samples make it difficult to establish the presence of variability in the data. On the other hand, the bumpy nature of the spectrum appears quite clear since the resolution bandwidth was kept low in that part of the frequency axis.

The absence of discontinuities (with one exception) in the spectral diagrams is a clear indication that the adopted processing technique (i.e.,

signal bandpassing and further separate spectral estimation) works well, since any aliasing problem or defective estimation of the variance in any band would have resulted in an abrupt discontinuity at the band limits. The only exception is represented by the upper envelope of the variation region for band 1 of station B: since the average curve is continuous, it has to be argued that only a small number of time segments must have been biased toward higher values of the estimates.

A comparison of the two stations reveals that the overall shape of the spectra is conserved, apart from the lower period range (less than a few minutes), where station B, located in the mountains, shows spectral densities higher by a factor of 10.

Having established that average spectra display significant temporal and spatial variability, we proceed to study their characteristics in more detail by considering the spectra of the individual time segments. To this end two quantities are assumed to be most representative of each spectrum: the slope which provides more information on the shape, and the energy level defined as the integral of the spectral density over the frequency band.

Except for the region containing sharp peaks, the spectral density $S(f)$ is often assumed to be proportional to the ν-th power of the frequency, so that these quantities are linearly related in logarithmic coordinates:

$$S^* \equiv \log S(f) = \alpha + \nu \log f = \alpha + \nu f^* \qquad (19)$$

where α is constant with respect to frequency. The slope ν, within a given frequency bnd, was calculated by approximating S^* with a straight line, in

a least-square sense. The likelihood of the straight line aproximation implied by (19) was tested following Bendat and Piersol (1971, chap. 4): the mean square residual was checked against the error that one would have for a purely random data set. The null hypothesis (i.e., absence of an obvious relationship between frequency and spectral amplitude) was almost always rejected at the 5% level of significance, which means that, with few exceptions, there is reason to believe that the spectral shape is clearly defined.

Next we evaluated the errors involved in the calculation of ν due to the uncertainties in the spectral estimates. According to Brownlee (1965, Section. 11), the resulting 95% confidence interval for the slope ν is $2\varepsilon_\nu$, with

$$\varepsilon_\nu = s_{S^*|f^*}\, t_{u-2;0.025} \left(\sum_{i=1}^{u} (f_i^* - \bar{f}^*)^2\right)^{-1/2} \qquad (20)$$

where $s_{S^*|f^*}$ is the sample standard deviation of the spectral values S^*, given the frequency f^*, with S^* and f^* defined by Eqn. (19). The quantity $t_{u-2;0.025}$ is the Student t parameter with u-2 degrees of freedom and 2.5% marginal probability on both sides of the distribution; u is the total number of discrete frequencies f^*_i in a given band, and $\bar{f}^*$ is the mean of the f_i^*'s.

To visualize the effect on the slope of the errors in estimating the spectral densities, we show in Fig. 6 three straight lines, for each of the first 5 bands. One line with slope ν corresponds to the least square fit to an arbitrary single spectrum. The other two form a wedge with slopes

$\nu \pm \varepsilon$, with ε_ν calculated from (20). Any individual spectrum whose linear approximation falls outside such a wedge, must be interpreted as coming from data with different spectral slopes. Indeed, a quick examination of the resulting ν values is sufficient to conclude that they are considerably different. Fig. 7 attempts a classification of the slopes vs. time of day for the bands 1, 2, and 3, and for the two stations examined. The classification refers to the collection time of the original data segment; for simplicity, the daily time scale has been quantized into 1-hour intervals. The curve in the middle of each diagram represents the average slope of the spectra of data segments collected at the same local time, during the 60-day campaign. The first curve on both sides of the middle one is placed one standard deviation apart; finally, the top curve indicates the maxima reached by the slope values and the bottom one is the locus of the minima.

Fig. 7 shows that the mean values, the maximum variations, and the temporal evolutions of the slopes are substantially different from band to band and from station to station. Band 1 of station B has a striking behavior: the spreading of the curves is larger than in any other diagram. While the average slope is definitely negative, there are few spectra with a positive (and high) slope. Station B has the average slope of band 1 always lower than station A, but the reverse is true for bands 2 and 3.

A diurnal variation is evident only in band 3 for both stations: the spectra tend to flatten during the afternoon hours, but night and morning hours are characterized by steeper densities.

The other quantity which we take to be representative of spectral behavior is Λ_b, the spectral density integrated over a given band:

$$\Lambda_b = \Delta f \sum_{i=1}^{u} S(f_i), \qquad (21)$$

where Δf is the nominal frequency resolution in the band, and the frequencies f_i are those for which the spectrum is estimated: f_1 is the lowest frequency of the band, f_u is the highest, and $f_{i+1} = f_i + \Delta f$.

Eqn. (21) is an approximation to the area under the spectral density in a particular frequency band: for white noise (i.e., flat spectrum), Λ_b equals the product of the bandwidth times the noise mean square level. Therefore, higher Λ_b values indicate that the process is characterized by wide fluctuations about its mean. The sequences of Λ_b values for the examined data segment show a marked variability during the 60 days of data collection; the smaller the band number (i.e., smaller periods), the higher the changes of Λ_b. An attempt to reveal a diurnal cycle was made using the rms value λ_b corresponding to Λ_b defined by Eqn. (21) (i.e., $\lambda_b = \Lambda_b^{1/2}$). The results are shown in Fig. 8, where the percentages of cases with λ_b less than a set level are plotted vs. time of day, for different bands and stations. The following levels were chosen: 7 μbar rms represent the minimum detectable signal above the quantization noise, according to the measurement resolution (see section 2); lower levels indicate the absence of a significant pressure signal. Above this, three thresholds of 15, 50, 100 μbar, respectively, were selected.

The diagrams in Fig. 8 are composite histograms: each curve represents the percentage of data segments having a variance lesser than the corresponding threshold, while the difference of the percentages of any two curves indicates the amount of data segments (in percent) with variance

higher than the lower threshold, but lower than the upper one.

One remark about Fig. 8 is that the percent occurrences of the higher rms levels increase with the band number. Moreover, station B shows a clear evidence of larger percentages for higher levels. All this is implicitly present in Fig. 5 where the spectral densities are shown to possess the same characteristics. The emphasis here is on the temporal variation: some curves show an evident pattern during the day.

5. Discussion and conclusions

We have shown in this paper that ground pressure records collected south of the Alpine massif display a nonstationary character and substantial time and space variability.

Nonstationarity implies that the statistical moments, calculated from the ensemble of the pressure realizations, depend on time. Using a Fourier series representation of the data, we have demonstrated that different frequency bands display nonstationarity time scales proportional to the corresponding time periods. Such nonstationarity should be viewed as part of the irregular behavior of the atmospheric system. The implication of irregularity for the atmosphere in general and upon weather forecasting in particular has been discussed (Lorenz, 1984). Here we have confirmed such intrinsic property of the atmosphere for periods ranging from 20 s to about 1 day and we have provided quantitative estimates of the corresponding nonstationarity scales, based on ground pressure information.

We have utilized the nonstationarity results in designing the spectral analysis procedure. Rather than let the various band widths be determined by the lengths of different segments of homogeneous data (with stationarity implicitly assumed), we have subdivided the frequency axis in bands of

equal width and chosen the length of the time segments according to the nonstationarity requirements and the desired error bars.

In order to make comparisons with the results of other authors mentioned in the introduction, we generated a mean spectrum for each station, Fig. 5, and we also determined the slopes of such mean spectra via the least square method (see Eqn. (19)). The results for the individual bands are summarized in Fig. 9, for both stations, while those for two or three adjacent bands are displayed in Figs. 9b and 9c for station A and B, respectively. The uncertainties of the slopes due to the errors of the spectral density estimates were calculated according to Eqn. (20) and are indicated by vertical bars in Fig. 9. Where the slope refers to more than one band, the error becomes comparable with the smallest single-band uncertainty: this follows from Eqn. (20), since in such cases the quantity expressing the separation of frequencies from the mean grows more rapidly than the errors of the estimated spectral values. The slopes for the higher bands have wider uncertainty bars due to the larger spectral estimation errors. Moreover, the peaks in such bands make the linear approximation less meaningful.

An analysis of Fig. 9 indicates that in the period range between approximately 1 day and 6 hours (bands 6 and 7) the spectral slopes reach their largest negative values and approach the theoretical value of -5 predicted by geostrophic turbulence (see the Introduction for a brief discussion of the physical interpretation of the spectra). Surprisingly enough, though, the slope values are substantially less negative at larger periods (band 8 and 9): it is unclear whether this departure calls for a different physical explanation or it simply implies poor performance of the least-square linear fit to the data with peaks.

The central part of the spectrum (bands 3, 4 and 5 for station A, and 4 and 5 for station B) show a slope value close to -7/3, which is theoretically predicted for the mesoscale region.

At smaller scales the spectra display considerably less negative slopes: the change in slope occurs at about 5 min and 20 min for station A and B, respectively. Such departure can probably be explained in our case as small scale turbulence or gravity wave activity related to surface roughness or topographic features. Indeed, the transition in slope begins at longer periods in station B than in station A, with B in the foothills of the mountains and A about 50 km into the plains. It is interesting to note that pressure spectra obtained by Gossard (1960) and by Herron et al. (1969) display a similar behavior with a flattening of the spectrum in the range of about 1 to 6 min and 0.5 to 4 min, respectively. The same can be said of the average spectra presented by Vinnichenko (1970) for the E-W wind components in the free atmosphere. These spectra were obtained by averaging all spectra relative to turbulence conditions deduced by flight reports and reveal an almost flat region in the range of about 1 to 15 min. Bull et al. (1981) also provide evidence of a flattening (though not as intense as ours) of the spectrum in the 2 to 5 min period range. Their results are obtained using a network of three microbarographs, with spacing less than 2 km, which allow them to calculate spectral densities in the range from 2 to 128 min and to identify wave events with a median period of 6 min and a median amplitude of 55 μbar. By comparing results from a site in a flat terrain near the Baltic Sea with those from a station 10 to 20 km from the Balcanic mountains, they show substantial increase in wave activity for the station in the foothills. All these results provide evidence for a higher energy content in the range 1-20 min between the

mesoscale, at longer periods, and three-dimensional turbulence, at shorter periods, not covered by our data.

Such higher energetic content in this transition region can be justified with the presence of an energy source. In fact, the theory that explains the mesoscale spectral density in terms of quasi-two-dimensional turbulence (Gage, 1979; Lilly, 1983) needs a small-scale source of turbulence energy, which propagates upscale in the mesoscale region and downwards into the inertial subrange (see also Fig. 1 of Gage and Nastrom, 1985). We suggest that the scales included in our transition region are compatible with the location of the proposed energy source. On the other hand, the wave activity detected by Gossard and Munk (1954), Bull et al. (1981), and others suggests a different possible interpretation for the nature of the energy source in the transition region. Energy in a form of waves is injected in such a range by one of the several mechanisms of wave generation (see Einaudi et al., 1978/79). The downward energy transfer is due to decaying waves, while triad interactions (Orlanski and Cerasoli, 1981; Fritts, 1982; Chimonas and Grant, 1984) are responsible for the energy upscaling. Further experimental evidence and, possibly, numerical simulations are needed in order to validate which mechanism explains the energy transfer more satisfactorily.

The results of Figs. 5, 7 and 8 contain additional information on the variability of the energy content of the pressure records. This is an independent proof of the process nonstationarity: the evolutionary spectrum of the data base shows different shapes and energy levels for the different time interval under examination. In section 4, statistical arguments were used to demonstrate that individual spectra calculated from independent time segments can differ from each other by much more than the error width

due to the estimation process. Moreover, the slopes of the linear approximation to the individual spectra show a variability well outside the range accounted for by the errors of the spectral amplitudes. All this implies that the slope and energy distribution among the various frequency components are not independent of time. Nor are they independent of space as revealed by a comparison of the results for station A and B contained in the various figures.

Some authors, for example Gossard (1960), Bull et al. (1981), Vinnichenko (1970), provide either individual spectra or maximum-minimum variability ranges similar to ours, for the power spectra of the atmospheric variables they consider. Others do not provide such information. All focus their attention on the shape and level of the mean spectra, and their plausible universal nature.

We believe that the substantial temporal and spatial variability indicated in our data should alert us on the consequences of the average process used in the derivation of the mean spectra. The question of whether the spectral variability is a result of competing physical mechanisms appears to us to be very important and to throw some doubt on the universality of the energy distribution, in frequency or wave number space, and on its physical origins.

Table 1. Bands utilized for the nonstationarity analysis.

Band No.	Upper frequency cutoff, f_{max} Hz	Period of the upper cuttoff, $1/f_{max}$ s	Lower frequency cutoff, f_{min} Hz	Decimation ratio in the window
1	5.0×10^{-2}	20	2.5×10^{-2}	1:1
2	2.5×10^{-2}	40	1.25×10^{-2}	1:1
3	1.25×10^{-2}	80	6.25×10^{-3}	1:1
4	6.25×10^{-3}	160	3.13×10^{-3}	1:2
5	3.13×10^{-3}	320	1.56×10^{-3}	1:4
6	1.56×10^{-3}	640	7.81×10^{-4}	1:8
7	7.81×10^{-4}	1280	3.91×10^{-4}	1:16
8	3.91×10^{-4}	2560	1.95×10^{-4}	1:32
9	1.95×10^{-4}	5120	9.77×10^{-5}	1:64
10	9.77×10^{-5}	10240	4.88×10^{-5}	1:128

Table 2. Results of the nonstationarity analysis. Significance of the terms in the model of Eqn. (7).

Cause of variance	Corresponding term in the model	Degrees of freedom for the reduced model	F-value	Significance @ 1% marginal probability
Time interval	β'_j	8	26.01	Yes
Frequency band	γ'_p	13	4.94	Yes
Interaction term	δ'_{jp}	104	1.85	Yes

Degrees of freedom for the full model are equal to 1055.

Table 3. Characteristics of the spectral analysis in each frequency band.

Band no.	Sampling interval	Samples per segment	Lower frequency cutoff	Upper frequency cutoff	Number of frequencies in the band	Nominal frequency resolution	Effective bandwidth	Error bars of the spectral estimate
	s		Hz	Hz		Hz	Hz	dB
1	10	255	1.25×10^{-2}	5.0×10^{-2}	193	1.95×10^{-4}	6.24×10^{-3}	+2.4/-1.9
2	10	1019	3.13×10^{-3}	1.25×10^{-2}	193	4.88×10^{-5}	1.56×10^{-3}	+2.4/-1.9
3	40	1019	7.81×10^{-4}	3.13×10^{-3}	193	1.22×10^{-5}	3.90×10^{-4}	+2.4/-1.9
4	160	811	1.95×10^{-4}	7.81×10^{-4}	193	3.05×10^{-6}	9.76×10^{-5}	+2.8/-2.1
5	640	321	4.88×10^{-5}	1.95×10^{-4}	49	3.05×10^{-6}	2.29×10^{-5}	+5.2/-3.3
6	2560	675	1.98×10^{-5}	4.88×10^{-5}	77	3.81×10^{-7}	1.88×10^{-6}	+6.2/-3.6
7	6400	281	7.93×10^{-6}	1.95×10^{-5}	39	3.05×10^{-7}	1.22×10^{-6}	+9.2/-4.4
8	16000	321	3.17×10^{-6}	7.81×10^{-6}	39	1.22×10^{-7}	4.88×10^{-6}	+9.2/-4.4
9	40000	129	1.27×10^{-6}	3.12×10^{-6}	20	9.76×10^{-8}	3.90×10^{-7}	+9.2/-4.4

Figure Captions

Fig. 1. Map of the area of the experimental campaign, including Northern Italy and the Alpine massif. Contour lines of equal altitude are shown for 500, 1000, 2000, and 3000 m levels. The dots represent the seven microbarograph stations in Italy set up for the experiment. A and B are the two locations whose data are analyzed in the present paper.

Fig. 2. Example of a pressure record for station A. Smaller scale and amplitude fluctuations are superimposed over larger disturbances.

Fig. 3. Nonstationarity time scale T_2 for different periods of the pressure fluctuations. T_2 was determined by repeating the nonstationarity test for increasingly long data segments. In the range of time scales between the x and + symbols, the test did not indicate nonstationarity for every run.

Fig. 4. Subdivision of the frequency axis in bands for the spectral analysis. The curves represent the transfer functions, in dB, of the filters used to passband the pressure records.

Fig. 5. Spectral density curves of the pressure records at stations A and B. The dots on the left hand side of the plot, and the central line represent the average spectrum for the entire data base. The upper and lower lines are the envelopes of the single spectra contributing to the mean.

Fig. 6. Error limits for the calculated spectral slopes due to the spectral density uncertainties. The central line in each band represents an example of a least-squares fit with $\nu = -4$; the upper and lower curves show the departures by $\pm\varepsilon_\nu$ from the mean, with ε_ν defined by Eqn. (20).

Fig. 7. Curves representing the slope ν of the spectrum for 3 different frequency bands, vs. time of day. The mean slope of spectra is indicated by (+); the dots (.) represent the value of the mean ± one standard deviation, whereas the symbol (x) indicates the extremum values. N is the average number of spectra in each hourly interval: its variability (due to missing data) during the 24 hour period is very little.

Fig. 8. Composite histograms for $\lambda_b = \Lambda_b^{1/2}$, where Λ_b is the spectral density integrated over a frequency band (see Eqn. (21)), versus time of day. Four levels, I_0, I_1, I_2, I_3, have been identified corresponding to λ_b less than 7, 15, 50, 100 μbar, respectively, with a fifth level I_4 corresponding to $\lambda_b > 100$ μbar. As an example, along the dashed curve of Fig. 8a corresponding to 1 p.m., we have: ℓ_0 = % of time for which λ_b is less than 7 μbar; $\ell_1 - \ell_0$ = % of time λ_b is such that 7 μbar $\leq \lambda_b \leq$ 15 μbar; ℓ_2 = % of time for which λ_b is less than 50 μbar; $\ell_2 - \ell_1$ = % of time for which 15 μbar $\leq \lambda_b \leq$ 50 μbar; $\ell_3 - \ell_2$ = % of time for which 50 μbar $\leq \lambda_b \leq$ 100 μbar; ℓ_3 = 100% means that these components are present all the time with rms amplitude less than 100 μbar. Parts a, b and c refer to bands 1, 2 and 3, respectively, for station A, while parts d, e and f refer to bands 1, 2 and 3, respectively, for station B.

Fig. 9. Part a: mean value of the slope for each band for station A, solid line, and station B, dashed line. The vertical lines within each band are the uncertainties of the slopes due to the errors of the spectral density estimates calculated according to Eqn. (20).

Part b: same as for part a but for two or three frequency bands grouped together.

References

Balsley, B.B., and D.A. Carter, 1982: The spectrum of atmospheric velocity fluctuation at 8 km and 86 km. Geophys. Res. Lett., 9, 465-468.

Balsley, B.B., and K.S. Gage, 1980: The MST radar technique: potential for middle atmospheric studies. PAGEOPH, 118, 452-493.

Bendat, J.S., and A.G. Piersol, 1971: Random data: analysis and measurement procedures. Wiley-Intersci., New York, 407 pp.

Brownlee, A.K., 1965: Statistical theory and methodology in science and engineering, 2nd ed. J. Wiley, New York, 590 pp.

Bull, G., R. Dubois, J. Neisser, and J.-G. Stangerberg, 1981: Investigations on gravity waves in the vicinity of mountains. Z. Meteor., 31, 267-279 (in German).

Charney, J.G., 1971: Geostrophic turbulence. J. Atmos. Sci., 28, 1087-1095.

Chen, T.-C., and W. Wiin-Nielsen, 1978: Non-linear cascades of atmospheric energy entrophy. Tellus, 30, 313-322.

Chimonas, G., and J.R. Grant, 1984: Shear excitation of gravity waves. Part II: Upscale scattering from Kelvin-Helmholtz waves. J. Atmos. Sci., 41, 2278-2288.

Dewan, E.M., 1979: Stratospheric spectra resembling turbulence. Science, 204, 832-835.

Einaudi, F., D.P. Lalas, and G.E. Perona, 1978/79: The role of gravity waves in tropospheric processes. PAGEOPH, 117, 627-663.

Fritts, D.C., 1982: Shear excitation of atmospheric gravity waves, J. Atmos. Sci., 39, 1936-1952.

Gage, K.S., 1979: Evidence for a $k^{-5/3}$ low inertial range in mesoscale two-dimensional turbulence. J. Atmos. Sci., 36, 1950-1954.

Gossard, E.E., 1960: Spectra of atmospheric scalars. J. Geophys. Res., 65, 3339-3351.

Gossard, E.E., and W.H. Munk, 1954: On gravity waves in the atmosphere. J. Met., 11, 259-264.

Hemmerle, W.J., 1982: Algorithm 591. A comprehensive, matrix-free algorithm for analysis of variance. ACM Trans. Math. Software, 8, 383-401.

Herron, T.J., I. Tolstoy, and D.W. Kraft, 1969: Atmospheric pressure background fluctuations in the mesoscale range. J. Geophys. Res., 74, 1321-1329.

Jenkins, G.M., and D.G. Watts, 1968: Spectral analysis and its applications. Holden-Day, San Francisco, 525 pp.

Kao, S.-K., 1970: Wavenumber-frequency spectra of temperature in the free atmosphere. J. Atmos. Sci., 27, 1000-1007.

Kao, S.-K., and L.L. Wendell, 1970: The kinetic energy of the large-scale atmosphere motion in wavenumber-frequency space: I. Northern Hemisphere. J. Atmos. Sci., 27, 359-375.

Kay, S.M., and S.L. Marple, Jr., 1981: Spectrum analysis - A modern perspective. Proc. IEEE, 69, 1380-1419.

Kolmogorov, A.N., 1941: The local structure of turbulence in incompressible viscous fluid for very large Reynolds numbers. Doklady ANSSR, 30, 301.

Koopmans, L.H., 1974: The spectral analysis of time series. Academic Press, New York, 355 pp.

Lilly, D.L., 1979: The dynamical structure and evolution of thunderstorms and squall lines. Ann. Rev. Earth Planet Sci., 7, 117-161.

Lilly, D.K., 1983: Stratified turbulence and the mesoscale variability of the atmosphere. J. Atmos. Sci., 40, 749-761.

Lilly, D.K., and E.L. Petersen, 1983: Aircraft measurements of atmospheric kinetic energy spectra. Tellus, 35A, 379-382.

Lorenz, E.N., 1984: Irregularity: a fundamental property of the atmosphere. Tellus, 36A, 98-110.

Lumley, J.L., and H.A. Panofsky, 1964: The Structure of Atmospheric Turbulence, J. Wiley & Son., New York, 239 pp.

Munk, N.H., F.E. Snodgrass and M.J. Tucker, 1959: Spectra of low-frequency ocean waves. Scripps Institution of Oceanography Bulletin, 7, 283-311.

Nastrom, G.D., and K.S. Gage, 1983: A first look at wavenumber spectra from GASP data. Tellus, 35A, 383-388.

Nastrom, G.D., and K.S. Gage, 1985: A climatology of atmospheric wavenumber spectra of wind and temperature observed by commercial aircraft J. Atmos. Sci., 42, 950-960.

Nuttal, A.H., 1981: Some windows with very good sidelobe behavior. IEEE Trans. Ac., Speech, Signal Proc., ASSP-29, 84-91.

Oppenheim, A.V., and R.W. Schafer, 1975: Digital signal processing, Prentice-Hall, Englewood Cliffs, N.J., 585 pp.

Orlanski, I., and C.P. Cerasoli, 1981: Energy transfer among internal gravity modes: weak and strong interactions. J. Geophys. Res., 86, 4103-4124.

Priestley, M.B., 1965: Evolutionary spectra and non-stationary processes. J. Roy. Statist. Soc., B27, 204-237.

Rhines, P.B., 1979: Geostrophic turbulence. Annual Review of Fluid Mechanics, 11, 401-441.

Ruster, R., P. Czechowsky and G. Schmidt, 1980: VHF-radar measurements of dynamical processes in the stratosphere and mesosphere. Geophys. Res. Lett., 7, 999-1002.

Stobie, J.G., F. Einaudi, and L.W. Uccellini, 1983: A case study of gravity waves-convective storm interaction: 9 May, 1979. J. Atmos. Sci., 40, 2804-2830.

Tsao, Y.H., 1984: Tests for nonstationarity. J. Acoust. Soc. Am., 75, 486-498.

Tukey, J.W., 1984: Styles of spectrum analysis. In: A Celebration in Geophysics and Oceanography - 1982: In Honor of Walter Munk, Scripps Institute of Oceanography, La Jolla, 118 pp.

VanZandt, T.E., 1982: A universal spectrum of buoyancy waves in the atmosphere. Geophys. Res. Lett., 9, 575-578.

VanZandt, T.E., T.L. Green, K.S. Gage and W.L. Clark, 1978: Vertical profiles of refractivity turbulence structure constant: Comparison of observations by the Sunset radar with a new theoretical model. Radio Science, 13, 819-829.

Vinnichenko, N.K., 1970: The kinetic energy spectrum in the free atmosphere - 1 second to 5 years. Tellus, 22, 158-166.

Wiin-Neilsen, A., 1967: On the annual variation and spectral distribution of atmospheric energy: Tellus, 19, 540-559.

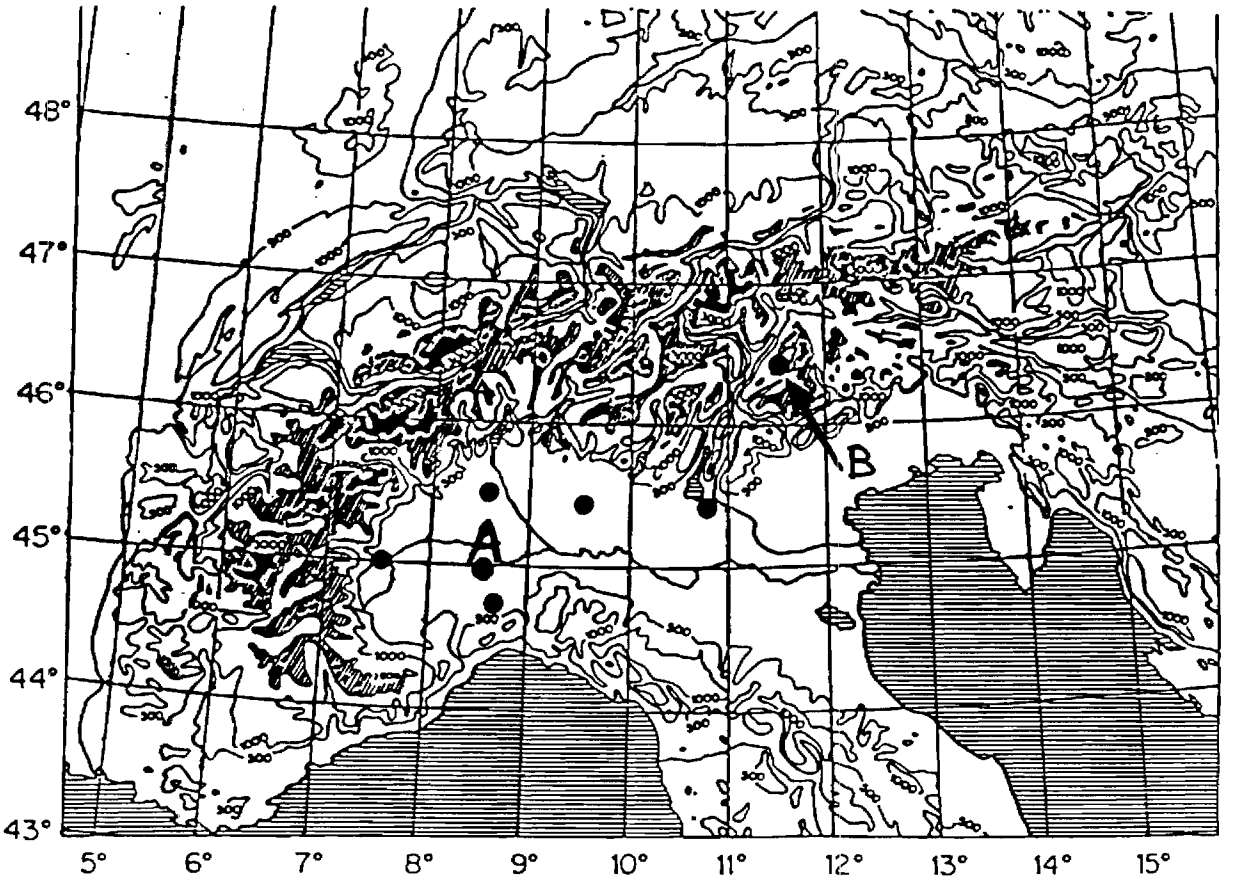

Fig 1.

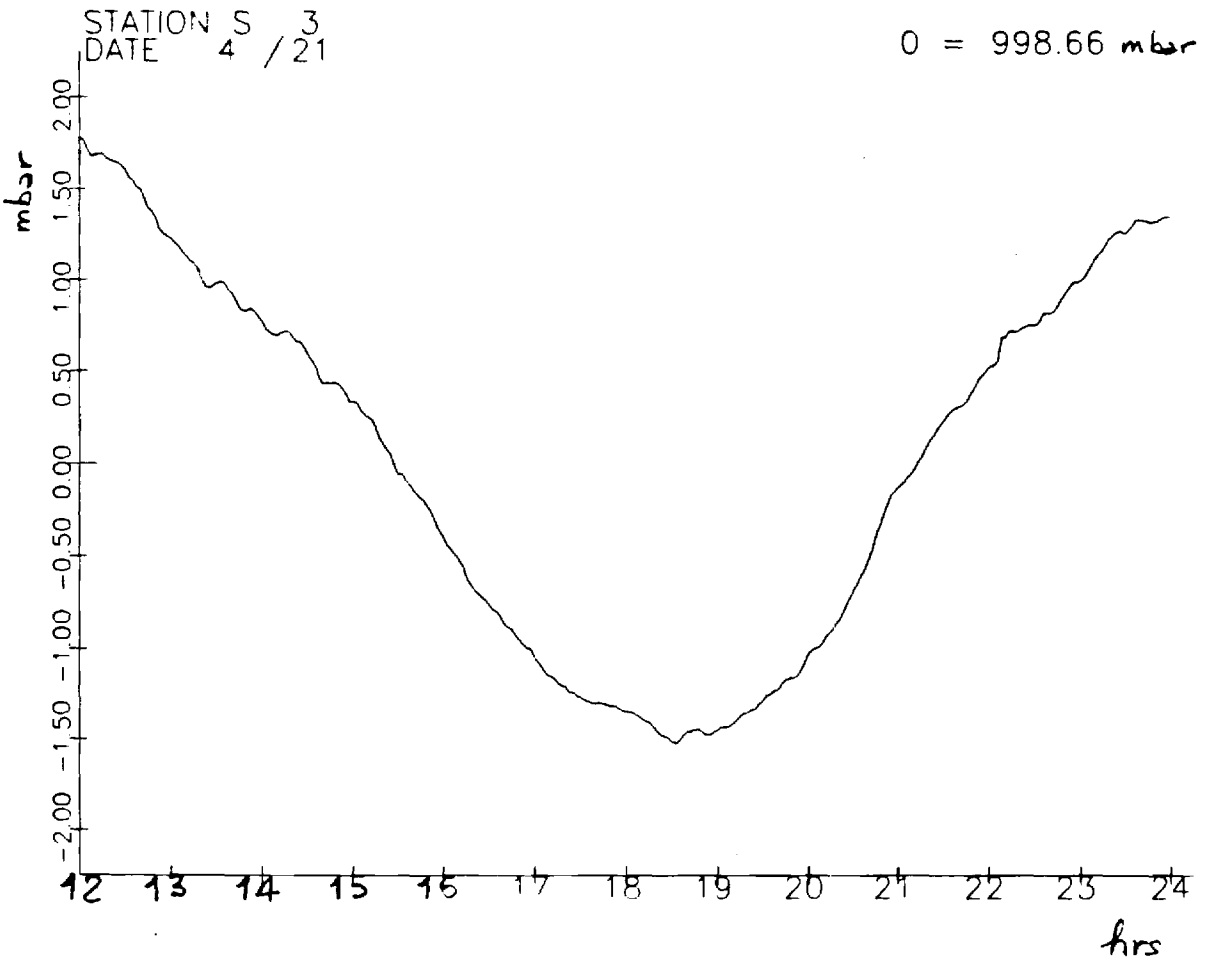
STATION S 3
DATE 4 / 21
0 = 998.66 mbar
mbar
2.00
1.50
1.00
0.50
0.00
-0.50
-1.00
-1.50
-2.00
12
13
14
15
16
17
18
19
20
21
22
23
24
hrs

Fig. 2

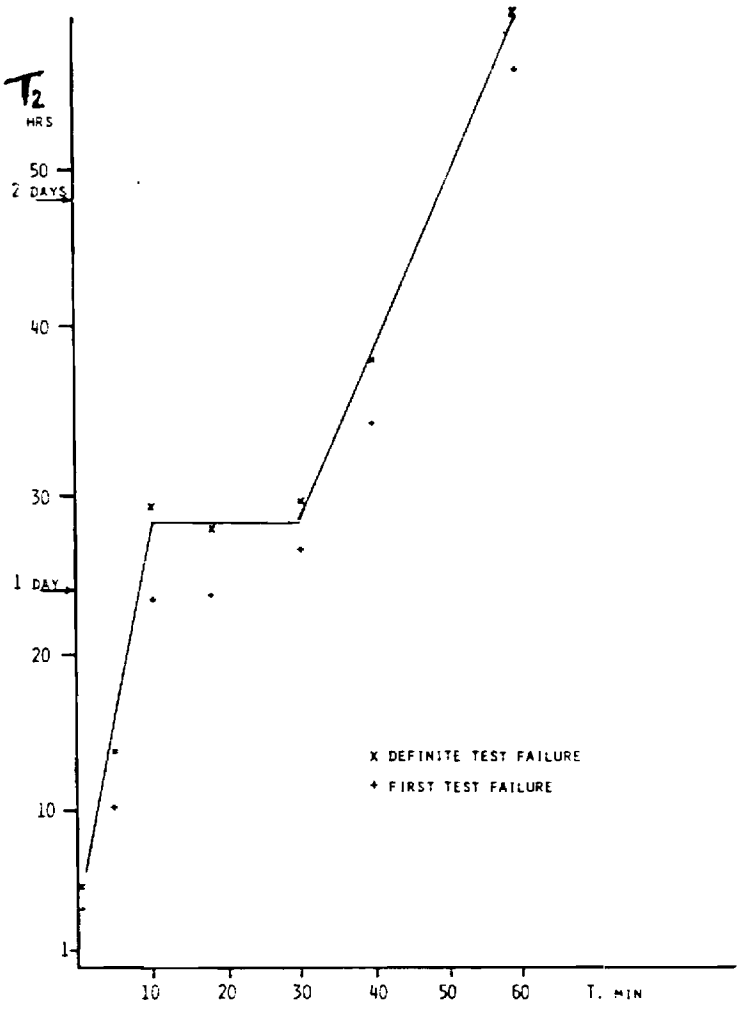
T2
HRS
50
2 DAYS
40
30
1 DAY
20
10
1
10
20
30
40
50
60
T. MIN
X DEFINITE TEST FAILURE
+ FIRST TEST FAILURE

Fig. 3

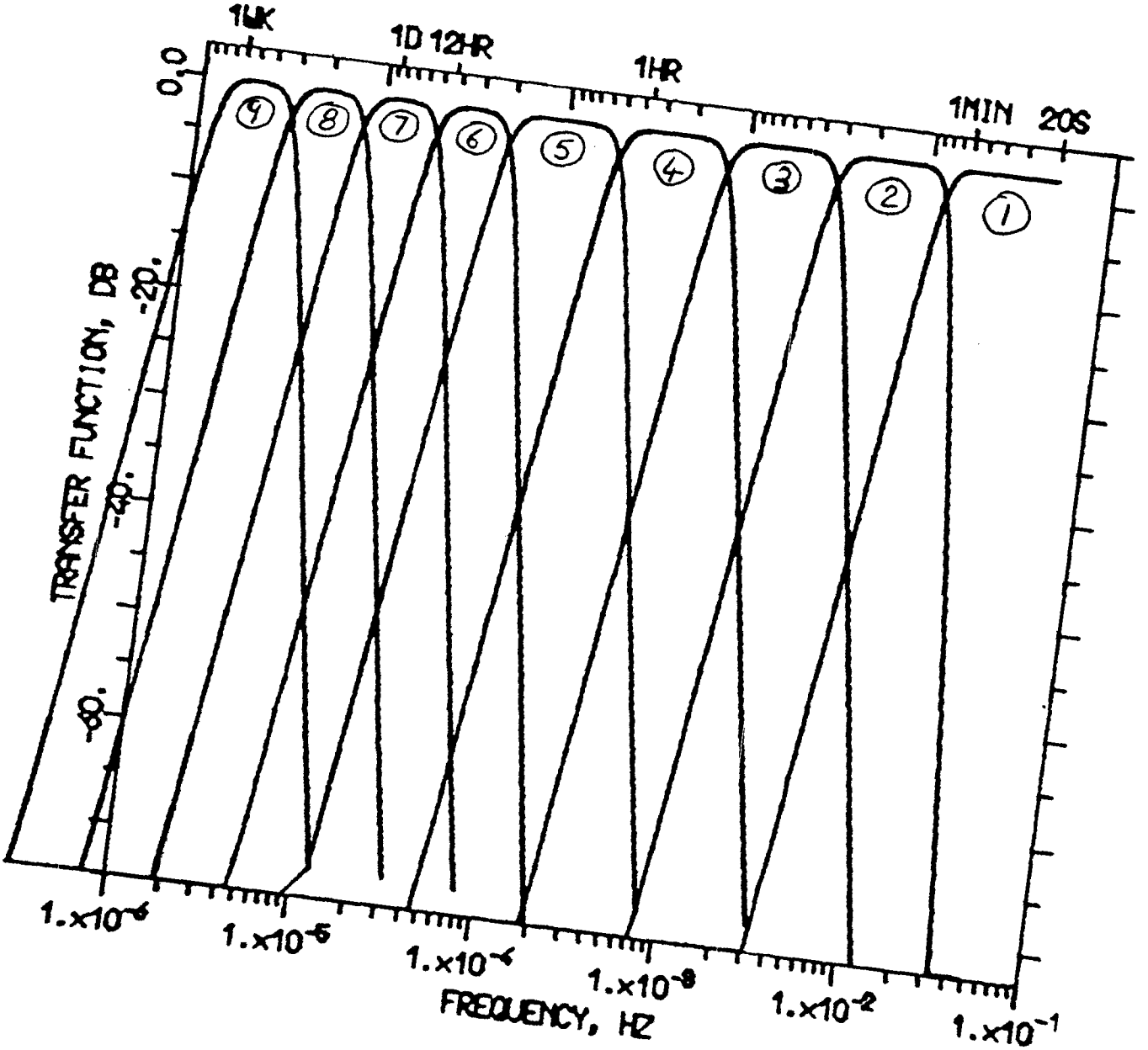
1WK
1D 12HR
1HR
1MIN 20S
0.0
-20.
-40.
-60.
TRANSFER FUNCTION, DB
1
2
3
4
5
6
7
8
9
1.x10⁻⁶
1.x10⁻⁵
1.x10⁻⁴
1.x10⁻³
1.x10⁻²
1.x10⁻¹
FREQUENCY, HZ

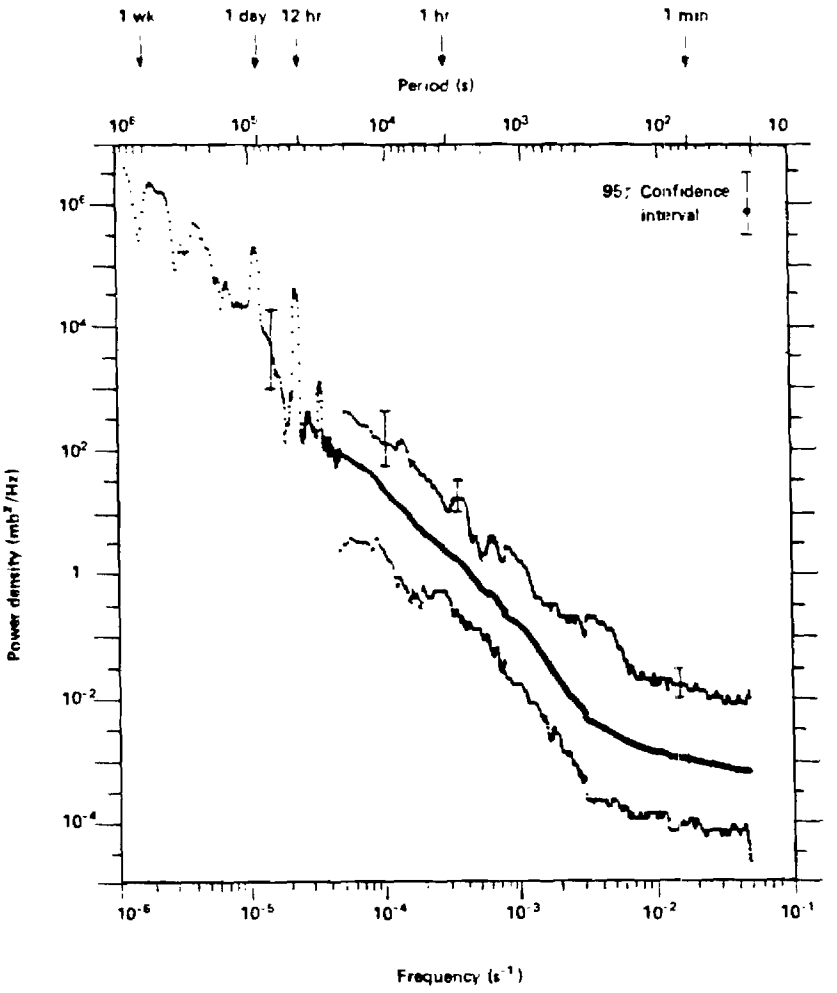
1 wk
1 day
12 hr
1 hr
1 min
Period (s)
10^6
10^5
10^4
10^3
10^2
10
95% Confidence interval
10^6
10^4
10^2
1
10^{-2}
10^{-4}
Power density (mb^2/Hz)
10^{-6}
10^{-5}
10^{-4}
10^{-3}
10^{-2}
10^{-1}
Frequency (s^{-1})

Fig. 5a

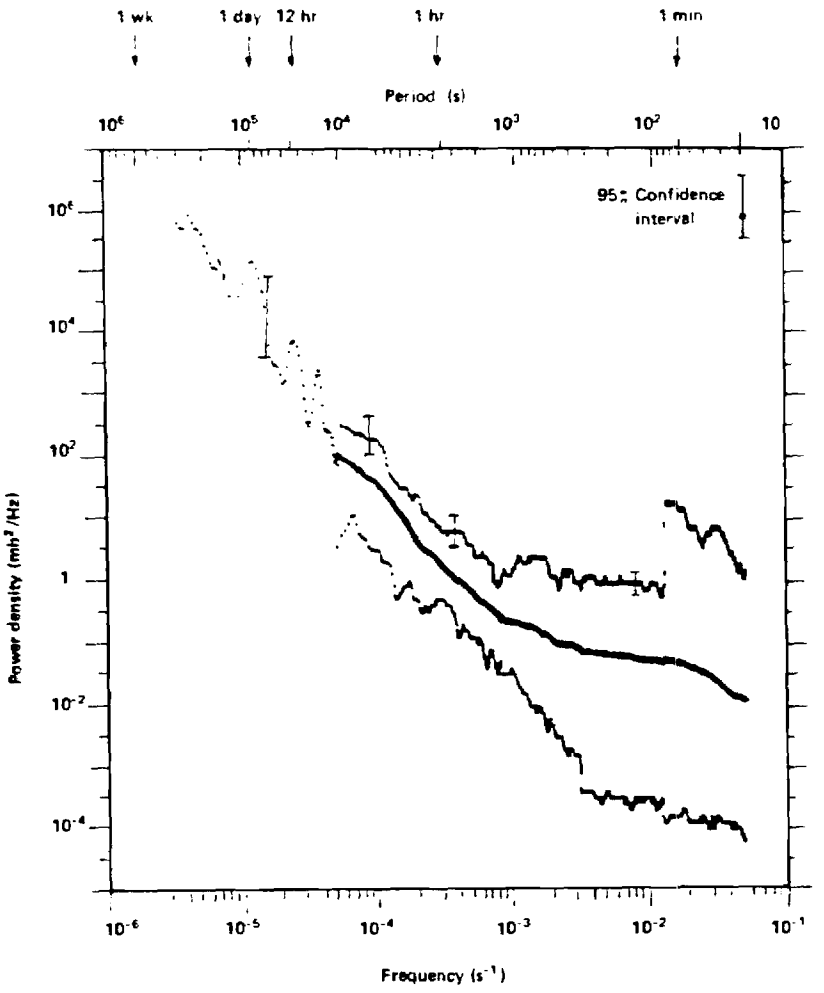
1 wk
1 day
12 hr
1 hr
1 min
Period (s)
10^6
10^5
10^4
10^3
10^2
10
95% Confidence interval
10^6
10^4
10^2
1
10^{-2}
10^{-4}
Power density (mh²/Hz)
10^{-6}
10^{-5}
10^{-4}
10^{-3}
10^{-2}
10^{-1}
Frequency (s^{-1})

Fig. 5b

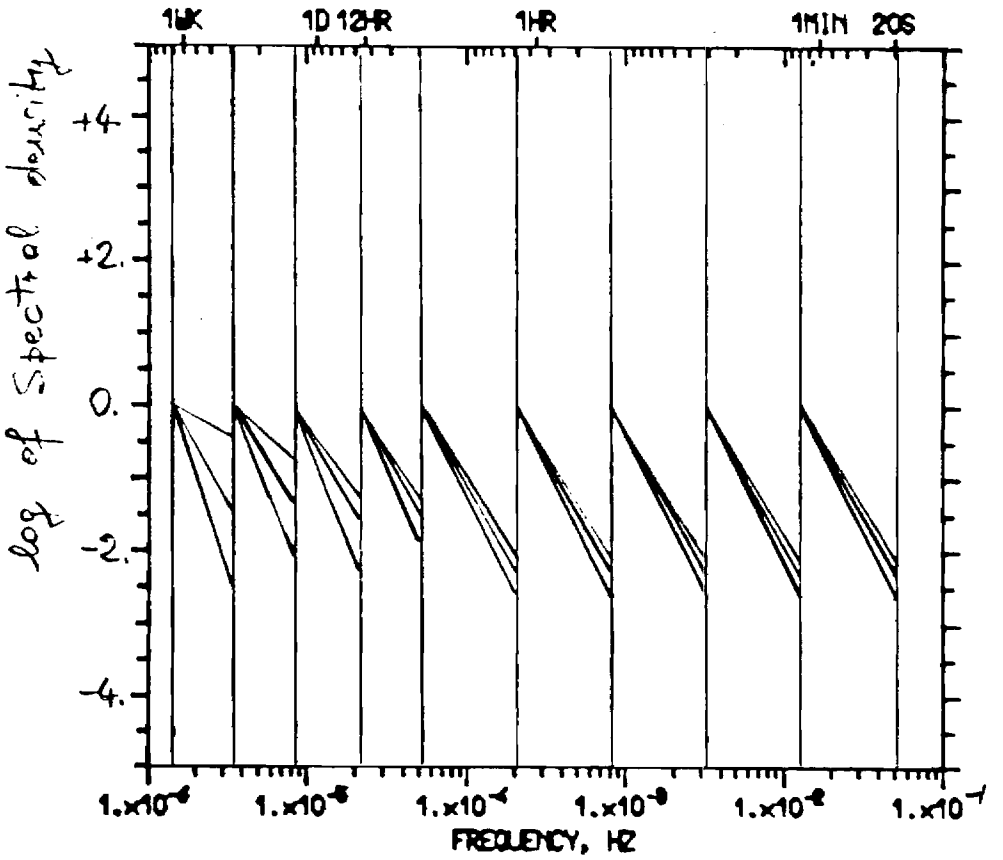
1WK
1D 12HR
1HR
1MIN 20S
log of Spectral density
+4
+2.
0.
-2.
-4.
1.x10⁻⁶
1.x10⁻⁵
1.x10⁻⁴
1.x10⁻³
1.x10⁻²
1.x10⁻¹
FREQUENCY, HZ

Fig 6

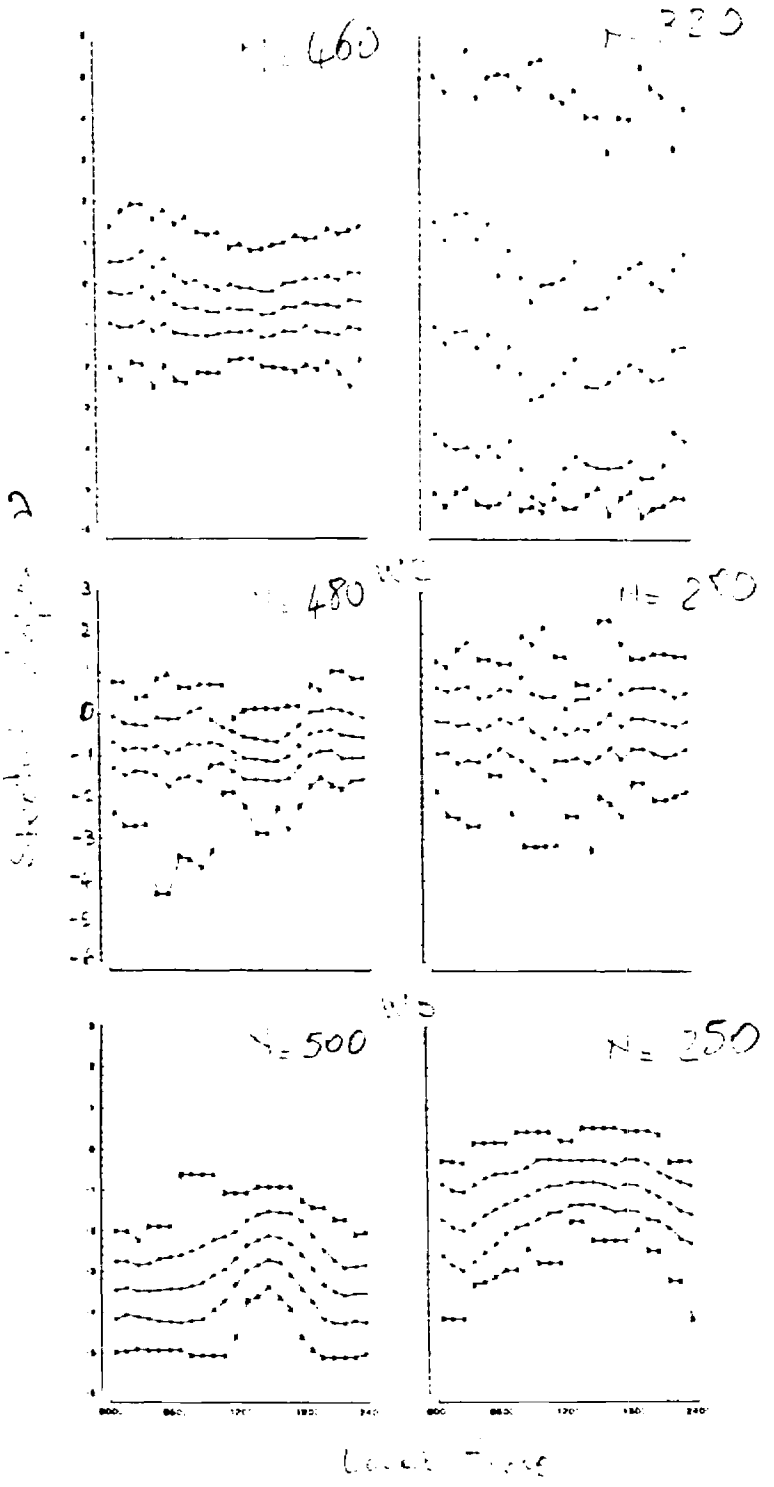

Fig. 7

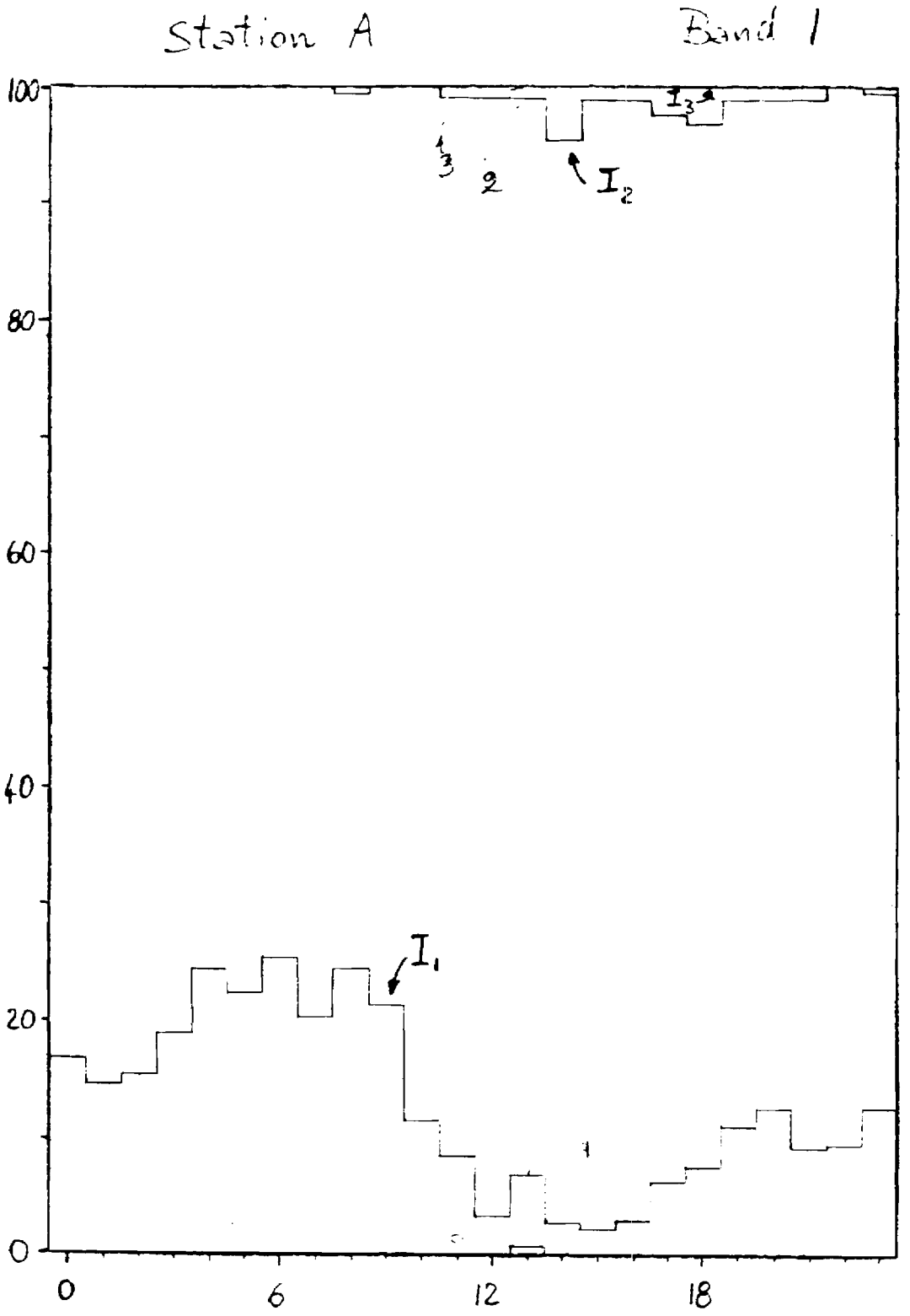

Fig. 8a

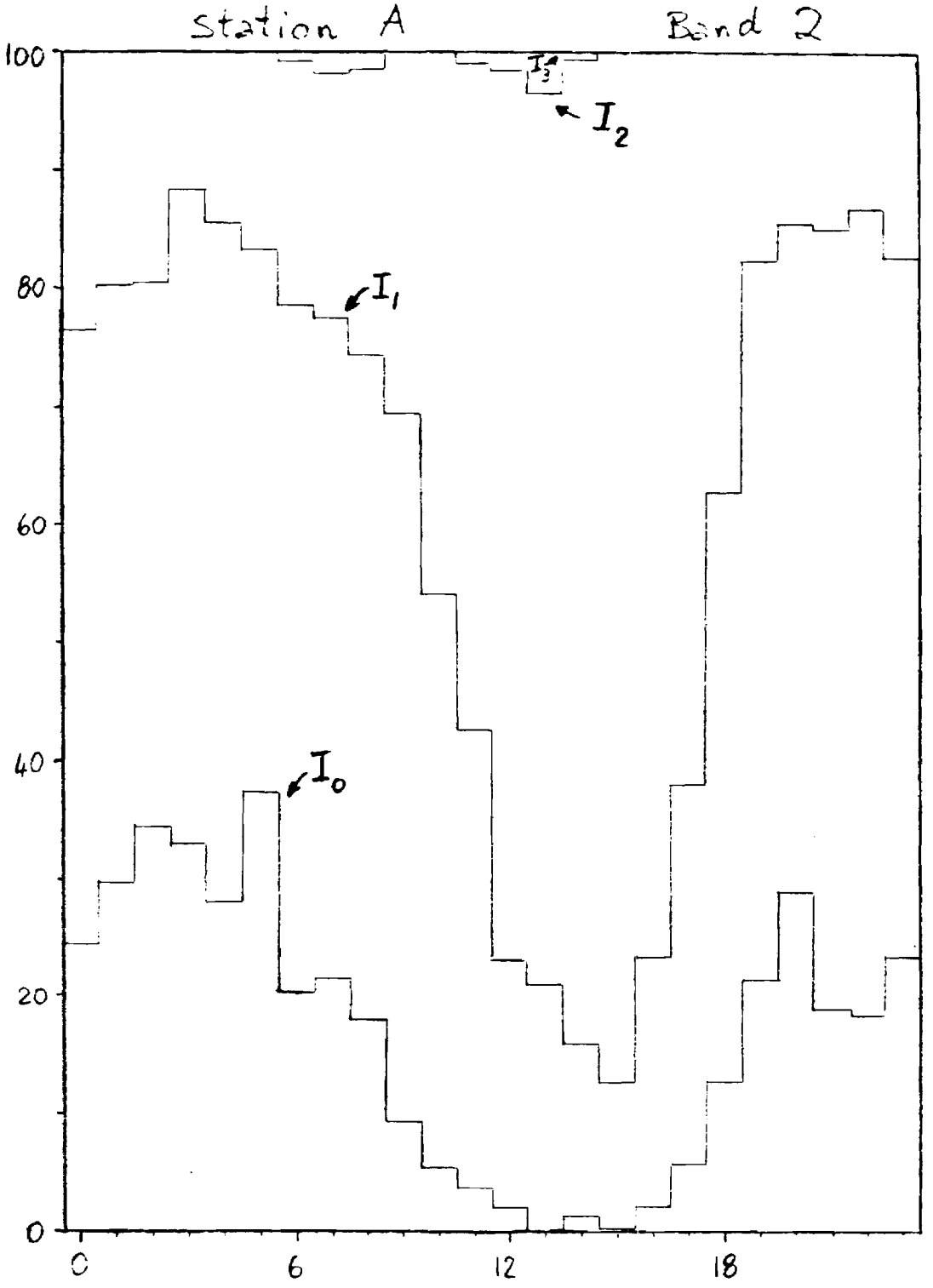

Fig. 8b

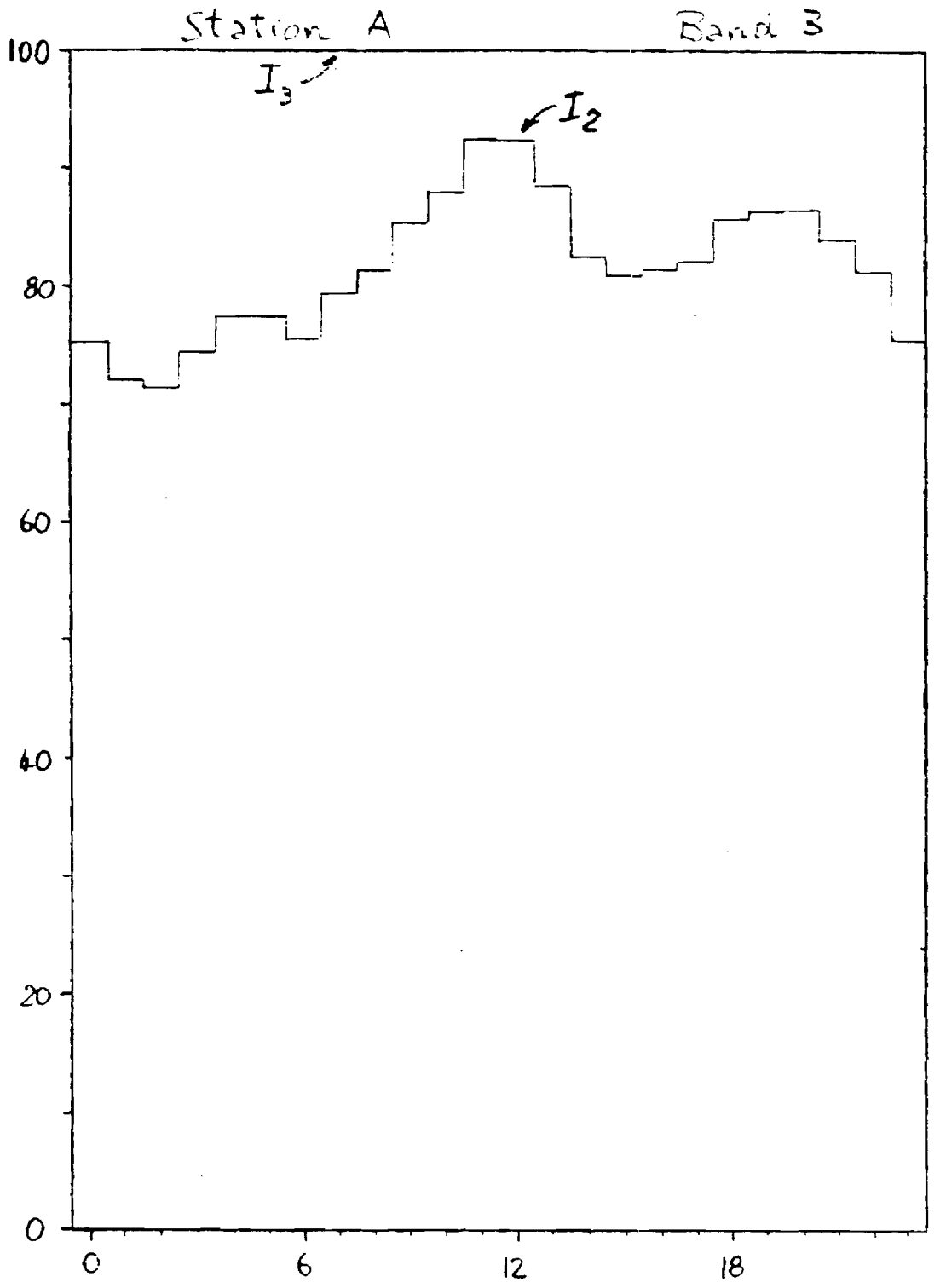

Fig. 8c

Station E Band 1

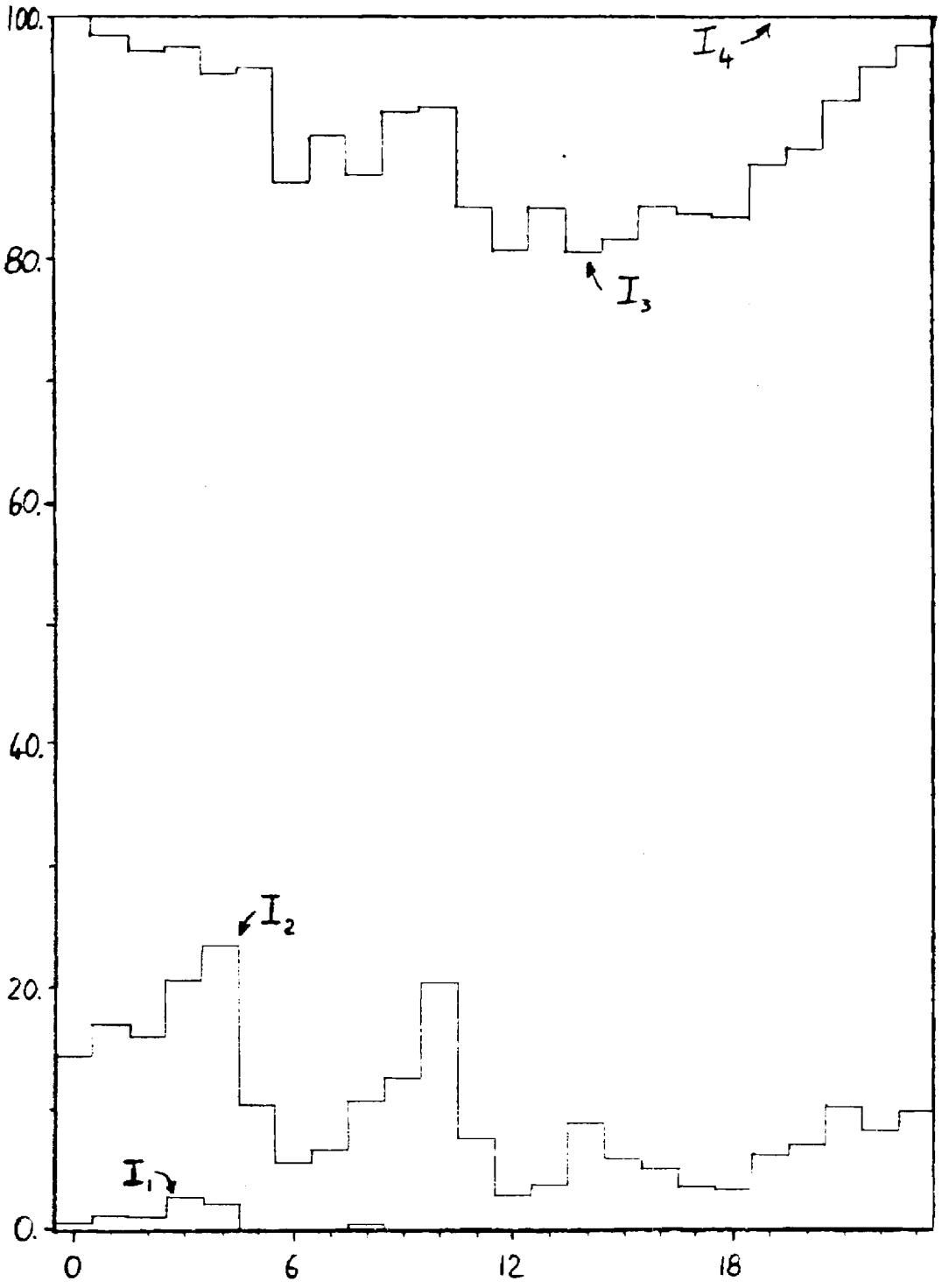

Fig. 8d

Station 1 Band 2

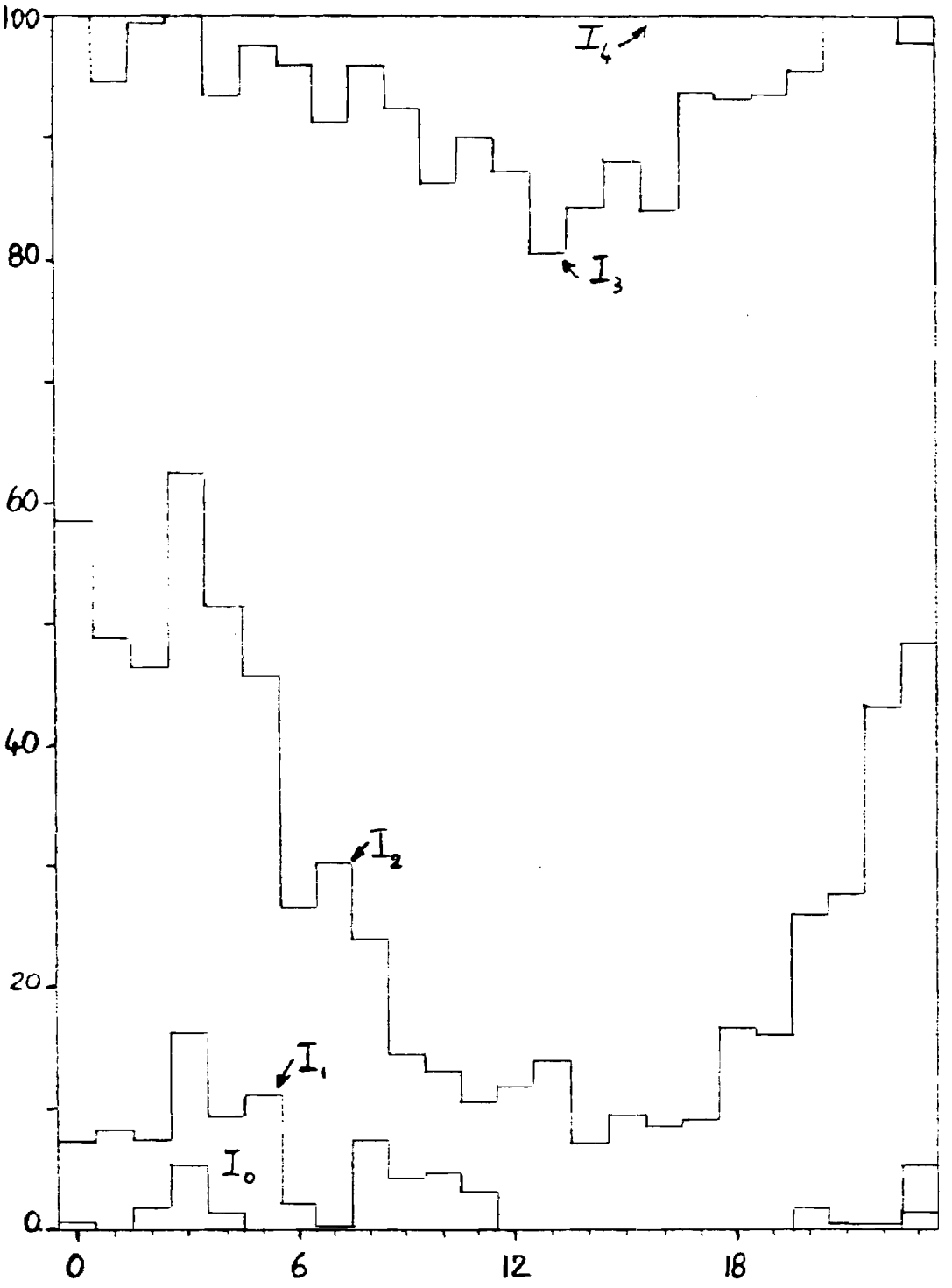

Fig. 8c

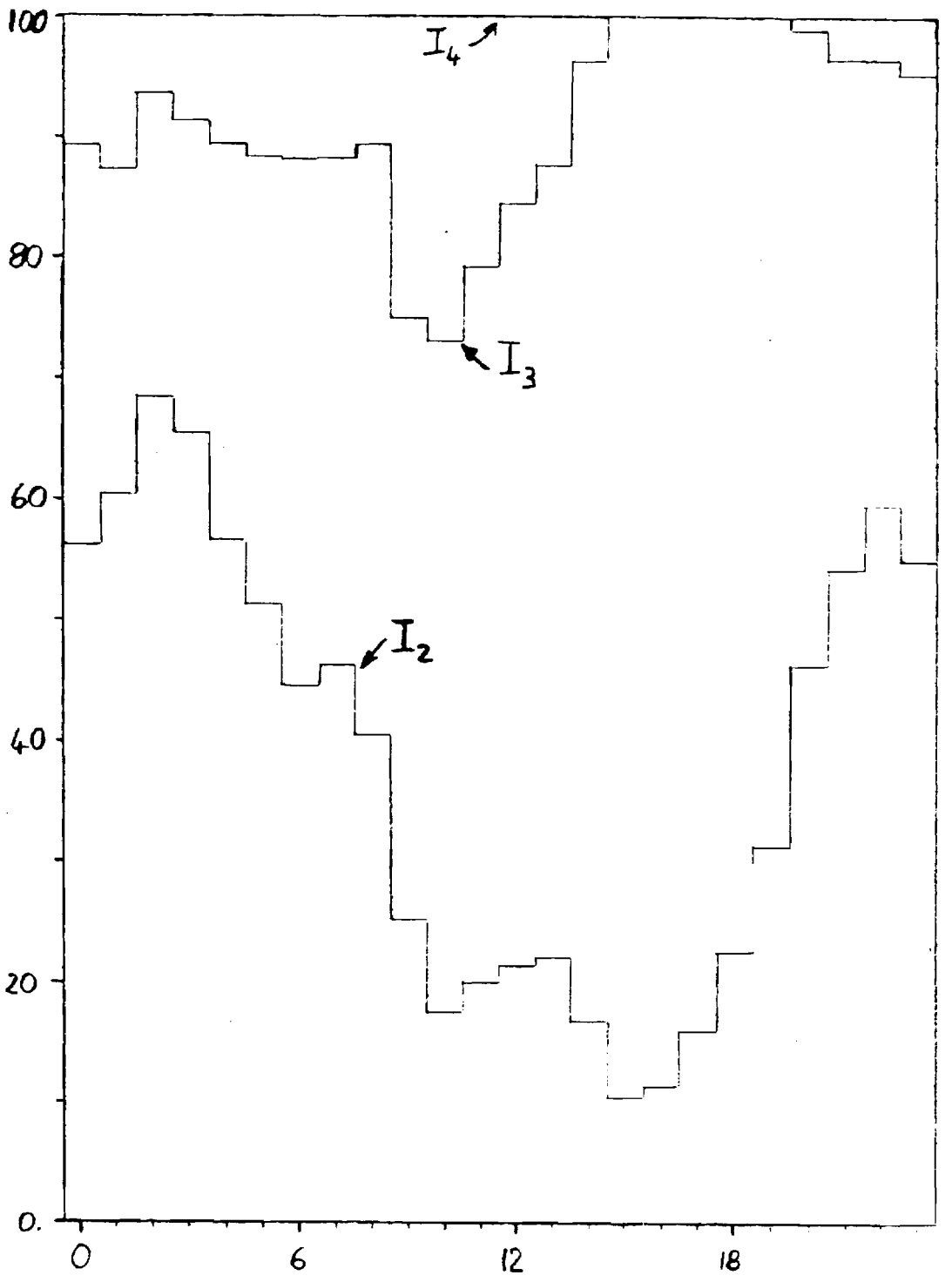

Fig. 8f

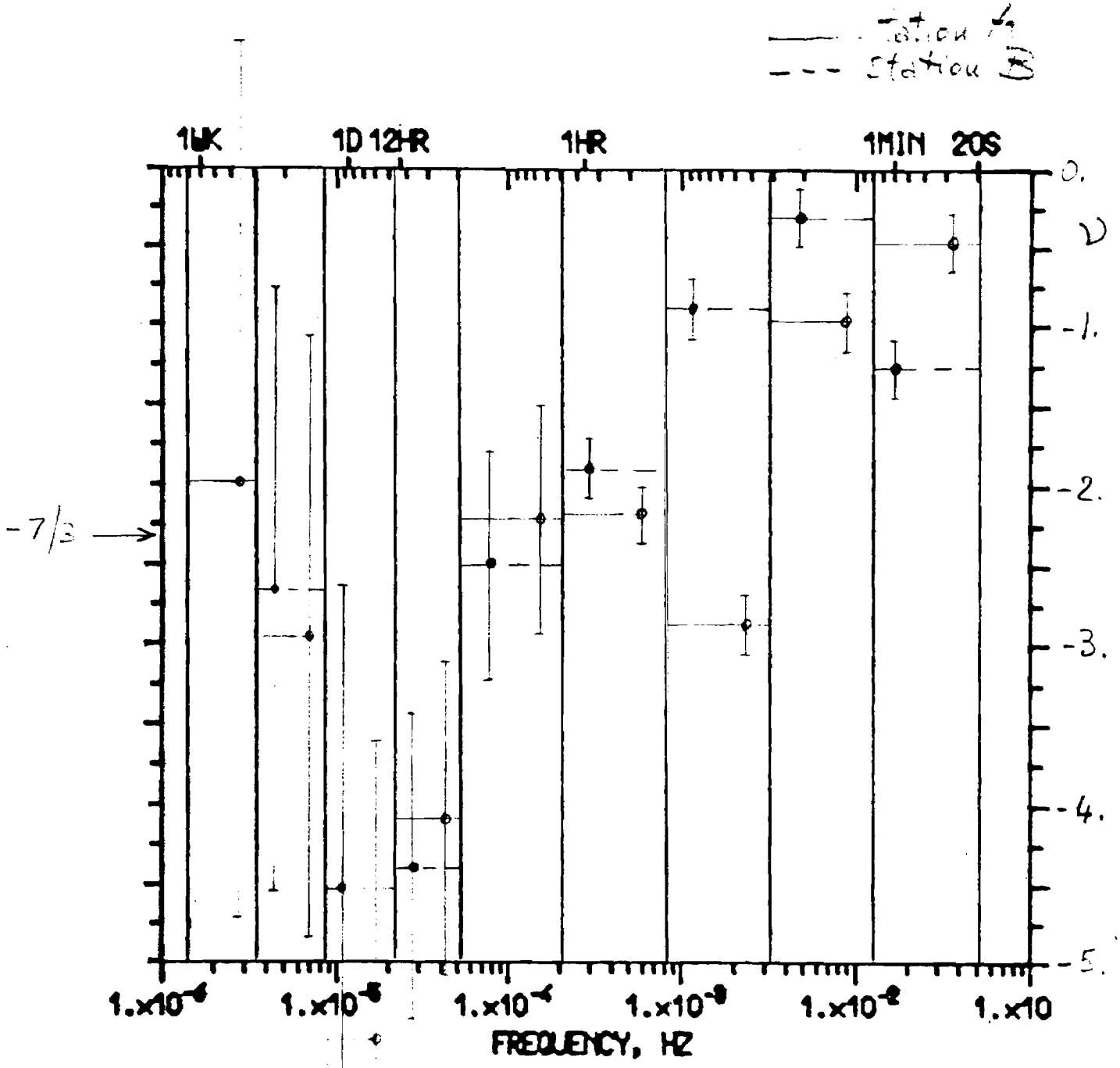
Station A
Station B
1WK
1D 12HR
1HR
1MIN 20S
0.
-1.
-2.
-3.
-4.
-5.
-7/3
1.x10⁻⁶
1.x10⁻⁵
1.x10⁻⁴
1.x10⁻³
1.x10⁻²
1.x10
FREQUENCY, HZ

Fig. 9a

Station A

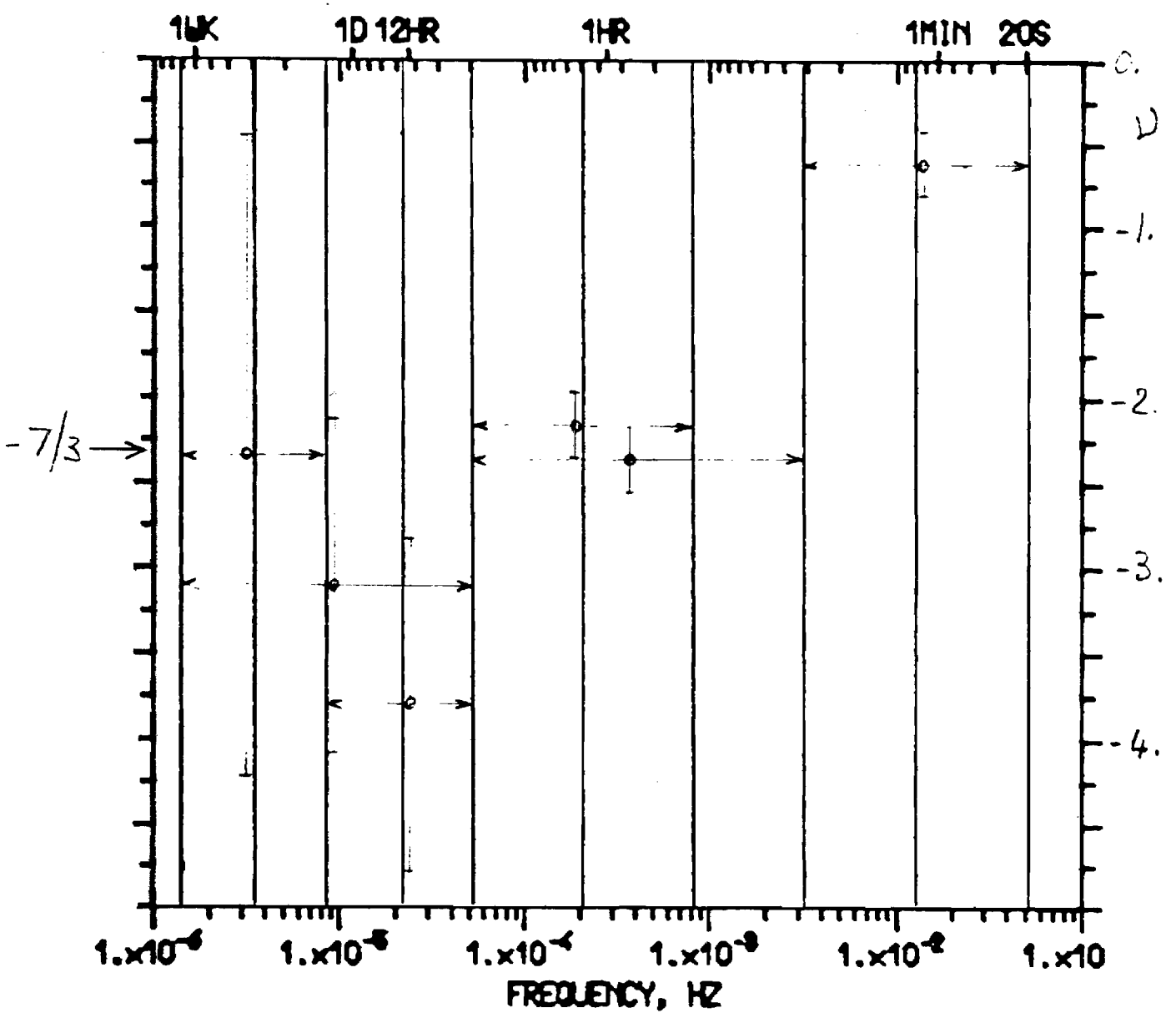

Fig. 9b

Station 5

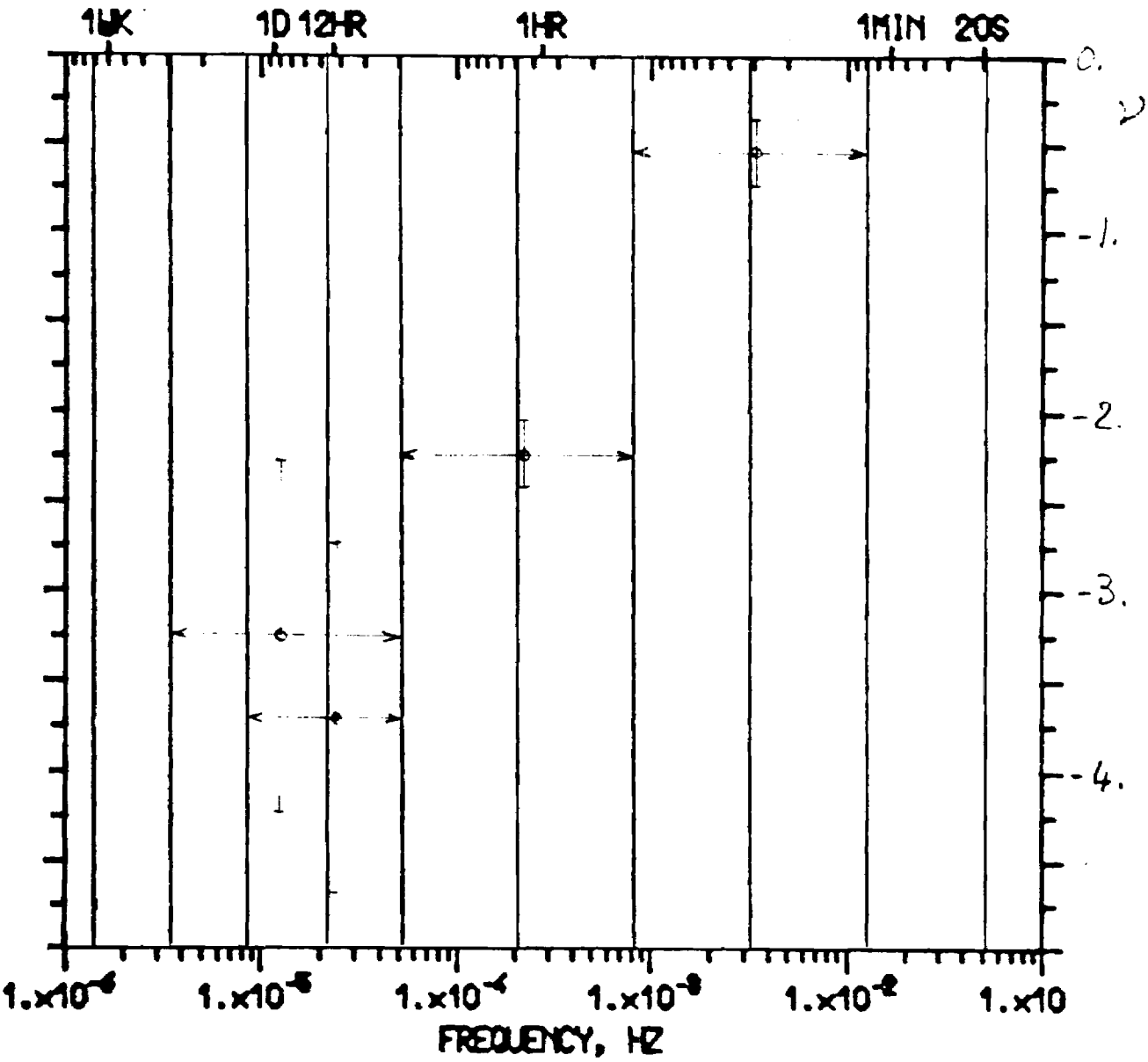

Fig. 2c